On-Track Testing as a Validation Method of Computational Fluid Dynamic Simulations of a Formula SAE Vehicle

By

Robert Weingart

Submitted to the graduate degree program in Mechanical Engineering and the Graduate Faculty of the University of Kansas in partial fulfillment of the requirements for the degree of Master of Science.

_____

Chairperson Dr. Robert M. Sorem

_____

Dr. Peter W. Tenpas

_____

Dr. Zhongquan (Charlie) Zheng

Date Defended: 19 February 2015

The Thesis Committee for Robert Weingart

certifies that this is the approved version of the following thesis:

On-Track Testing as a Validation Method of Computational Fluid Dynamic Simulations of a Formula SAE Vehicle

_____

Chairperson Dr. Robert M. Sorem

Date approved: 19 February 2015

AN ABSTRACT OF THE THESIS OF

Robert Weingart for the degree of Masters of Science in Mechanical Engineering

presented on 19 February, 2015.

Title: On-Track Testing as a Validation Method of Computational Fluid Dynamic Simulations of a Formula SAE Vehicle

This thesis is about the validation of a computational fluid dynamics simulation of a ground vehicle by means of a low-budget coast-down test. The vehicle is built to the standards of the 2014 Formula SAE rules. It is equipped with large wings in the front and rear of the car; the vertical loads on the tires are measured by specifically calibrated shock potentiometers. The coast-down test was performed on a runway of a local airport and is used to determine vehicle specific coefficients such as drag, downforce, aerodynamic balance, and rolling resistance for different aerodynamic setups. The test results are then compared to the respective simulated results. The drag deviates about 5% from the simulated to the measured results. The downforce numbers show a deviation up to 18% respectively. Moreover, a sensitivity analysis of inlet velocities, ride heights, and pitch angles was performed with the help of the computational simulation.

ACKNOWLEDGEMENTS

This master thesis has been performed in collaboration with the Formula SAE team of the University of Kansas. I would like to thank my supervisor Dr. Robert M. Sorem for his support and advice; the Jayhawk Motorsports 2014 and 2015 team and their members for helping to prepare the car as well as performing the tests, and my committee members Dr. Peter W. Tenpas and Dr. Zhongquan Zheng for their time and expertise. Last but not least, I deeply appreciate all the support from the Fulbright Commission and the Fulbright Foreign Student Program. Without their support, this thesis and my graduate program would not have been possible.

TABLE OF CONTENTS

LIST FIGURES

LIFT OF TABLES

LIST OF APPENDIX

ABBREVIATIONS

Abbreviation	Description
AoA	Angle of attack
CFD	Computational Fluid Dynamics
CoG	Center of gravity
CoP	Center of pressure
FSAE	Formula SAE
HCM	Half car model
JMS	Jayhawk Motorsports
NS	Navier-Stokes
RANS	Reynolds-Average-Navier-Stokes

1. Introduction

Motor sport is a fascinating competition where car manufacturers, professional racing companies and amateur teams race with their specialized cars in different classes and disciplines. The goal of race car engineering is to build the fastest car according to the rules. Nowadays, external aerodynamics play a key role in vehicle dynamics. The higher the (vertical) aerodynamic load on the tires, the higher the force generation due to friction is. Acceleration capabilities (longitudinally and laterally) benefit from increased tire forces which results in higher velocities in corners and on straights [1].

This thesis studies the aerodynamic package of the open-wheeled single-seater race car “JMS14c” of the Jayhawk Motorsports team (see Figure 1). The student-built car is designed according to the rules and standards of Formula SAE (FSAE) [2]. It is an international design competition held by leading engineering societies around the world.

Figure 1: Jayhawk Motorsports, JMS14c-race car

1.1. Objectives

The aim of this thesis is a comprehensive aerodynamic analysis of the existing race car JMS14c. The use of computational fluid dynamic (CFD) simulations is common practice in FSAE aerodynamic design. Limited funding, computer cluster usage, and no access to

professional aerodynamic validation methods such as wind tunnels let most of the teams rely on CFD simulations exclusively. However, CFD simulations are often simplified and it is difficult to judge the accuracy of the results and their application to the real world without validation tests. A comprehensive and adjustable CFD model has been developed within this thesis. Furthermore, the practicability and benefits of coast-down tests as a low-budget validation method are explored and compared with the computational simulations.

1.2. Delimitations

This study focuses on the general aerodynamic properties of the JMS14c and changes to the aerodynamic force production which are caused by vehicle's motion. No experimental measurements in a constant environment (wind tunnel) are carried out due to budget and time constraints. Instead, real track testing is compared and evaluated with the help of sensor data. Numerical methods are employed for the prediction of aerodynamic forces and the visualization of the air flow around the car. Simulations are performed on half car geometries only, consequently no detailed simulations of selected areas are performed. The method of Reynolds Average Navier Stokes (RANS) with the $k-\omega$ (omega) turbulence model is used to solve the differential equations of the computational grid. No transient solving methods such as large eddy simulation (LES) or detached eddy simulation (DES) are used.

1.3. Aerodynamic Design Rules of FSAE

In FSAE, the position and size of any aerodynamic device is described in the set of rules. The 2014 rules [2] define that no part can be: "a) Further forward than 762 mm (30 inches)

forward of the fronts of the front tires; b) No further rearward than 305 mm (12 inches) rearward of the rear of the rear tires; [and] c) No wider than the outside of the front or rear tires measured at the height of the hubs, whichever is wider." (see Figure 2). There is no limitation given for the maximum height of any aerodynamic device. However, the height of the rear wing is a compromise of a low center of gravity, the maximum downforce through undisturbed airflow above the car, and generated aerodynamic drag forces. All aerodynamic devices of the JMS14c have been designed according to the rules of the year 2014.

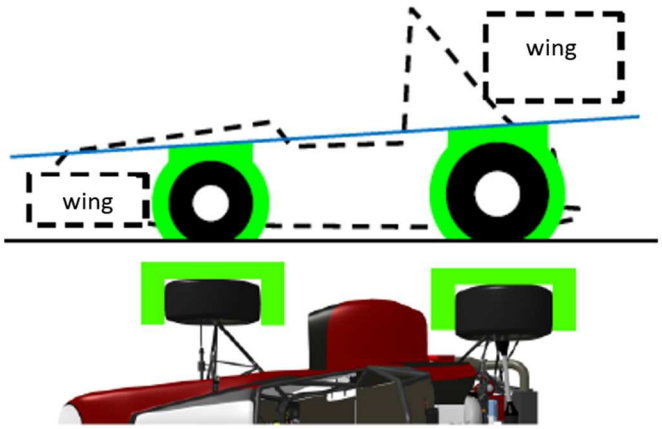

Figure 2: FSAE 2014 rules for position of aerodynamic devices [2]

During the event, aerodynamic devices can be adjusted but not replaced or completely dismounted. It is common practice to run different setups for each discipline specifically. All disciplines and setup goals are listed in Table 2 (p.31).

2. Background

In this section, fundamental vehicle dynamics and external aerodynamics are described. An understanding of these topics is necessary and the reader can refer to [3-6] and [1, 7-10] for more details of vehicle dynamics and race car aerodynamics, respectively. Furthermore, a Cartesian coordinate system is used to describe directions of motion and forces (Figure 3) throughout this thesis.

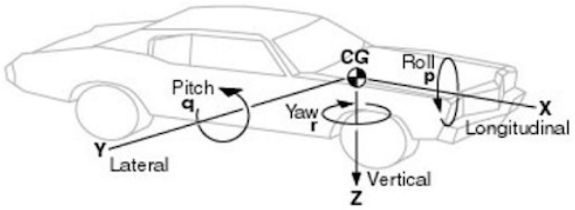

Figure 3: Vehicle axis and coordinate system according to SAE standard [11]

2.1. Vehicle Dynamics

Vehicle dynamics in general describe the motion based on distance, velocity, and acceleration of the car in all three directions (longitudinally, laterally, and vertically). The goal in race car engineering is to improve the acceleration capabilities of the car which inherently increases the velocity around the track and reduces lap times.

2.1.1. Longitudinal Motion

A vehicle is in longitudinal motion when there are no side forces and the driving direction is straight ahead. This motion is described by an equilibrium of forces that combines all driving forces and resistances of the longitudinal motion [3]. The equation is written as:

[3]

$$F_{drive} = F_{R,air} + F_{R,roll} + F_{R,grade} + F_{R,acc} \quad (1)$$

where F_{drive} is the available force supplied by the power train of the car. All other terms are listed in Table 1. To accelerate the car (increasing velocity), there has to be an excess of driving force with respect to the all driving resistances. The car is in a constant motion (zero acceleration) when the driving force is equal to all combined resistant forces. In deceleration (braking, reducing velocity), driving resistances support the process of slowing down the vehicle.

Table 1: Overview of driving resistances acting on a moving vehicle

Driving Resistance	**Symbol**	**Description and equation**
Rolling and frictional resistance [3]	$\mathrm{F_{R,roll}}$	- tire resistances caused by rolling on the ground (assumed to be a constant, $f_{R,roll,0}$) - includes frictional resistances of power train and suspension (wheel bearings, drive axle joints, chain drive, differential, clutch, engine internals, gears) that depend on the vehicle velocity, $f_{R,fric,1}$ [12] - Coefficient: $f_R = f_{R,roll} + f_{R,fric}\, v$ (2) - equation: $\mathrm{F}_{R,roll} = \mathrm{m_{stat}\, g\, f_R}\, cos(\alpha)$ (3)
Air resistance [3]	$\mathrm{F_{R,air}}$	- forces resulting from a vehicle's interaction with air - equation: $\mathrm{F_{R,air}} = \mathrm{c_D}\, \frac{\rho_{air}}{2}\, \mathrm{A_{face}}\, v^2$ (4)
Grade resistance [3]	$\mathrm{F_{R,grade}}$	- gravitational forces through inclined/ declined road (α) - equation: $\mathrm{F_{R,grade}} = \mathrm{m}_{stat}\, \mathrm{g}\, \sin(\alpha)$ (5)
Acceleration resistance [3]	$\mathrm{F_{R,acc}}$	- resistance resulting from all rotating parts of a vehicle - additional energy is needed to accelerate rotating parts against their rotational inertias - can be expressed as a characteristic factor λ or as an additional mass reduced to the tire - equation: $\mathrm{F_{R,acc}} = \mathrm{m}_{stat}\, \lambda\, \mathrm{a}$ (6)

By substituting all described resistances into equation (1), the equation can be written as:

$$F_{drive} = c_D \frac{\rho_{air}}{2} A_{face}\, v^2\, h_{COG} + m\ \mathrm{g}\ \mathrm{f_R} \cos\alpha + \mathrm{m}\ \mathrm{g}\ \sin\alpha + \mathrm{m}\ \lambda\ \mathrm{a} \tag{7}$$

c_D – drag coefficient
ρ_{air} – density of air
A_{face} – frontal face of vehicle
m_{stat} – static mass of vehicle
v – velocity
a – inclination angle
g – gravity

The only term related to aerodynamic forces in this equation is drag. Reducing drag helps the positive acceleration of the car, an increase of drag supports the braking phase.

2.1.2. Tires

Tires are the only connection between vehicle and ground. Thus, they have to transfer every force through frictional effects between the ground surface and the rubber of the tire [13]. The ratio of the generated force (F) with respect to the vertical force is referred to as coefficient of friction (μ). It indicates how much grip a tire can produce with respect to the vertical load. The ratios for both directions are written as:

[3] longitudinal: $\mu_x = \frac{F_x}{F_z}$, lateral: $\mu_y = \frac{F_y}{F_z}$ (8)

Modern FSAE racing tires are tested on specific tire testing machines such as the one of Calspan©. The “Tire Test Consortium” (TTC) is a network of many universities which funds tire tests to obtain test results of various setup iterations (inflation pressure, camber, slip angle, slip ratio, vertical loads) [14].

A tire generates a force (according to Newton’s third law) when there are differences in the motion of the tire with respect to the ground [13]. The contact patch gets deformed because of frictional forces in longitudinal, lateral or combined direction [9]. Longitudinally, the tire has to rotate faster than at rolling speed (no driving force influence) [13]. Laterally, the tire needs to turn by a larger angle than the desired driving direction [13]. A faster

rotation as rolling speed or turning by a larger angle is referred to as slip. Generally speaking, transferring forces through the tire is only possible when there is slip [15]. The slip in longitudinal direction (slip ratio, SR) is calculated in percentage and in lateral direction (slip angle, SA) it is given as an angle α.

[13]
$$SR = \frac{\omega r - v}{v} \tag{9}$$

[13]
$$\alpha = -atan\left(\frac{v_y}{|v_x|}\right) \tag{10}$$

v_x – longitudinal velocity component
v_y – lateral velocity component
ω – rotational speed of tire

The tire forces in longitudinal and lateral direction are combined in a simplified model, the traction ellipse (see Figure 4, p.21) [1, 9, 13]. This model describes transmittable forces of a tire based on its friction coefficients. It is distinguished between static (stiction) and dynamic (sliding) friction. The outer dimensions of the ellipse are based on the vertical load applied to the tire. The higher the vertical load on the tire, the larger the expansion of the ellipse in both directions is. The size of the ellipse describes the maximum amount of the transferable tire force. The traction ellipse can also be described with longitudinal (a_{long} or a_x) and lateral (a_{lat} or a_y) acceleration capabilities which is referred to as GG-plot. The car's total acceleration is then calculated by:

$$a = \sqrt{\left(a_{long}\right)^2 + (a_{lat})^2} \tag{11}$$

The traction circle dimensions do not remain static at all four tires [16]. When the car moves around the track, changes in velocity, longitudinal and lateral acceleration affect the vertical load on all four corners of the car (weight transfer and aerodynamic load).

An increase of the tire force output (when operated at its maximum) is achieved by higher vertical loads or a greater friction coefficient of tire rubber and/ or road surface [1]. Higher vertical loads are a result of either a higher mass or an aerodynamic load. But, mass ultimately hurts the cornering performance through a higher yaw and translational inertia that has to be overcome in order to rotate or accelerate the vehicle respectively. Consequently, aerodynamic loads can be used to increase the vertical load on the tires without adding substantially more mass to the car [1]. Higher vertical loads do not linearly increase the produced lateral or longitudinal force and can also cause overheating and severe tire wear. Every tire operates at its best in a specific temperature window. Consequentially, when the tire gets too hot the maximum generated force drops.

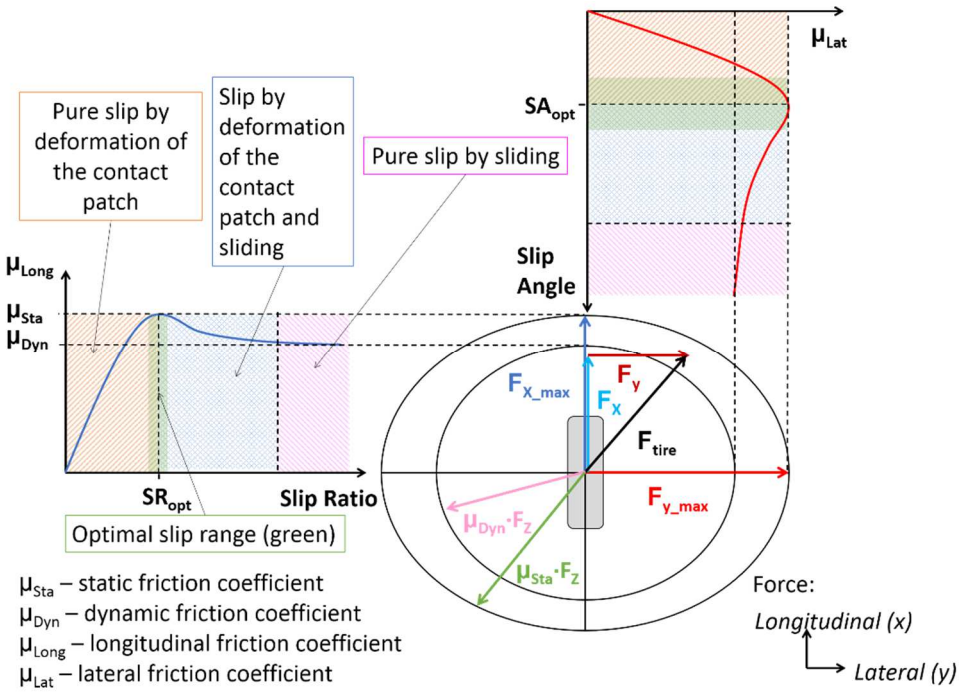

Figure 4: Traction circle based on slip [3, 6, 17, 18]

2.1.3. Handling

The term handling is referred to as how well the vehicle is balanced during the cornering phases. Although this thesis only covers straight line performance, it is important to understand the effects of the position and migration of the aerodynamic center of pressure. The handling is often simplified to three different behaviors [19]: understeering, oversteering and neutral (see Figure 5).

- A car **understeers** when the radius of the travelled curved path is larger than the desired radius of the corner (steering input). The front end of the car tends to push towards the outside of the corner instead of turning in appropriately.
- **Oversteering** is the opposite behavior of understeering. The radius of the travelled curved path is smaller than the radius of the corner. The rear end of the car tends to push towards the outside of the corner and the car turns in more than it is desired.
- The car has a **neutral balance** when the radius of the travelled curved path is equal to the corner radius.

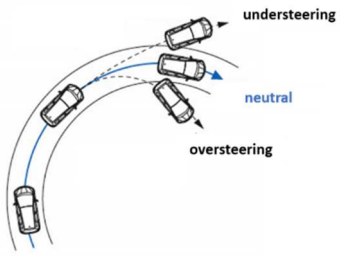

Figure 5: Oversteering, understeering and neutral car balance [20]

Oversteering or understeering is caused by an imbalance of the grip levels between the front and rear pair of wheels. When the front tires have more grip available than the rear (for instance, due to better suspension design, more downforce from the front wing, or other factors) the car tends to oversteer. If the rear tires have better grip than the front,

the car understeers. Drivers have personal preferences about the balance of a car. However, most of the drivers prefer a slight understeering behavior in high speed corners [21]. Understeering in general is considered to be the more stable driving condition. Especially in high speed sections where small steering inputs can have significant influences it is desired to have a stable behavior. For this reason, the aerodynamic center (center of pressure, CoP) is usually placed behind the CoG of the car [1]. This leads to an imbalance in the aerodynamic load towards the rear axle (especially in high-speed) and therefore, more available grip. Based on the definition above, the imbalance of grip towards the rear axle causes an understeering behavior.

2.2. External Aerodynamics

This section covers the basic principles of airflow around a body or vehicle.

2.2.1. Bernoulli's Principle

Whenever a flow moves around a body or follows a geometry, there is a change of fluid property in pressure and velocity. The relationship of pressure and velocity is described by the Bernoulli principle. According to Bernoulli, the pressure of a flow field is referred to as total pressure that consists of a static (p/ρ), dynamic ($v^2/2$), and hydrostatic (gz) part [10]. In ground vehicle aerodynamics, the hydrostatic part will remain constant and can be ignored in the equation. Thus, the equation is written as:

[13]
$$\frac{v^2}{2} + \frac{p}{\rho} + gz = constant \tag{12}$$

$$dynamic\ pres + static\ pres + hydrostatic\ pres = total\ pressure$$

The Bernoulli principle is only applicable for incompressible flow and when viscous forces are neglected. It cannot be used for calculations because the air flow around race cars is very complex including flow separation, wake areas, and viscous effects. However, it is commonly used to describe effects such as pressure and velocity changes in a flow field. For instance, when a flow velocity is increased or decreased (dynamic part) within the same volume, the static pressure changes inversely too.

2.2.2. Ground Vehicle Aerodynamics

The incoming (ideal) air flow far upstream of the vehicle is undisturbed (irrotational) and inviscid (no viscous effects). The most forward point where the flow touches the body or vehicle is called stagnation point (see Figure 6). The velocity of the air flow in this point is zero and the exerted pressure to the vehicle is maximum. The stream is then divided into parts that flow over, under or around the body (and through the body if internal flow is considered or there is an opening in the front section). The flow continues further downstream and gets reunited after a wake area behind the body.

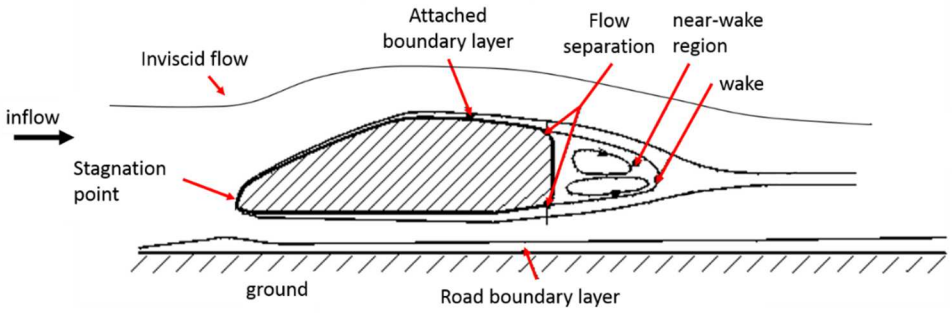

Figure 6: Flow around body [22]

Close to the body, a boundary layer is formed due to frictional effects of the flow with the body surface (wall shear stress). Along the flow direction, shear stress causes an energy exchange between the wall shear layers and the freestream flow. Thus, the boundary

layer grows [9]. At steep geometry changes (curvature, edges, obstacles), the flow can detach (separate) from the surface. Separation negatively affects the air flow downstream and increases the drag significantly [1]. When there is no flow separation due to boundary layer effects, then the flow detaches from the body at the most rearward point in its flow direction (trailing edge). Downstream of the separation point or the trailing edge, a turbulent wake region is formed. The rotational character of the wake flow prevents an increase in pressure behind the rear face of the body [9].

Drag describes the resistance of the body moving through air. It inhibits the forward acceleration but supports the deceleration. There are three different types of drag [9]: pressure, viscous, and induced drag. Pressure drag results from forces along the direction of motion of the body. The pressure behind the body is lower than in the front which creates a pressure gradient. The resulting force acts in the opposite direction of the motion. Viscous drag results from the skin friction of the moving air over a surface due to the wall shear stresses. The induced drag is created through vortices [9].

Studies on external aerodynamics (simulation and experiment) predict forces and moments acting on the body or vehicle. Forces and moments are created due to the pressure distribution and the shear stress distribution over the body surface [1]. Both parts are integrated over the entire length of the body and result in the aerodynamic force F_{air} as well as the moment M_{air}. The aerodynamic force is divided into a horizontal (drag, acts parallel to the freestream flow) and a vertical part (lift/ downforce, acts perpendicular to the freestream). For comparisons, non-dimensional coefficients of lift, drag and pressure are calculated for any type of flow around a body.

[13]
$$c_L = \frac{F_L}{\frac{1}{2}\,\rho\,A\,{V_\infty}^2} \tag{13}$$

[13]
$$c_D = \frac{F_D}{\frac{1}{2}\,\rho\,A\,{V_\infty}^2} \tag{14}$$

[13]
$$C_p = \frac{p - p_\infty}{\frac{1}{2}\,\rho\,V_\infty^2} = 1 - \frac{V^2}{V_\infty^2} \tag{15}$$

c_L – lift coefficient
F_L – lifting force
c_D – drag coefficient
F_D – drag resistance force
A – frontal face area
V – velocity
C_p– pressure coefficient
p_∞ – free stream pressure
p – pressure
V_∞ – free stream velocity

2.2.3. Lift-Generating Devices

2.2.3.1. Wings

A wing is a three-dimensional airfoil with the main purpose of generating a force perpendicular to the stream wise direction of the flow. Race cars use inverted wings to produce negative lift (downforce). A wing section is called airfoil. Important terms of an airfoil are given in Figure 7.

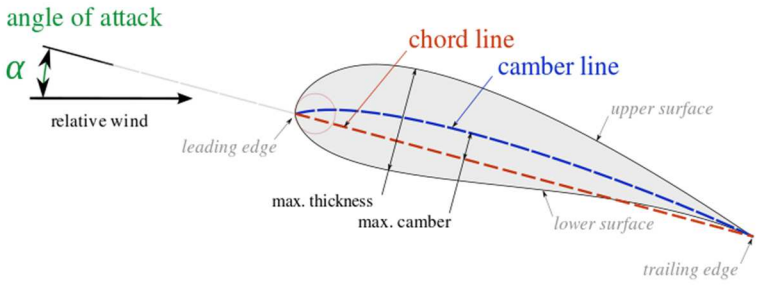

Figure 7: Airfoil term definition [23]

Considering an inverted race car wing, the air flow closest to the airfoil accelerates the most (in direction and speed) because of the steepest change in geometry. According to

Bernoulli, this increase in velocity causes a low pressure [9]. On the upper side of the airfoil, an increase in pressure occurs due to the deflection from the wall in stream wise direction which causes a reduced flow velocity. A force perpendicular to the stream is created because of the pressure gradient between upper and lower surface [9]. Both flows converge at the trailing edge and a mixing turbulent wake region is formed. The higher the angle of attack (AoA) and the camber of the airfoil, the higher the caused turbulent wake is.

Terms of the wing design are: span (width of the wing), chord (length of the wing), and aspect ratio (coefficient of span to width) [1]. The aspect ratio (AR) of race car wings is very small compared to conventional aircraft wings [15]. A negative effect of small aspect ratios is the high influence of tip vortices. At the tip of the wing, the flow exchanges pressure from the high pressure side to the low pressure side. This reduces the magnitude of the pressures and therefore the overall gradient (see Figure 8). To minimize this effect, it is common practice to fit endplates to the wingtips which help to keep the flow separated between the upper and lower side of the wing [15]. Endplates reduce the formation of vortices and therefore the induced drag [9]. Furthermore, they are used to help controlling the flow in cornering and keeping the flow channeled over and under the wing.

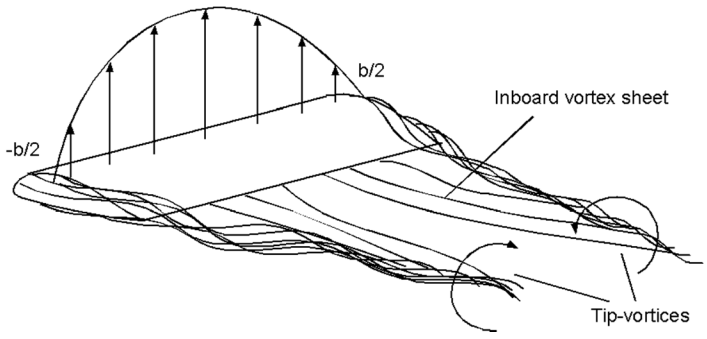

Figure 8: Wing tip vortices, pressure distribution displyed on top of the wing surface [24]

To improve the aerodynamic performance of the vehicle, engineers seek for methods to increase downforce within the limited space for wings (restricted by the rules). In FSAE and many other racing series, multi-element wings are utilized to maximize the downforce level. These wings feature a big main plane and smaller flaps that can have very steep angle of attacks in order to generate higher pressure gradients between upper and lower side. Flow separation (as it would appear at a single large element) can be delayed by air passing through the small gaps between the airfoils (re-energizing/ restarting the boundary layer) [9].

2.2.3.2. Ground Effect

When the ground is used as part of the aerodynamic system then it is referred to as ground effect [1]. It is achieved by placing aerodynamic devices close to the ground so that there is just a small gap between the part and the ground. According to the Bernoulli principle and the law of mass conservation, the velocity increases and the static pressure decreases when the same amount of air is moving through a smaller gap than before [1]. This creates a suction effect and the generated downforce is higher than in freestream condition (as long as the flow does not separate). An example flow with streamlines is shown in Figure 9. The closer the streamlines are to each other, the higher the flow velocity is and the lower the pressure is.

Figure 9: Airfoil in ground effect [25]

In terms of the design of external devices, the pressure gradient of the front wing particularly can be maximized by making use of the ground effect. The lower the front

wing is placed with respect to the ground, the higher the downforce generated. However, the downside of the ground effect is the sensitivity to ground clearance changes through bumps, pitching and rolling. These motions might result in touching the ground and damaging the wing, or in a loss of downforce because of separation at the wing.

2.2.4. Effects of External Aerodynamics on Race Car Performance

2.2.4.1. Aerodynamic Forces

Drag and downforce play a key role in the design of race cars. Devices that make use of air forces help to increase the performance of the car and greatly influence the balance. The size of aerodynamic devices depends on the available space that is usually restricted by the rules and the speed characteristics of the race track.

First, drag impedes the forward motion. The force vector of drag points in the opposite of the driving direction and increases the demand of driving force in forward acceleration [9]. The vehicle accelerates slower and its top speed is reduced. However, drag supports the deceleration under braking. Second, downforce improves cornering and braking capabilities by increasing the vertical load on the tire without adding an equivalent amount of physical mass to the vehicle [1]. Ultimately, the car benefits from a higher grip level without an increased yaw inertia. Equations (13) and (14) show that the aerodynamic forces change with the square of the velocity. Consequentially, the faster the vehicle, the higher the influence of external aerodynamic devices on the performance is. Both, drag and downforce are inseparably linked with each other. Producing downforce always entails aerodynamic resistance. The coefficient of both forces is calculated to evaluate the efficiency of the force generation (lift-to-drag ratio or aerodynamic efficiency).

Aerodynamic forces also influence the balance of the car and therefore, its handling. Simplified, all aerodynamic forces can be reduced to one force acting at a specific point, the center of pressure (CoP) or aerodynamic center. The correct position of the CoP is important to control low speed, transient, and high speed handling of the vehicle. Furthermore, the CoP does not remain static in its position. It migrates along the longitudinal and lateral axis with speed and vehicle motion (pitch and roll) which makes the positioning more difficult.

2.3. Race Track Analysis

FSAE cars run multiple disciplines throughout an event to evaluate their performance. For maximizing the performance, specific aerodynamic and suspension setups are run in each of the disciplines. Before designing an aerodynamic package for the car, track data must be analyzed. FSAE tracks in particular feature a high cornering percentage. Hence, the car spends more time in corners than on straights. This is an important factor when it comes to the dimensioning of the aerodynamic package and the respective downforce and drag coefficients.

The average speed is between $13 - 17 m/s$ depending on track and competition. For design and development purposes, the vehicle speed is divided into the following speed ranges [17]:

- Low speed: $5 - 10 m/s$ $(= 11.3 - 22.5 mph)$
- Mid-speed: $10 - 20 m/s$ $(= 22.5 - 45.0 mph)$
- High-speed: $20 - 30 m/s$ $(= 45.0 - 67.5 mph)$

All FSAE disciplines and the suggested aerodynamic setups are listed in Table 2 (p.31).

Table 2: Aerodynamic setup at different FSAE disciplines [2, 17]

Discipline	Aero Setup	Background
Acceleration (75pts.)	Low drag	Timed, 75m acceleration on straight line, maximum power output needed
Skid pad (75pts.)	Maximum downforce	Timed, low speed steady state cornering in 15.25m radius turn, maximum cornering performance needed
Autocross (150pts.)	Maximum downforce	Timed, single lap on race track, maximum cornering performance needed
Endurance (325pts.)/ Efficiency (100pts.)	High downforce, best efficiency	Timed and fuel consumption measured, 22km in multiple laps on race track, high cornering performance and good efficiency needed

3. On Track Testing

Simulations play a key role in the development and design of race cars. They are used to evaluate concepts and designs, improve part geometries, calculate forces, and find the best performance of the vehicle. However, simulations can just be as good as their input data. Thus, physical tests are necessary in order to know how well simulation results correlate with the real world data. These validation tests can then be used to adjust and interpret the existing model or results.

In the case of external aerodynamics, validation tests are most commonly done in wind tunnels. They provide steady and repeatable environmental conditions. However, wind tunnel testing is extremely expensive and the majority of FSAE teams cannot afford access to it. Furthermore, there is just a limited number of wind tunnels specifically designed for ground vehicles (rolling floor, ground boundary layer treatment) which are available for use in the United States.

An attractive cost-effective alternative to a wind tunnel session is coast-down testing. It is mainly used for drag coefficient validation but other aerodynamic coefficients can be obtained as well. This chapter is about the preparation, procedure and analysis of the driving tests. As part of the analysis, templates and math channels have been created for future use. A comparison of the real track data with the simulation results is shown later in this thesis (see chapter 4).

3.1. Static Testing and Test Preparation

Before the car is taken out to the test track, some tests and preparations are necessary to ensure an accurate data collection. Prior to every test, the suspension setup needs to be adjusted to achieve the best performance. Important parameters are [26]:

- Tire pressure
- Toe, camber
- Corner weights
- Ride height
- Wing positions and angle of attack (overall, main plane, and flaps)

Additionally, there are a number of sensors that are necessary to achieve all desired test data such as:

- Wheel speed sensors, GPS, Pitot-tube for vehicle speed
- Shock potentiometers for suspension movement and aerodynamic loads
- Steering angle sensor, throttle and brake pedal position for driver inputs
- Accelerometer for lateral and longitudinal acceleration
- Strain gauges for force measurements

Static testing is used for the evaluation of car specific parameters such as the reduced mass representing the rotational inertias, the position of the center of gravity and wheel loads through shock potentiometer readings.

3.1.1. Reduced Mass

For the calculation of longitudinal motion, the reduced mass is an important factor for the evaluation. It represents additional resistances that has be overcome when the car

accelerates or brakes. All rotating parts of a car have rotational inertias [3]. The inertia indicates the resistance of a body when it is rotated around an axis. Inertias can be reduced to a single value for the car or a group of parts. This combined inertia is converted into a mass that is then added to the static mass of the car and the new mass is known as total mass. From the coefficient of total mass and static mass, a characteristic factor λ is calculated which is used for further calculations [3].

In this thesis, the rotational inertias of the suspension (tires, rims, brake rotors, hubs, half shafts, and differential) and final drive (sprocket, drive sprocket, chain, and clutch) of the car are considered. Engaging the clutch for the rolling tests eliminates the resistance of the gearbox and engine. The final value is set to be $\lambda = 1.05$ according to previous measurements of the author [17].

3.1.2. Shock Potentiometer Calibration for Wheel Load and Ride Height

To measure vertical loads on the car, each spring and shock unit is equipped with a potentiometer that is mounted to the shock and duplicates its travel. Originally installed to measure the pure shock travel, the potentiometer data can also be combined with weight scale data to measure the wheel load [19]. The static testing is done with a variety of different loads represented by weight discs stacked on top of the car. The appropriate weight scale readings and shock potentiometer data are given in Figure 10 (p.35).

It is assumed that the dependence of sensor output with respect to the wheel load is linear as evaluated by the given trend lines. The test was repeated five times per weight case for statistical reliability. This procedure is repeated for ride height measurements and provides front and rear axle ride heights through a combination of the respective values.

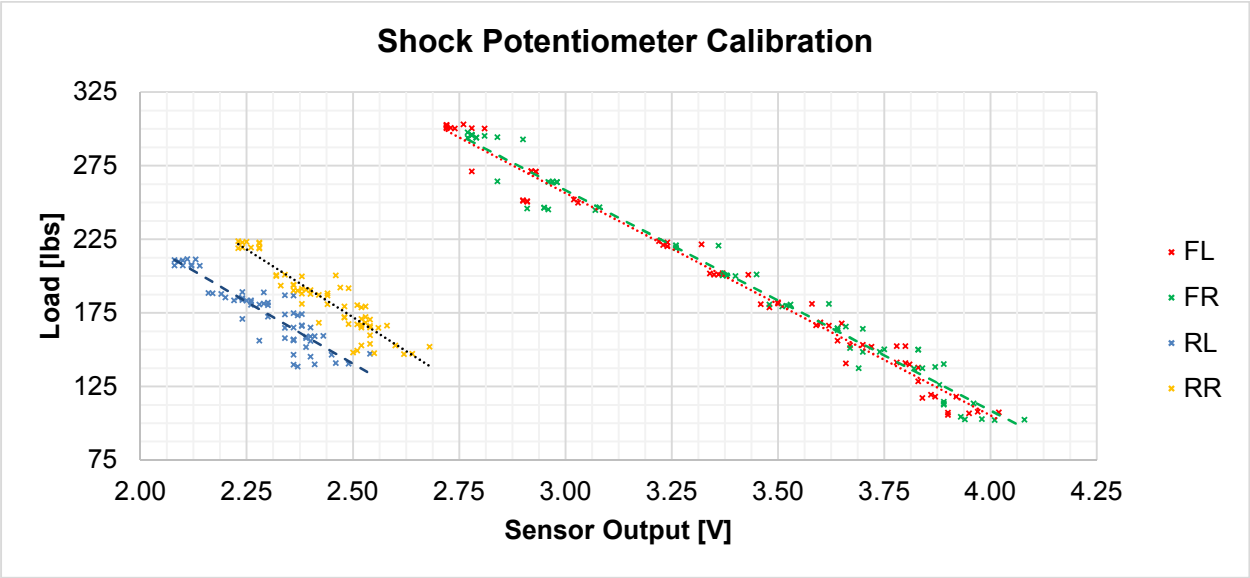

Figure 10: Shock potentiometer calibration

It is a fact that this method is not the as accurate as strain gauge measurements or wheel force transducer data. However, the shown method is easy to implement into the testing process and suitable for tests without fast weight transfer changes such as the coast-down test or the skid pad test. Strain gauges have been planned as a second method to measure the vertical loads of the car. However, by the time the tests were done strain gauges installed at the push/ pull rods did not function properly so that the shock potentiometers are the only method for determining the vertical load.

3.2. Coast-Down Testing

The coast-down test is a well-known method to measure aerodynamic coefficients without high expenses (wind tunnel) on the track. It is mainly used for studying drag and rolling resistance. In addition, downforce and its distribution can be calculated when the car is equipped with sensors to measure wheel loads. Without specific measuring methods like pressure sensors in the wing profiles, Pitot-tube arrays mounted to the car (as used in professional motorsports), “Flow-Viz” paint to visualize the air flow on surfaces, or strain

gauges at wing mounts, it is not possible to get further information about local flow schemes. Due to time and budget constraints, none of the listed methods could have been employed on the JMS14c.

The coast-down test presented in this thesis has been done on the taxi way at the municipal airport in Lawrence (KS) in June 2014. The example later on shows “run 1” of the June coast-down test with the JMS14c baseline wing setup and 8deg AoA of the main plane at the rear wing. All other test runs results have been calculated in the same way.

3.2.1. Preparation and Procedure

It is recommended to run a specific suspension setup for the coast-down test to minimize influences of all resistances but aerodynamic drag. For comparisons it is important to keep the testing conditions as constant as possible. Therefore, the track should feature at least a 500m long, straight lined and flat road [26]. The starting places and the coasting section of both directions should be clearly marked to ensure that the car runs always on the same place (see Figure 11).

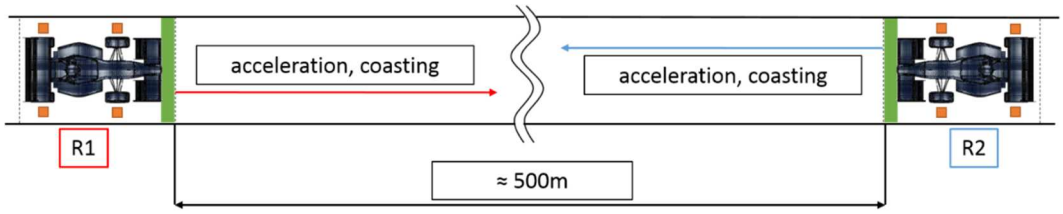

Figure 11: Coast-down testing

For setup changes, an even pit area should be marked. It has been helpful to use leveled corner weight scales where the car can be placed to adjust the setup.

The test is done in the following order:

1. Stop prior to every launch in pre-defined launch box (4 cones)

2. Launch the car and accelerate to top speed of ~33.5m/s (75mph)
3. Engage clutch and coast down to approximately ~7m/s (15mph)
4. Repeat test to have at least 4 runs per setup, 2 in each direction

In between the runs of different setups, the car should sit for a while to let the tires cool down.

3.2.2. Theory of Coasting Vehicle Dynamics and Example Calculation

During the coasting phase, the car ideally is in a pure longitudinal motion (no driver steering input, no side winds, and no banked straight). Engaging the clutch disconnects the power train from the driving wheels and eliminates the biggest source of friction losses. Hence, no driving forces are transmitted to the wheels anymore and only aerodynamic drag and rolling resistance forces slow down the car [3]. Consequently, the radial deformation of the tire contact patch is small which reduces the energy losses of the tire-ground interaction.

Furthermore, the tires are inflated to a higher pressure ($2.0bar \approx 30psi$) to limit the vertical tire deflection and keep the change of the dynamic tire radius small over the speed range (compression caused by high aerodynamic vertical loads). For the sake of simplicity, the dynamic tire radius is assumed to be constant with $r_{dyn} = 0.264m$ [17]. Also, a stiffer tire absorbs less energy through its own deformation (increases tire spring stiffness). Hence, higher loads are transmitted into the spring and shock system where the resulting compression can be recorded by the potentiometers.

Generally, a softer suspension setup (small spring rate/ stiffness) allows for more suspension travel of the shock potentiometer. More travel increases the accuracy of the measurement because of the greater difference in the sensor output between static (on

weight scales) and the dynamic (on the test-track) load. The initial breakaway force is smaller and therefore, small force variations can be detected much better. However, a soft suspension also causes greater changes of the ground clearance and pitch angle (negative acceleration) which affects the downforce generation (ground effect).

3.2.2.1. Calculation of Drag and Rolling Resistance

After accelerating the car to top speed and engaging the clutch, the car slows down because of internal friction, tire friction and air resistance. The energy (E) balance is given:

[3]
$$\frac{dE_{total}}{dt} = P_{drive} - \sum P_{loss} \tag{16}$$

[3]
$$E_{total} = E_{kin} + E_{pot} = E_{kin,trans} + E_{kin,rot} + E_{pot} \tag{17}$$

where E_{total} is the total energy of the system, E_{kin} is the kinetic energy with translational and rotational parts, E_{pot} is the potential energy, P_{drive} is the supplied power, and P_{loss} is the power responsible for efficiency losses (friction). The rotational term $E_{kin,rot}$ includes the energy that is necessary to spin a mass and increase the rotational speed (ω_{drive}) against the inertial resistance (I_{drive}). The energy is accumulated in form of a rotation. $E_{kin,trans}$ is the translational or longitudinal energy part.

[3]
$$E_{kin} = \frac{m_{stat}\, v^2}{2} + \sum \frac{I_j {\omega_j}^2}{2} = \frac{m_t\, v^2}{2} + \frac{I_{drive}\, {\omega_{drive}}^2}{2} = \frac{m_{red}\, v^2}{2} \tag{18}$$

[3]
$$E_{pot} = m_{stat} \cdot g \cdot h \tag{19}$$

Written as a balance of forces:

$$F_{R,acc} = F_{R,roll} + F_{R,air} + F_{R,grade} \tag{20}$$

$$m_{red} \frac{dv}{dt} = m\, g\, f_R\, cos(\alpha) + c_w \frac{\rho_{air}}{2} A_{face}\, v^2 + m_{stat}\, g\, sin(\alpha) \tag{21}$$

The rolling resistance coefficient is split into two parts to account for internal friction at different speeds ($f_{R,fric,1}$) and the tire rolling resistance ($f_{R,roll,0}$) that is assumed to be constant [12]. The coefficient is written as (see chapter 2):

$$f_R = f_{R,roll} + f_{R,fric} \cdot v \tag{22}$$

It is unlikely to do the test at absolutely perfect conditions without any wind and grade. To account for environmental influences, the wind speed and direction are measured [12].

$$v_{rel} = \sqrt{{v_{car}}^2 + 2vw\ cos(\delta) + w^2} \tag{23}$$

w – wind speed δ – wind direction

Assuming wind speed purely in driving direction, equation (21) extends to:

$$m_{red}\ \frac{dv}{dt} = a(t) = m_{sta}\ g\left(f_{R,roll} + f_{R,fric}\ v\right) cos(\alpha) + c_w\ \frac{\rho_{air}}{2}\ A_{face}\ (v+w)^2 + m_{stat}\ g\ sin(\alpha) \tag{24}$$

Prior to the calculation of coefficients, the acceleration must be obtained. In case of the JMS14c, all four wheel speeds are averaged to obtain the velocity of the coasting vehicle. The acceleration can then be derived from the speed. An example derivation of the acceleration can be seen in Figure 12.

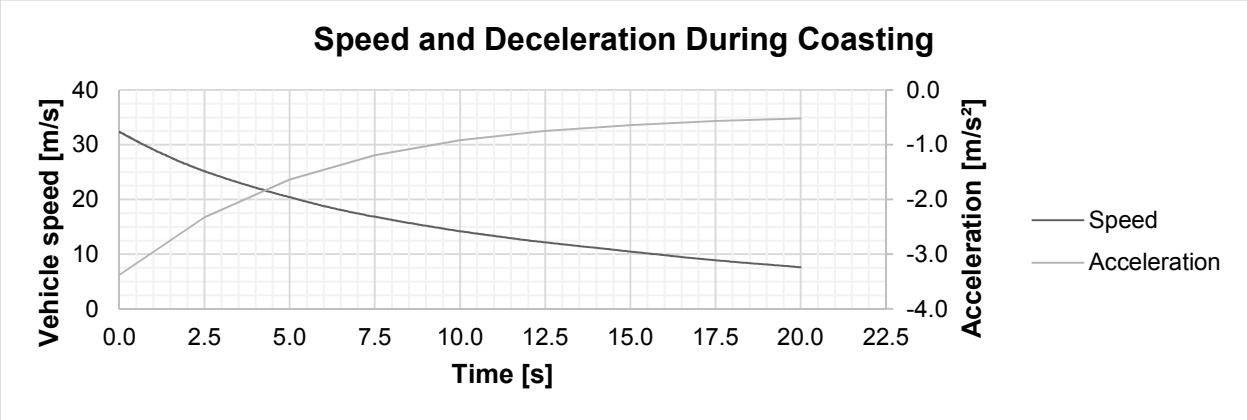

Figure 12: Derivation of recorded vehicle speed

The drag is calculated in two ways, by a first and second order approximation of speed and acceleration [3, 12, 17]. Both methods are compared in Figure 13.

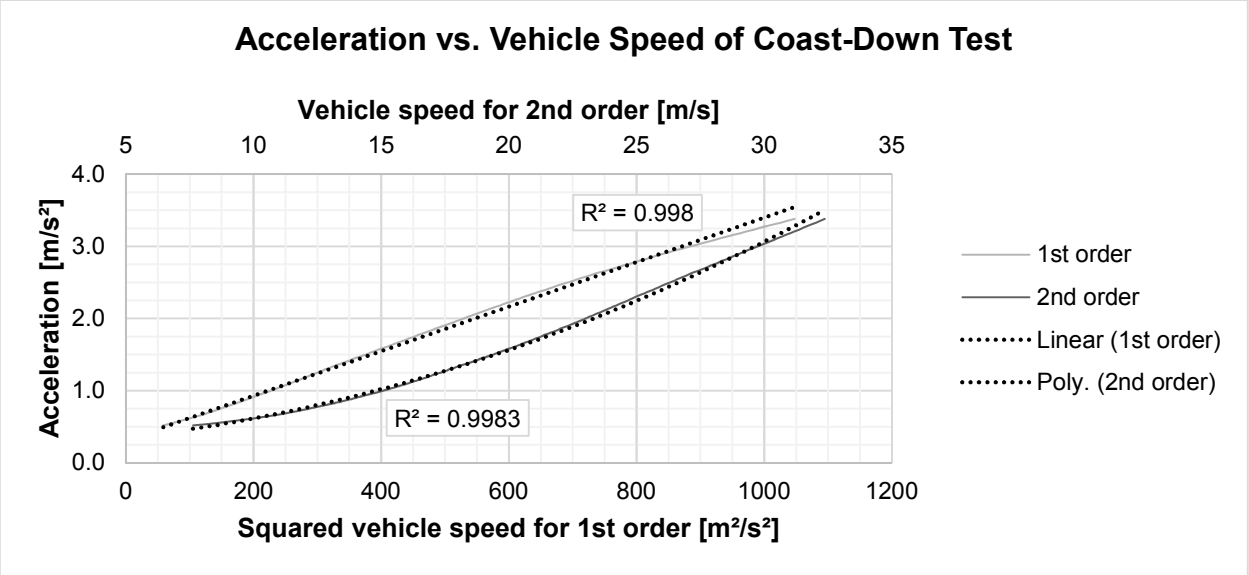

Figure 13: Comparison of 1st and 2nd order polynomial fit

1st order linear fit

For the linear approximation, the acceleration is plotted over the squared vehicle speed. The idea behind this method is that the function value of the trend line equation can be substituted by the acceleration and squared velocity to obtain a speed-dependent (drag resistance) and independent part (rolling resistance) of the vehicle resistances. The wind speed in this example is neglected.

It can be seen from the Figure 13 that the function is not exactly linear which implies that the drag coefficient varies over the speed range. To account for the differences in the drag generation over the speed, the regression line is split into multiple sections (see Figure 14, p.41).

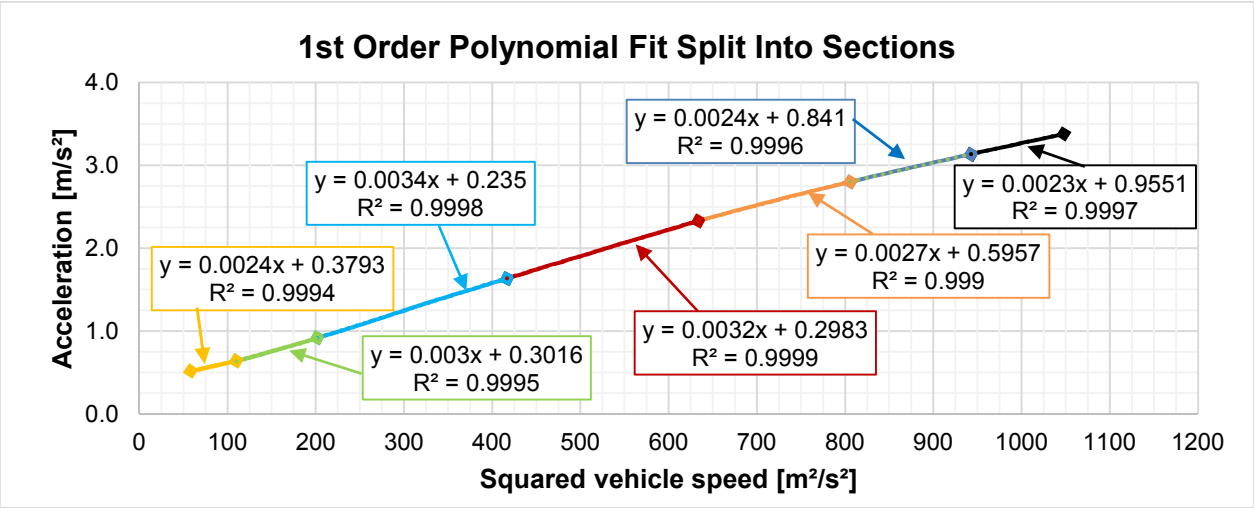

Figure 14: First order polynomial fit (regression) of vehicle speed vs acceleration

The regression line in general has a linear form of:

$$y(x) = m \cdot x + b \tag{25}$$

In the 1st order method, the dependent function value is:

$$y = a(v^2) \tag{26}$$

Substituting the function value into the regression line function results in a square function in the form of:

$$(v) = K_2 \cdot (v^2) + K_0 \tag{27}$$

K values are constants of the square function that result in the desired coefficients.

$$a(t) = \frac{dv}{dt} = \frac{1}{m_{red}} \cdot c_w \cdot \frac{\rho_{air}}{2} \cdot A_{face} \cdot v^2 + \frac{1}{m_{red}} \cdot m_{stat} \cdot g \cdot f_R \tag{28}$$

The constants K_2, K_0 and the desired coefficients c_w, f_R are determined by:

$$K_2 = \frac{1}{m_{red}} \cdot c_w \cdot \frac{\rho_{air}}{2} \cdot A_{face} \tag{29}$$

$$\rightarrow c_w = \frac{2 \cdot K_2 \cdot m_{red}}{\rho_{air} \cdot A_{face}} \tag{30}$$

$$K_0 = \frac{1}{m_{red}} \cdot m_{stat} \cdot g \cdot f_R \tag{31}$$

$$\rightarrow f_R = \frac{K_0 \cdot m_{red}}{m_{stat} \cdot g} \tag{32}$$

2nd order polynomial fit

The idea behind this method is similar to the 1st order method. The difference is that this method features an additional part which depends on the vehicle speed. The second order polynomial fit of the resulting curve has the form of:

$$a(v) = C_2 \cdot v^2 + C_1 \cdot v + C_0 \tag{33}$$

where C_2, C_1, C_0 are constants. Applying equation (24) to (33) and rewriting gives

$$\begin{aligned} a_x = \frac{1}{m_{red}} \Big\{ & \Big(c_D \frac{\rho_{air}}{2} A_{face} \Big) \cdot v^2 \\ & + \Big(m_{stat}\, g\, f_{R,fric}\, cos(\alpha) + c_D \frac{\rho_{air}}{2} A_{face}\, w \Big) \cdot v \\ & + \Big(m_{stat}\, g \Big(f_{R,roll}\, cos(\alpha) + sin(\alpha) \Big) + c_D \frac{\rho_{air}}{2} A_{face}\, w^2 \Big) \Big\} \end{aligned} \tag{34}$$

The constants are found by:

$$C_2 = \frac{1}{m_{red}} \Big(c_D \frac{\rho_{air}}{2} A_{face} \Big) \tag{35}$$

$$C_1 = \frac{1}{m_{red}} \Big(m_{stat}\, g\, f_{R,fric}\, cos(\alpha) + c_D \frac{\rho_{air}}{2} A_{face}\, w \Big) \tag{36}$$

$$C_0 = \frac{1}{m_{red}} \cdot \Big(m_{stat}\, g \Big(f_{R,roll}\, cos(\alpha) + sin(\alpha) \Big) + c_D \frac{\rho_{air}}{2} A_{face}\, w^2 \Big) \tag{37}$$

The equations (35) to (37) show that the wind speed and grade of the ground have influences on the rolling and frictional resistance of the coasting vehicle. However, the test is done consecutively on the same straight in both directions (to limit influences from changed wind speed and direction). The average of the results filters out influences from

wind speed and grade. Thus, neglecting the wind speed and grade influences, simplifies the equations to:

$$\rightarrow c_D = \frac{2 \cdot C_2 \cdot m_{red}}{\rho_{air} \cdot A_{face}} \tag{38}$$

$$\rightarrow f_{R,fric} = \frac{C_1 \cdot m_{red}}{m_{stat} \cdot g} \tag{39}$$

$$\rightarrow f_{R,roll} = \frac{C_0 \cdot m_{red}}{m_{stat} \cdot g} \tag{40}$$

Comparison

Choosing the correct method strongly depends on the available data set. The 2nd order method requires a wide range of speed data to appropriately represent the function of 2nd order due to its parabola shape. If just a small data section of the coasting period is available, then the shape of the function is better represented by a 1st order fit. The results of both methods are compared in Figure 15. For this thesis, the 2nd order method is chosen to be the preferred calculation of drag and rolling resistance. The tests provided enough data points to adopt the trend of a parabola of speed over time.

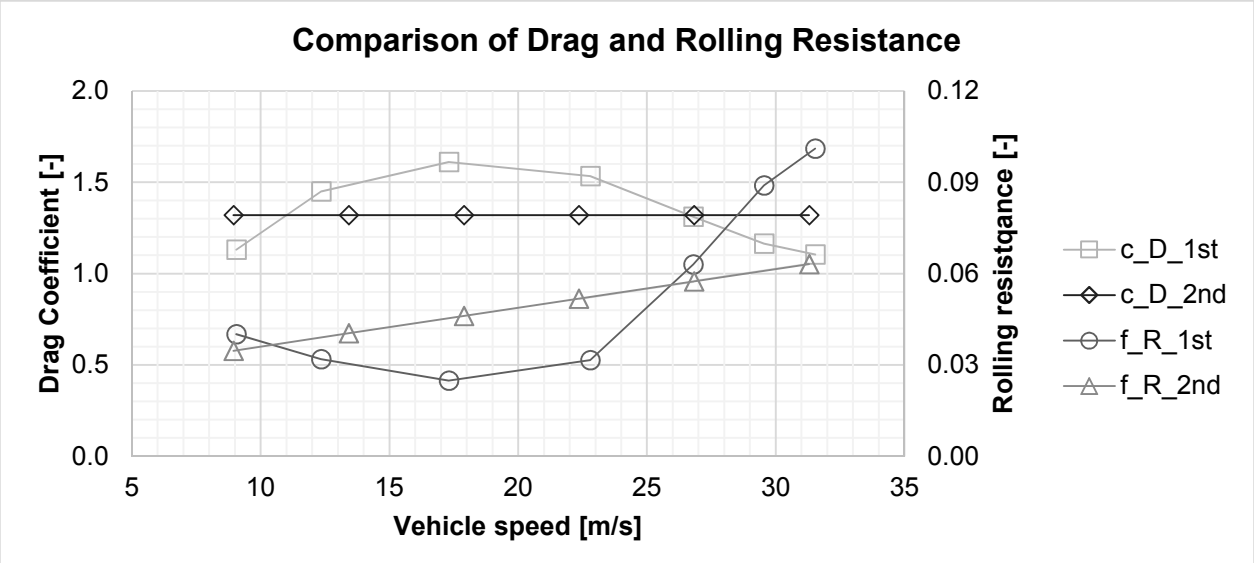

Figure 15: Comparison of 1st and 2nd polynomial fit

3.2.2.2. Calculation of Downforce

This section is about the calculation of the aerodynamic (vertical) load and its distribution between the front and rear axle (aerodynamic balance). The weight transfer caused by the pitch angle is determined by the acceleration, vehicle speed and drag. Under braking, accelerating or coasting, the car rotates around its pitch center in the direction of the front axle (negative angle). However, the body pitch angle is small and does not exceed $-0.8deg$ in deceleration and $+0.8deg$ in acceleration with respect to the ground. Therefore, an additional weight transfer caused by a geometric angle is negligible.

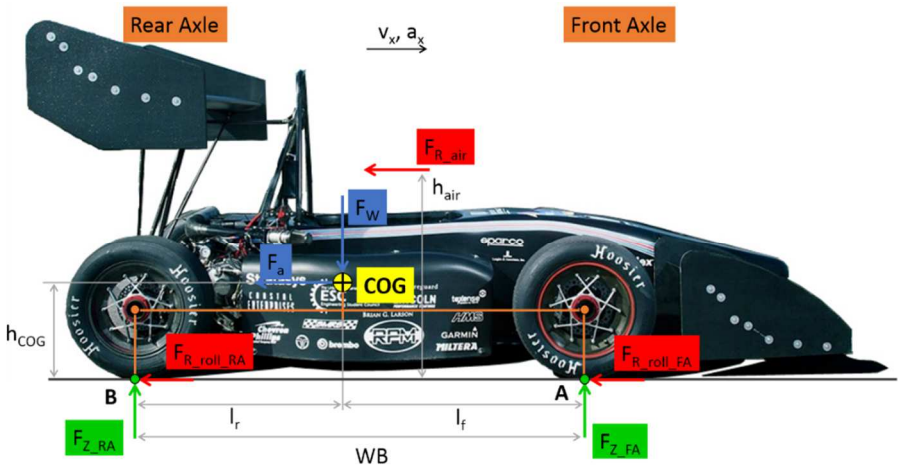

Figure 16: Balance of forces during coasting

The balance of forces according to Figure 16 is:

$$\circlearrowleft \text{A} \quad : 0 = F_G \cdot l_f + F_a \cdot h_{COG} + F_{R\_air} \cdot h_{COG} - F_{Z\_RA} \cdot l \tag{41}$$

$$0 = m_{stat} g \cdot l_f + \mathrm{m_{total}} \cdot a_x \cdot h_{COG} + c_w \cdot \frac{\rho_{air}}{2} \cdot A_{face} \cdot v^2 \cdot h_{COG} - F_{Z\_RA} \cdot l \tag{42}$$

$$\circlearrowleft \text{B} \quad : 0 = F_{Z\_FA} \cdot l + F_a \cdot h_{COG} + F_{R\_air} \cdot h_{COG} - F_G \cdot l_r \tag{43}$$

The vertical loads of rear and front axle are:

$$F_{Z\_RA} = \frac{1}{l}\left(m_{stat} \cdot g \cdot l_f + \mathrm{m_{total}} \cdot a_x \cdot h_{COG} + c_w \cdot \frac{\rho_{air}}{2} \cdot A_{face} \cdot v^2 \cdot h_{COG}\right) \tag{44}$$

$$F_{Z\_FA} = \frac{1}{l}(m_{stat} \cdot g \cdot l_r - m_{total} \cdot a_x \cdot h_{COG} - c_w \cdot \frac{\rho_{air}}{2} \cdot A_{face} \cdot v^2 \cdot h_{COG}) \quad (45)$$

The results of the example calculation are plotted in Figure 17. It can be seen that the difference in wheel load is about 5% from high-speed to low-speed.

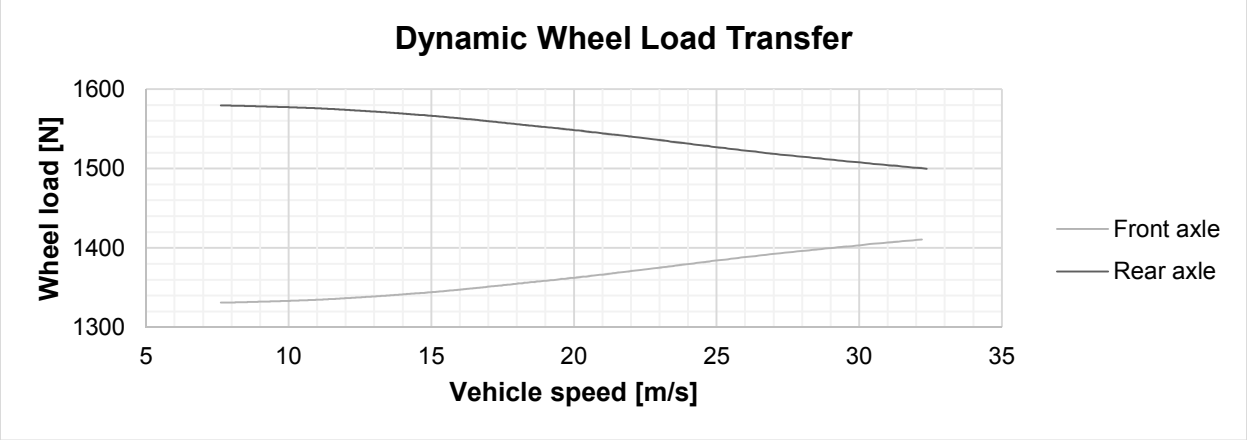

Figure 17: Dynamic weight transfer due to coasting

The downforce is then calculated by a subtraction of the calculated dynamic wheel load and the recorded wheel load data. A polynomial approximation of the fourth order is applied to the data of front and rear downforce as shown in Figure 18. The approximation filters noisy data and determines a function for further use in calculations. The total downforce is calculated as the summation of front and rear downforce.

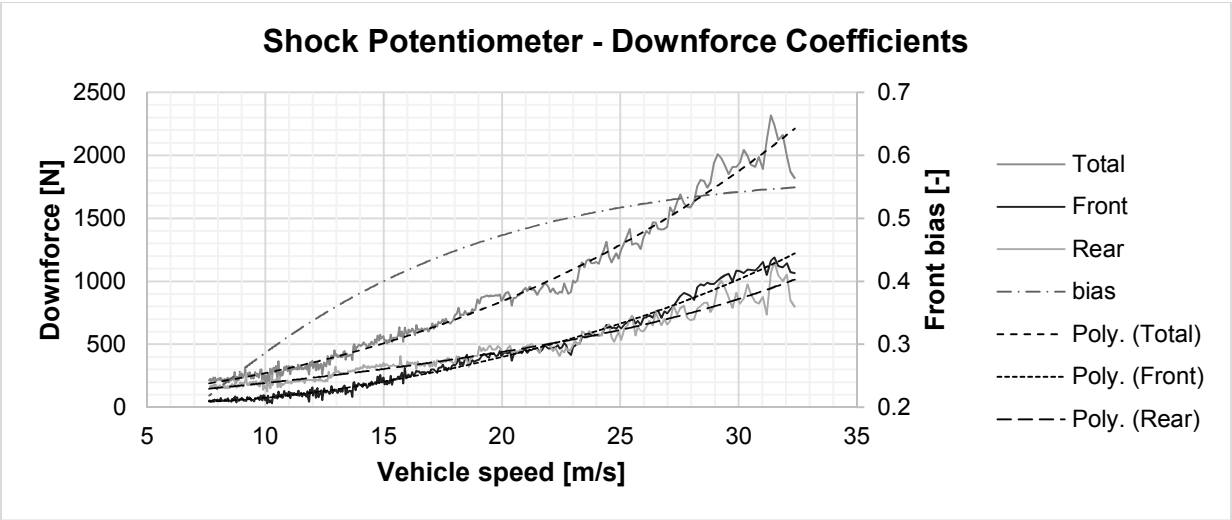

Figure 18: Polynomial approximation of calculated downforce

The respective coefficients of downforce of both axles are determined by equation (13) and are shown in Figure 19. A high deviation in the lower speed range is noticeable which is why only data above the speed range of $20m/s$ are used for an approximation of the downforce coefficients. Linear approximations based on high-speed data (dashed lines) are then used to obtain functions for the calculation of coefficients at different speeds.

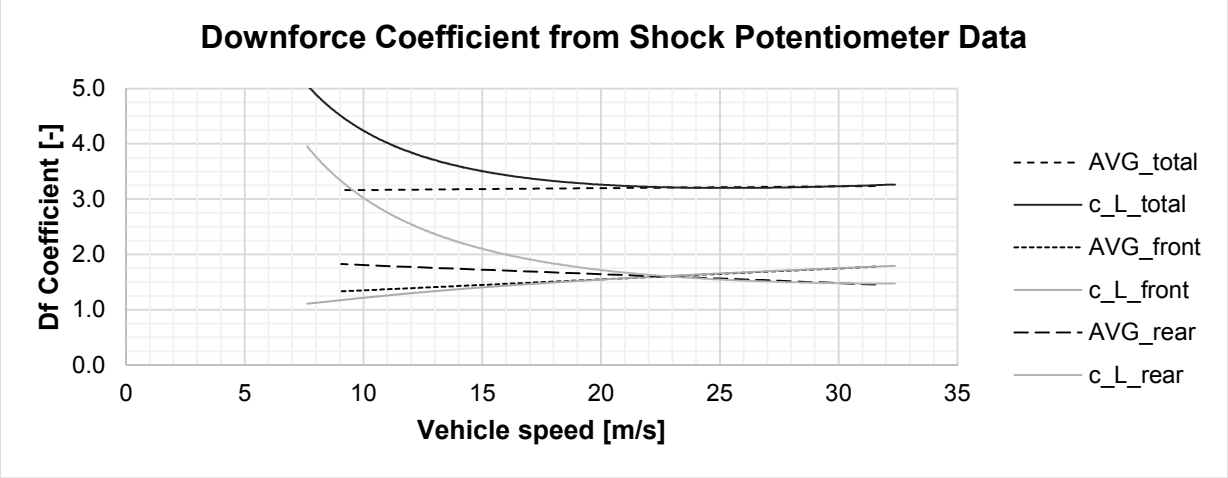

Figure 19: Downforce calculation at different velocities

The real forces of lift and drag are calculated over the entire speed range by equation (13) and (14) (see Figure 20). From the total downforce the front bias is calculated with:

$$Front\ bias = \frac{F_{Z\_FA}}{\left(F_{Z\_FA} + F_{Z\_RA}\right)} \tag{46}$$

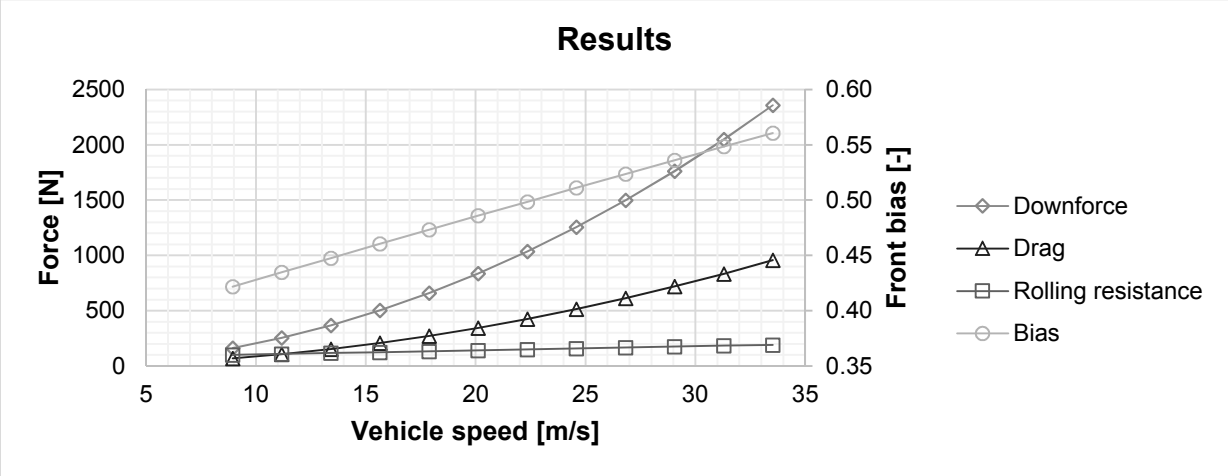

Figure 20: Downforce and drag force

3.2.2.3. Pitch Angle and Ride Height

As indicated in section 2.2.4, the downforce production of ground vehicles also depends on the position relative to the ground. The spring/ shock unit is compressed under high aerodynamic load which lowers the ride height of the car. Additionally, the car pitches towards the front axle which is caused by the dynamic weight transfer. Thus, the front wing might produce more downforce through ground effect (when no separation occurs) and shifts the aerodynamic balance towards the front of the car. More front downforce increases the pitch angle even more which further reduces the gap size and enhances the downforce production again. This interaction is counterbalanced by the spring stiffness so that the vertical load is in a balance with the produced spring/ shock force.

For the comparison of real track data and CFD simulation data, it is important that the correct ride height, pitch angle and front wing ground clearance are set in the model. Therefore, the ride height is obtained by the readings of the shock potentiometers and the pitch angle is calculated according to:

[27]
$$\gamma_{pitch} = atan\left(\frac{RH_{RA,dyn} - RH_{FA,dyn}}{WB}\right) \tag{47}$$

γ_{Pitch} – pitch angle
$RH_{RA,dyn}$ – dynamic rear ride height
$RH_{FA,dyn}$ – dynamic front ride height
WB – wheelbase

Moreover, a study [27] for the determination of the coefficients was performed (see Appendix B). The front wing ground clearance can be calculated by equation (64). The results of the example coast-down runs are plotted in Figure 21 (p.48).

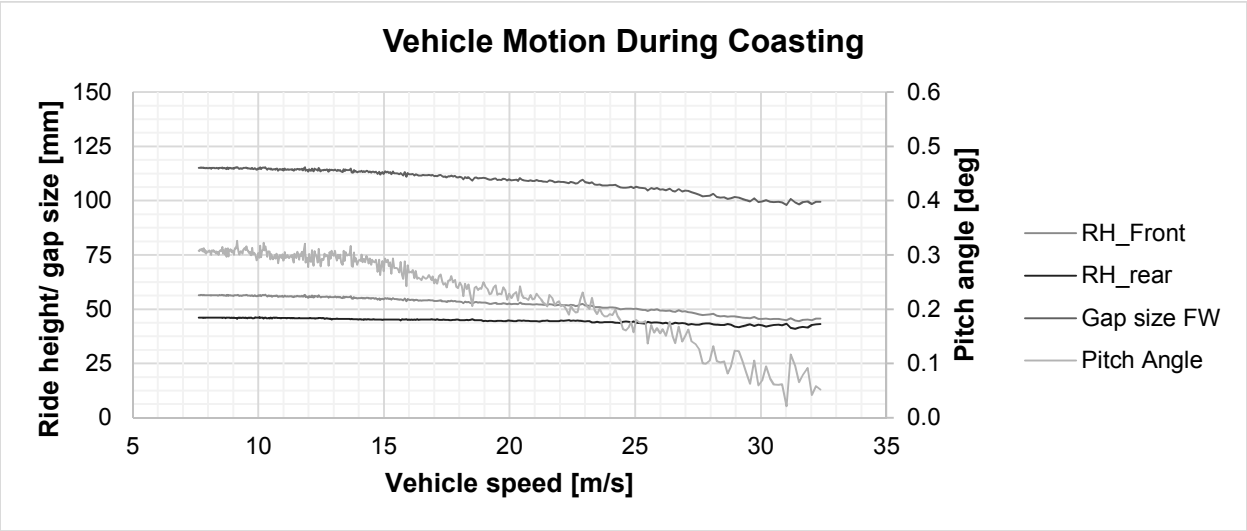

Figure 21: Pitch angle and ride height change of the coasting vehicle

In this particular example, it can be seen that the front and rear ride heights were not set equally. The problem results from the setup work. During the adjustments of ride height and corner weights, another person was sitting in the car. The ride height and balance changed when the driver sat in the car. This error shows how sensible the car reacts to small changes in driver position and weight. The pitch angle of the car in static condition is around 0.30deg and changes with high aerodynamic load to 0.05deg. The difference is 0.25deg towards the front axle. Furthermore, the gap between front wing and ground changes by approximately 12mm over the speed range.

3.2.3. Results

Coast-down test results of all other runs are calculated in the same way as it was shown in the previous section. Following, the results of all coast-down tests are plotted in Table 3 to 6 (p.49-52). Data of every run are shown next to the average of each setup and the respective standard deviation of the averaged data.

Table 3: Coast-down testing – downforce coefficients

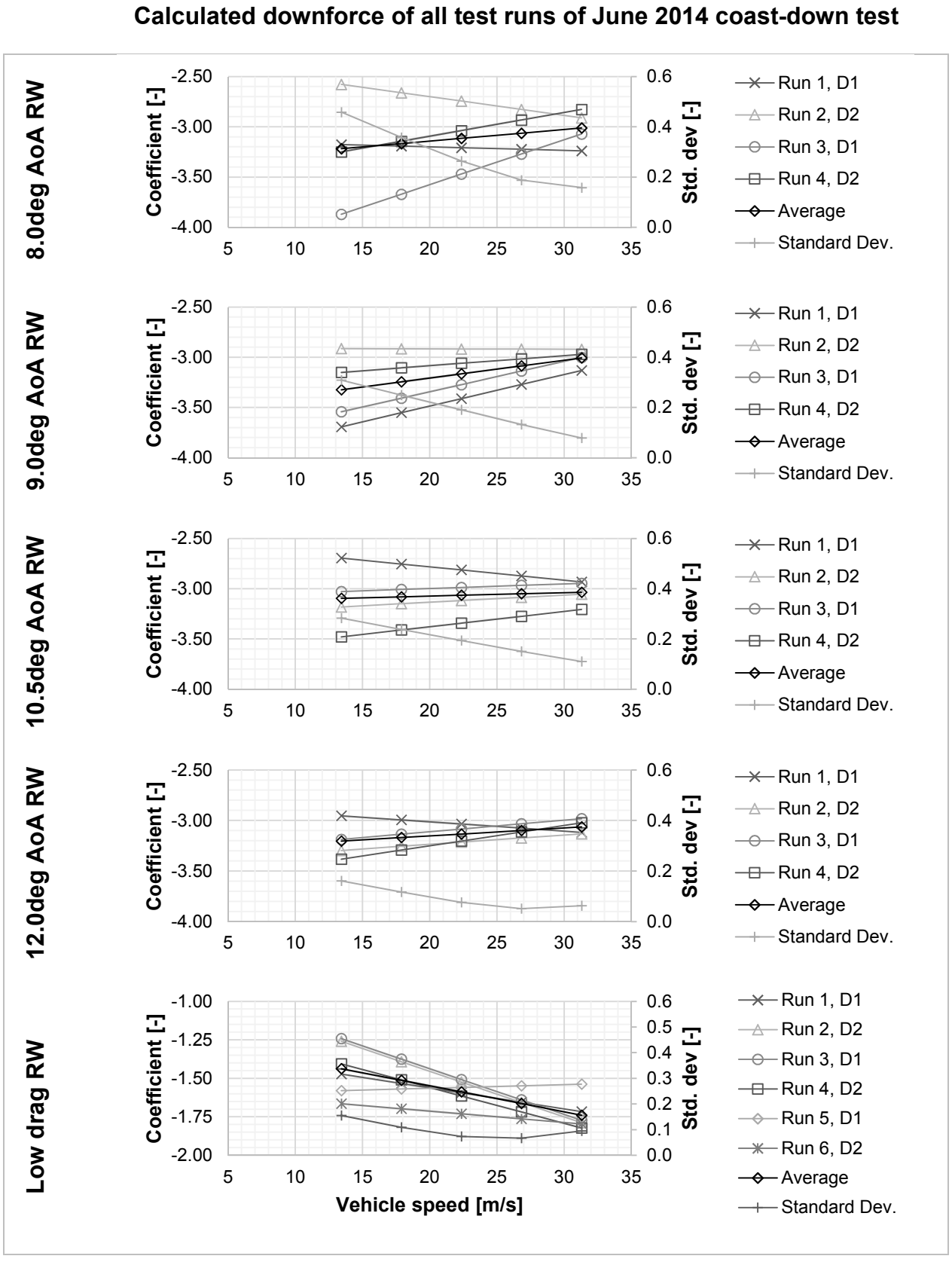

Table 4: Coast-down testing – rolling resistance coefficients

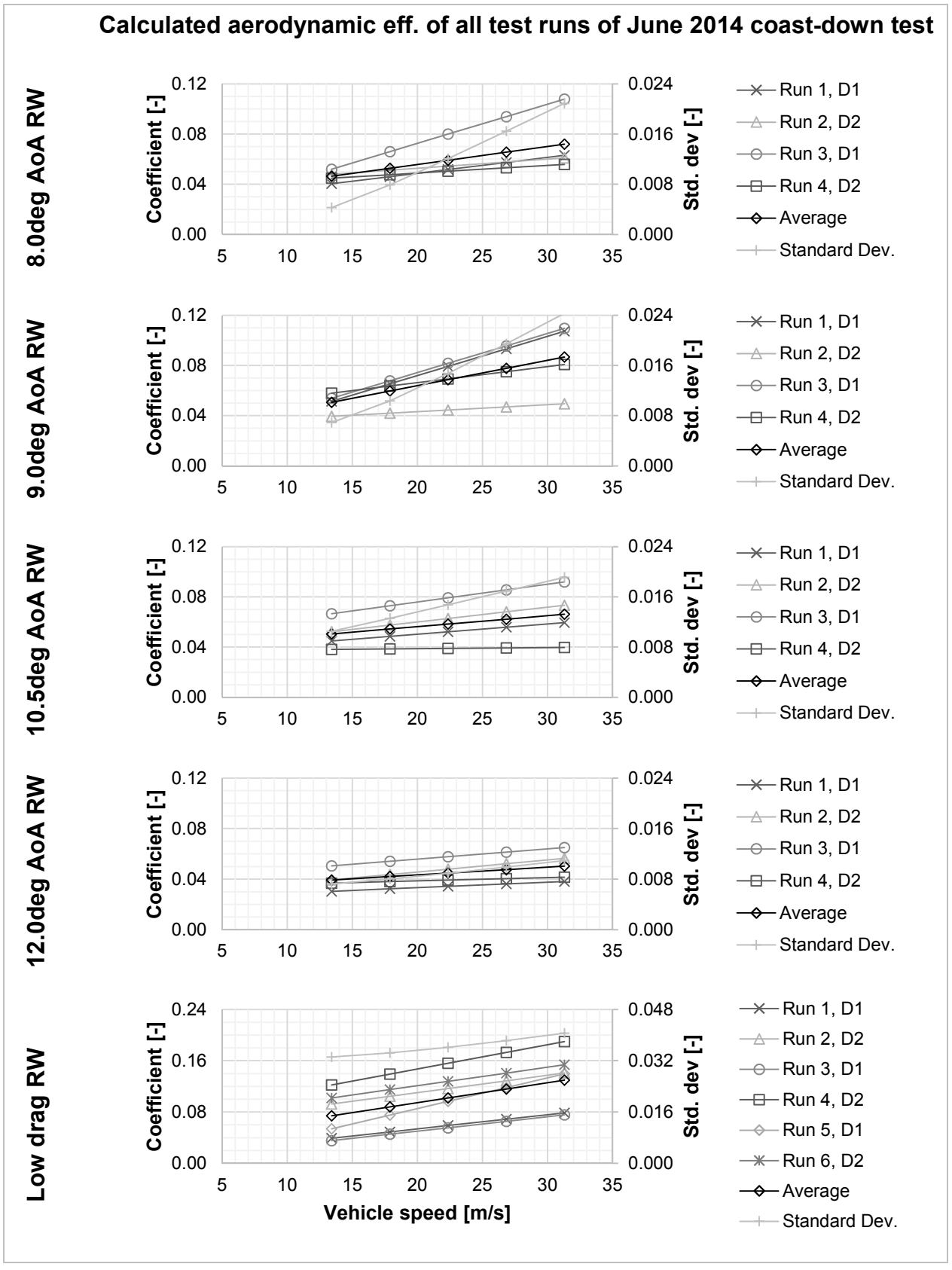

Table 5: Coast-down testing – front to rear bias coefficients

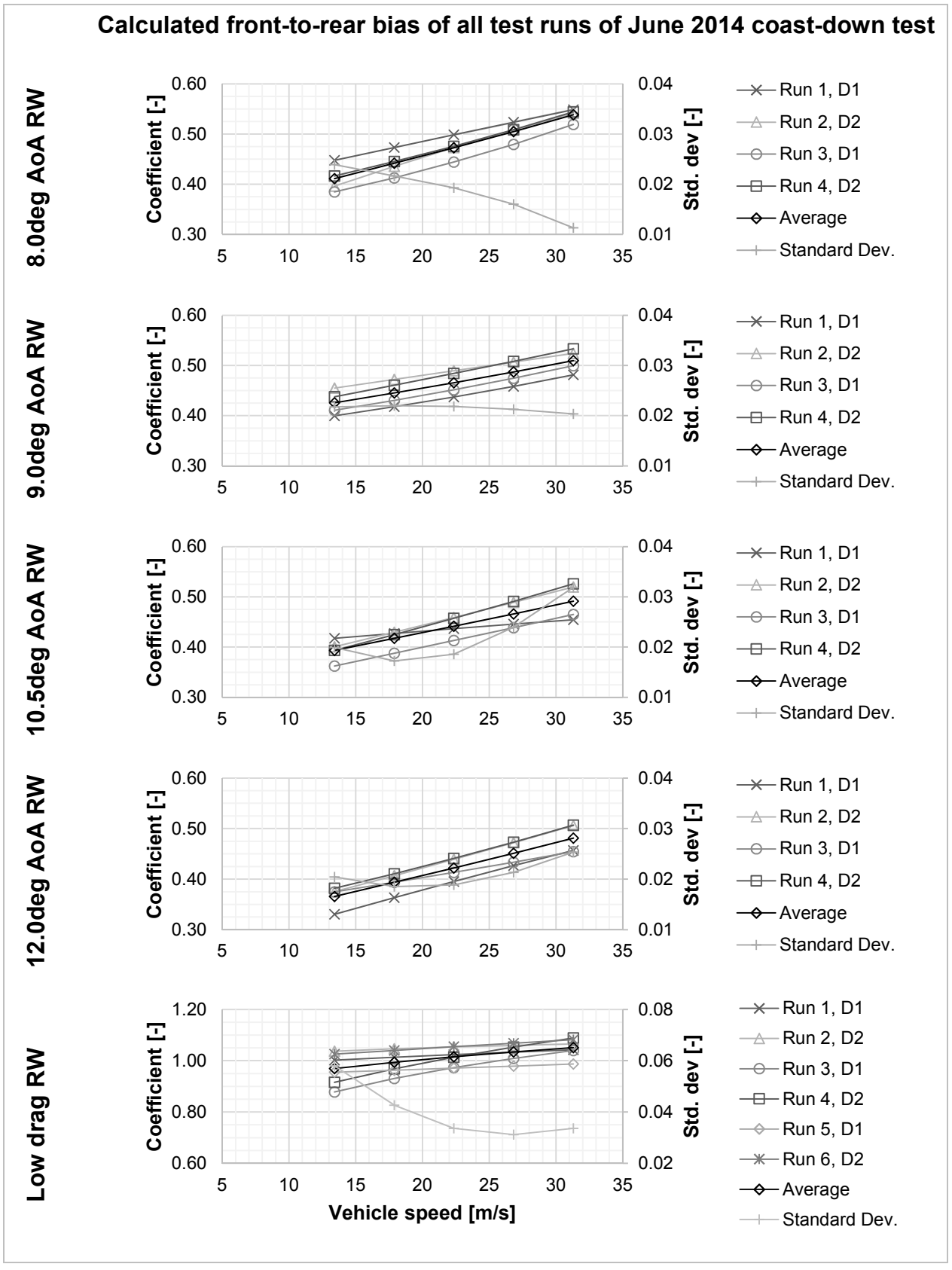

Table 6: Coast-down testing – drag coefficients

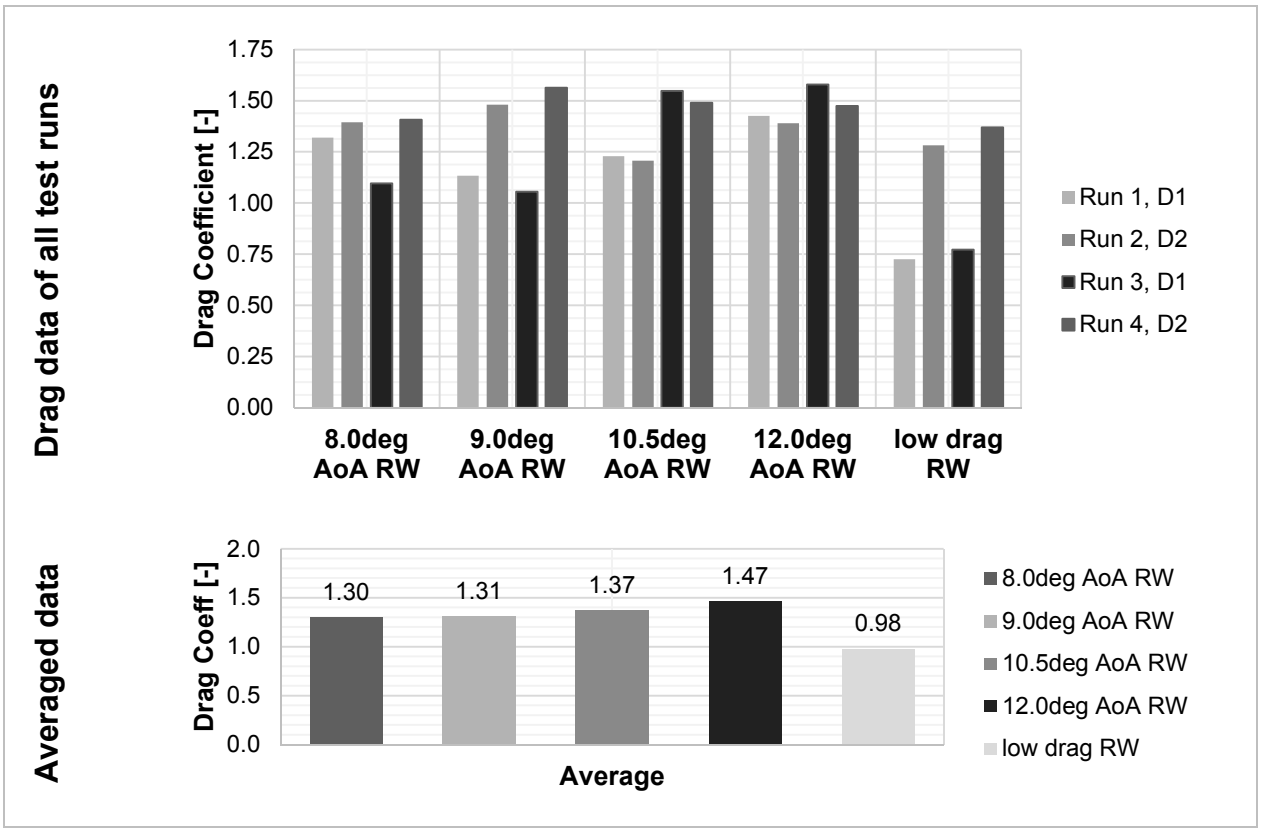

The presented data shows deviations of all runs per setup. The large deviation implies that multiple runs in both directions are necessary to account for all influences. The averaged results help to compensate for different grades of the road and for the influence of head or tailwind.

In Table 3 (p.49), the plots show that downforce results are more scattered in low-speed than in high-speed. This strengthens the assumption which was made earlier regarding the higher accuracy of downforce numbers in high-speed. Furthermore, it seems that steeper angle of attacks of the rear wing cause less scattering in downforce results than smaller angles. One of the reasons for that comes from the suspension design. The JMS14c features a greater motion ratio at the rear axle than at the front axle. The motion

ratio is the coefficient of wheel and shock displacement [28]. The higher the motion ratio, the higher the wheel displacement compared to the shock displacement is. Through a higher load on the rear axle (caused by an increased AoA of the rear wing), the suspension (shocks and springs) of the rear axle gets more compressed than the front axle. Thus, it uses a greater shock potentiometer travel and sensor range which helps to decrease the influence of sensor errors. A similar effect can be seen between the low and high-speed range in general. The increased vertical load at high-speed compresses the suspension more than in low-speed.

Regarding the front-to-rear bias, it is apparent that the front wing gains more downforce with higher speed than the rear wing (also in 12deg AoA setup). The low-speed range shows an aerodynamic balance of around 40/60 (front/rear) whereas the high-speed range has a 50/50 overall balance. This effect is potentially based on the lowered overall ride height under aerodynamic load and therefore, an increase of the ground effect. A 50/50 overall aerodynamic balance has its CoP in the center of the wheelbase. Appendix A shows that the center of gravity is located at approximately 46/54. The result is an oversteering balance in high-speed (CoP located in front of CoG). However, the balance does not represent the vehicle in general since the recorded driving condition is specific for coast-own tests.

By increasing the rear wing AoA, the overall balance shifted towards the rear. This behavior was expected but surprisingly, a change of 1deg AoA could be detected by the averaged results. The rolling resistance coefficients show the expected trend. Through the speed depending part of the frictional resistance, all setups increase the resistance over the entire speed range. Furthermore, less data scattering occurs with greater angle of attacks for the same reason as mentioned before.

3.2.4. Errors

The performed coast-down test has very likely multiple errors that influence the test results. However, it is almost impossible to ensure the same test conditions for all runs. Wind, bumpy surfaces, grade of the road, tire grip, and tire wear are the main influences that impact the results. It is nearly impossible to obtain numbers for these errors nor control them effectively. Tire grip can even change within the runs when the tires heat up and generate more grip. Thus, it is important to interpret all results with caution. The statistical reliability plays a key role in achieving valuable data. Averaging all results helps to account for some major influences like wind speed and grade of the track.

The ride height change cause inaccurate results as well. When the suspension (springs, shocks, tires, compliances) gets compressed under a high aerodynamic load then the ride height decreases. Although a soft suspension helps the accuracy of the measurement, it increases the interaction of front wing and undertray with the ground. Another influence arises from the method of wheel load measurement. Tires of open-wheel cars generate lift. This lift force is then measured as downforce relative to the movement of the body .

3.3. Future Work

For future validation work, strain gauges should be installed not only to the push and pull rods but also to all wing mounts. Their force prediction is more accurate than the shock-potentiometer method. The results could be further improved through more consecutive runs per setup (in total 10 runs). This would increase the statistical reliability significantly. An acceleration, high-speed or constant speed test could generate more helpful data for the evaluation of aerodynamic coefficients. Combined with engine dyno results and further efficiency measurements, coefficients of drag and downforce can be obtained.

4. Aerodynamic Simulations

This chapter presents the developed CFD model and simulation results. The work flow is divided into three steps: pre-processing, solving and post-processing. Each step will be described individually. Symmetry of the car is assumed and focus is put on a half car model (HCM) which consequentially can only represent straight line driving conditions. This assumption is based on the available computational resources which were limited to desktop PCs with 8GB of RAM and quad-core processors from the year 2013. The entire process of meshing, calculating, and post-processing should not last longer than 12 hours per simulation. Multiple PCs were available so that many different iterations with the developed model could be performed. In total, over 100 different simulation cases based on the initially developed CFD model were run. The following vehicle configurations are studied with the HCM simulation:

- Baseline model over the entire velocity range
- Aerodynamic sensitivities such as pitch angle and ride height
- Recorded coast down driving conditions

Other key interests of the simulation are:

- Parameter-based controls to adjust the CFD model for setup iterations,
- Interchangeability of parts for further design iterations
- Automatic post-processing macros

4.1. Numeric Simulations

The following sections briefly introduce the theory behind the numeric simulation of fluids.

4.1.1. Navier-Stokes Equations

Generally, numerical fluid mechanics are used to describe the physical flow by a mathematical model [29]. Inertia, pressure, velocity, and viscosity of the fluid are considered. The governing equations represent the three-dimensional fluid flow, heat transfer and energy exchange by the laws of conservation of mass, momentum and energy [29]. In external aerodynamics of ground vehicles, the flow is treated as incompressible (flow velocity below Mach 0.3 [9]) and isothermal (no heat transfer effects [9]). Therefore, the energy equation can be neglected. The temperature as well as density are defined as ambient constants. Thus, the incompressible continuity equation (mass conservation) is written as:

[7]

$$\text{general form: } \nabla V = 0$$

$$\frac{\partial u}{\partial x} + \frac{\partial v}{\partial y} + \frac{\partial w}{\partial z} = 0 \tag{48}$$

The momentum equations are referred to as (incompressible) Navier-Stokes (NS) equations and are written in Cartesian coordinates:

[7]

$$\text{general form: } \rho g - \nabla p + \mu \nabla^2 V = \rho \frac{dV}{dt}$$

$$\rho g_x - \frac{\partial p}{\partial x} + \mu \left(\frac{\partial^2 u}{\partial x^2} + \frac{\partial^2 u}{\partial y^2} + \frac{\partial^2 u}{\partial z^2} \right) = \rho \frac{du}{dt}$$

$$\rho g_y - \frac{\partial p}{\partial y} + \mu \left(\frac{\partial^2 v}{\partial x^2} + \frac{\partial^2 v}{\partial y^2} + \frac{\partial^2 v}{\partial z^2} \right) = \rho \frac{dv}{dt} \tag{49}$$

$$\rho g_z - \frac{\partial p}{\partial z} + \mu \left(\frac{\partial^2 w}{\partial x^2} + \frac{\partial^2 w}{\partial y^2} + \frac{\partial^2 w}{\partial z^2} \right) = \rho \frac{dw}{dt}$$

V – velocity field
u, v, w – local flow velocity in x, y, z-direction respectively
x, y, z – 1st,2nd,3rd Cartesian coordinate
t – time
p – pressure
μ – dynamic viscosity
ρ – density
g – gravity constant

The NS equations are second order non-linear partial differential equations which cannot be solved analytically due to the limited number of known coefficients. Mathematically, it represents a boundary value problem which is then numerically integrated in a finite number of control volumes (computational grid) and solved by default boundary values with an iterative approach [7]. The key problem in solving the NS equations is the turbulence model in order to accurately represent the physical flow.

4.1.2. Turbulence Modelling and Near-Wall Functions

Corrsin [30] has defined turbulence by: “Incompressible hydrodynamic turbulence is a spatially complex distribution of vorticity which adverts itself in a chaotic manner […]. The vorticity field is random in both space and time, and exhibits a wide and continuous distribution of length and time scales.” In flow with high Reynolds numbers (Re>4000), turbulence can occur because the viscosity of the fluid cannot dampen the turbulent fluctuations of fluid particles anymore [10]. Turbulent flow can have a chaotic and unorganized appearances which makes it difficult to predict [7].

The Reynolds-Average-Navier-Stokes model (RANS) is one of the most commonly used models to solve the NS equations [7] and is also referred to as Reynolds decomposition. The terms of the NS equation are rewritten as time-averaged terms. The instantaneous

velocity and pressure are split into an averaged (mean) and a fluctuating part [7]. The averaged part is:

[31]
$$\bar{u} = \frac{1}{T}\int_0^T u\, dt \tag{50}$$

The fluctuating terms is the deviation from the time averaged value and is written as:

[31]
$$u' = u - \bar{u} \tag{51}$$

Similarly, all other properties are split into the two parts as well.

[31]
$$\begin{aligned} u &= \bar{u} + u' \\ v &= \bar{v} + v' \\ w &= \bar{w} + w' \\ p &= \bar{p} + p' \end{aligned} \tag{52}$$

Both terms of the properties are now substituted back into the NS equations. There are just time-averaged and fluctuating terms left in the final equations. These parts are referred to as turbulent (Reynolds) stresses. The equation of the momentum in x-direction is written as (similar in y and z-direction):

[31]
$$\begin{aligned} \rho\frac{d\bar{u}}{dt} = \rho g_x - \frac{\partial \bar{p}}{\partial x} + \frac{\partial}{\partial x}\left(\mu\frac{\partial \bar{u}}{\partial x} - \rho\overline{u'^2}\right) \\ + \frac{\partial}{\partial y}\left(\mu\frac{\partial \bar{u}}{\partial y} - \rho\overline{u'v'}\right) + \frac{\partial}{\partial z}\left(\mu\frac{\partial \bar{u}}{\partial z} - \rho\overline{u'w'}\right) \end{aligned} \tag{53}$$

Because of the unknown turbulent stress terms, it is not possible to solve these equations analytically. Therefore, a turbulence model is used to make assumptions about the flow's behavior [32]. The most common one is known as Eddy Viscosity Model. It uses an isotropic value for the turbulent viscosity value whereas other models like the Reynolds Stress Model (RSM) uses 6 separate Reynolds stresses for an anisotropic solution (more accurate but more computational power/ time needed) [32]. Further developed and well-

known Eddy Viscosity Models are [31]: (1) Spalart-Allmaras, (2) k-ε (epsilon) model, (3) k-ω (omega) model, (4) $v^2 - f$ model, (5) Reynolds stress model (RSM), (6) detached eddy simulation model (DES), and (7) Large eddy simulation (LES) model. With the available computational resources of JMS, the latter four models are not realizable. The Spalart-Allmaras model (1) is a single equation turbulence model that has been designed for low Reynolds number flows and very fine near wall meshes with desired wall y+ values in the order of $y^+ = 1$. The k-ε (epsilon) model (2) is widely used in industry and covers a wide range of different flows [33]. However, it is not recommended for flow types where separation and strong vortices are expected (race car wings, rotating tires). The k-ω (omega) model (3) offers reasonable results for low Reynolds number flows, shear flows and separation [33]. Furthermore, a seminar held specifically for the computational simulation of race car aerodynamics [33] suggests the usage of the k-ω (omega) model in FSAE race car application. Through the expected separation and highly turbulent flow areas around tires and wings, the k-ω (omega) model was chosen for the CFD model of this thesis.

Along with the turbulence model, a near-wall treatment model is used to represent the flow close to the wall (boundary layer). A non-dimensional coefficient is calculated to distinguish the type of boundary layer. The Reynolds number Re describes the ratio between inertial and viscous (friction) forces [1] and is expressed as follows:

[1]

$$Re = \frac{\rho V L}{\mu} \tag{54}$$

ρ – density of the fluid
V –velocity
L –characteristic length
μ – kinematic viscosity of the fluid

For Formula SAE race cars in general, Reynolds numbers range from 200,000 to 600,000 depending on the velocity [18]. Based on the characteristic Reynolds number, boundary layers are either laminar, transient or turbulent (see Figure 22). Because of high Reynolds numbers of the model, all boundary layers are assumed to be turbulent.

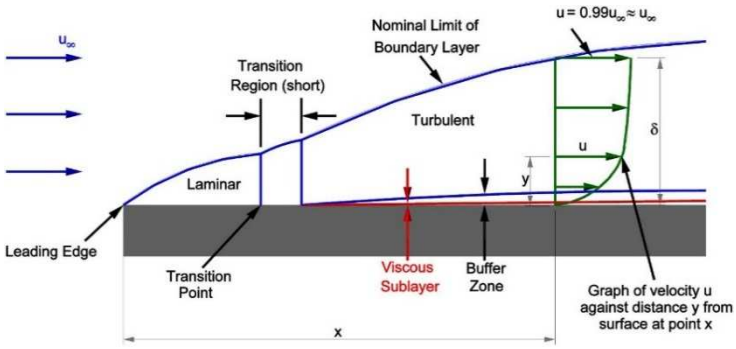

Figure 22: Boundary layer – laminar, transition and turbulent zones [35]

For near-wall modelling, a dimensionless distance and velocity are introduced:

[36]
$$y^+ = \frac{u^* d}{\nu} \tag{55}$$

[36]
$$u^+ = \frac{u_{||}}{u^*} \tag{56}$$

[36]
$$u^* = \sqrt{\tau_w} \tag{57}$$

y^+ – dimensionless (normalized) distance normal to the wall
u^+ – dimensionless (normalized) velocity
$u_{||}$ – velocity parallel to the boundary
u^* – friction velocity
ν – kinematic viscosity

As the flow moves past the vehicle, there is an interaction of fluid molecules with the surface. Due to shear forces that act between fluid particles and the wall surface (referred as to viscous effects), the first layer of the fluid molecules above the wall sticks to the surface. The velocity is zero (no-slip condition) [31]. Shear forces in the above layers decrease gradually whereas the velocity gradually increases until the flow reaches the

same velocity as the surrounding flow region. All layers with reduced velocities above a surface are referred to as boundary layer and cause the skin friction drag [31].

According to Figure 23 (p.62), the boundary layer is split into different regions which are influenced by viscous and turbulent shear stress effects. The three inner and one outer regions are [8]:

- Viscous sub-layer: $y^+ \leq 5$

  The viscous sub layer is an extremely thin layer above the wall surface where the no-slip condition is applied. The viscous shear stress is dominant and causes turbulent eddying motions to stop. Thus, turbulent fluctuations are damped and turbulent shear stress can be neglected. Due to its thinness, it is assumed that the shear stress is approximately constant and equal to the wall shear stress. The flow is nearly laminar and the following relationship holds:

[8] $$u^+ = y^+ \tag{58}$$

- Buffer layer: $5 \leq y^+ \leq 30$

  The buffer layer has an unknown distribution of viscous and turbulent stresses.

- Logarithmic layer: $30 \leq y^+ \leq 500$

  The velocity in this layer is approximated with the logarithm of the distance to the wall surface. Turbulent stresses are dominant but viscous stresses are still present. The following relation between wall distance and velocity is

[8] $$u^+ = \frac{1}{\kappa} y^+ + B = \frac{1}{\kappa} lnEy^+ \tag{59}$$

Where the universal constants depend on the roughness of the wall. For a smooth wall, the constants are $\kappa = 0.4$, $B = 5.5$ and $E = 9.8$.

- Outer layer: $y^+ \geq 500$

  In the outer region, the flow is dominated by its inertia where viscous effects are negligible. The layer is far away from the wall and holds the following relation:

[8]
$$\frac{U_{max} - U}{u_\tau} = \frac{1}{\kappa} ln \frac{y}{\delta} + A \tag{60}$$

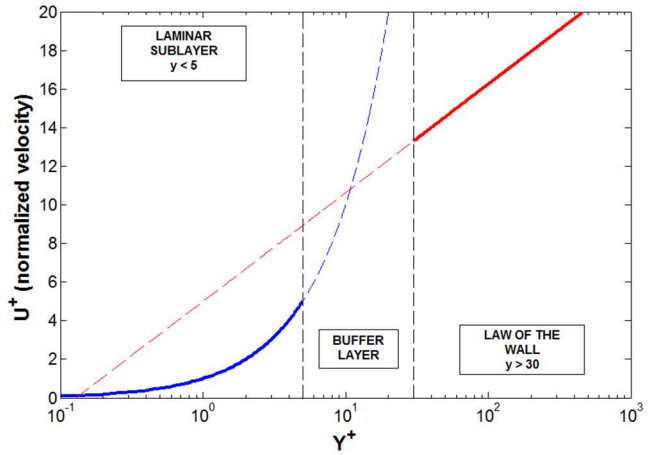

Figure 23: Wall function, wall y+ functions [32]

The three parts of the inner region (viscous, buffer and log-law layer) form just 10-20% of the total boundary layer thickness [8]. Thus, a very fine mesh structure close to the wall is necessary for a good flow representation. In flow schemes with a high chance of separation, a fine representation with low wall y+ values is recommended [33]. The point of separation can be solved more accurately which affects the drag and downforce estimation for race car applications [9]. With the intention of resolving the laminar sublayer, the value should ideally be $y^+ \leq 1$. However, to reduce the computational demand, values of $y^+ \leq 5$ are acceptable as well [33]. Furthermore, [33] suggests to use at least 10 boundary layers that have to be adapted in their thickness based on the prevalent flow

velocities and characteristic length of the part. More accurate boundary layer representations are expected with 15 to 20 layers above the wall. However, because of fine surface meshes in the computational model, a large number of prism layers increase the overall cell number drastically. Therefore, multiple boundary layer treatments over the entire model are used.

4.1.3. Flow Separation

The boundary layer is formed along the surface of the immersed body and develops the characteristic velocity profile within the layer. Further downstream along the wall, the pressure gradient dp/dx starts to drop. The flow detaches from the wall surface and forms an eddy when the pressure gradient (slope) reaches zero (velocity profile reverses). According to Prandtl [37], the reason for the flow separation is a significant loss of momentum close to the wall surface. From the continuity equation (48), the momentum equation (49), and the boundary condition $u = v = 0$ at the wall, the pressure gradient along the wall is calculated by:

[37]
$$\left.\frac{\partial \tau}{\partial y}\right|_{wall} = \mu \left.\frac{\partial^2 u}{\partial y^2}\right|_{wall} = -\rho V \frac{dV}{dx} = \frac{dp}{dx} \tag{61}$$

After the separation on edges, a large and highly turbulent wake region is formed. Flow that detaches from a surface as shown in Figure 24 often forms a trailing vortex in streamwise direction. The strong circulation creates the induced drag portion.

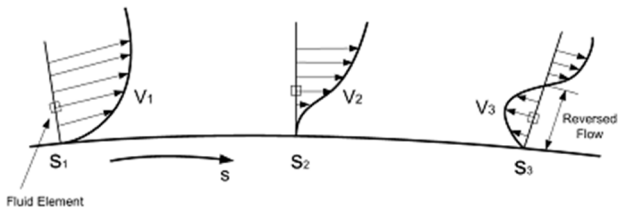

Figure 24: Flow separation, velocity profile of boundary [37]

4.2. Computational Fluid Dynamics

The computational simulations are carried out by the commercial CFD software package StarCCM+ v9.04 of cd-Adapco©. For FSAE aerodynamic design, it is found that the use of a commercial package provides good results within a short training period. This chapter describes the setup of the computational simulation and the baseline model.

4.2.1. Pre-Processing

The fluid sub domain with the model is set up in the pre-processing stage. The size of the sub domain depends on the flow velocity and the complexity in terms of flow direction changes through the geometry. It should be big enough to capture all major flow field influences around the vehicle and do not interact through the walls with the flow.

4.2.1.1. Fluid Sub Domain

The height and width of the sub domain is chosen based on the blockage ratio. In general, literature suggests a ratio of 1 to 5% [33]. The frontal face of the model is 2.1% of the size of the sub domain frontal face. The domain dimensions and outer dimensions of the JMS14c are shown in Figure 25.

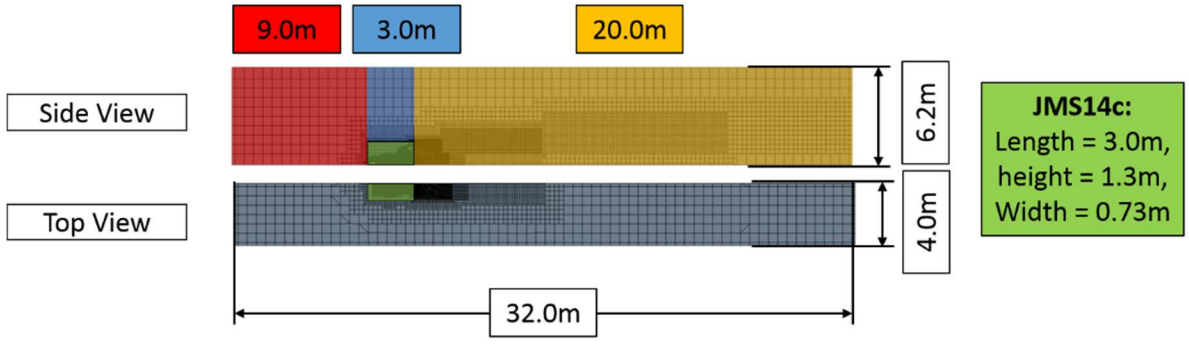

Figure 25: Setup and basic dimensions of fluid sub domain and JMS14c

4.2.1.2. Geometry

Based on the JMS14c Solidworks© model, a simplified CAD (computer-aided design)-model is created to reduce the computational requirements. All parts which do not significantly affect the flow scheme or add disturbance can be replaced or simplified. Simplifications include: closing holes/ openings, replacing complicated CAD geometry, and deleting unnecessary parts. The level of simplification strongly depends on the desired accuracy. For this thesis, major changes are made to the following parts of the JMS14c:

- Monocoque: closed cockpit opening and deleted all inside parts, filled mainhoop
- Driver: dummy model of helmet, neck, arms, torso and steering wheel
- Engine and intake: modeled as a single part for a simple representation
- Suspension: simplified a-arms, push/ pull rods, half shafts, wheel hubs, and uprights
- Wings: filled wings, no mounts
- Radiator and exhaust: simplified, radiator shape includes fan shroud and fan
- Wheels: closed rims and tires; wheel fairings at contact patch (see Figure 26)

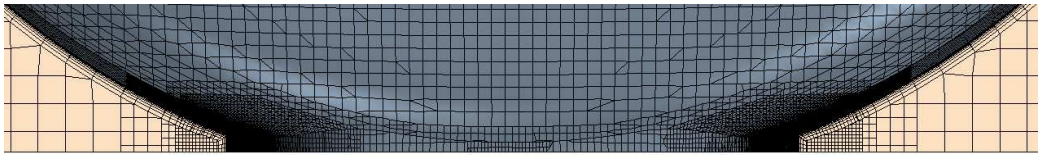

Figure 26: Wheel fairing and mesh around the tire contact patch

The final (CFD-ready) CAD model is shown in Figure 27 (p.66).

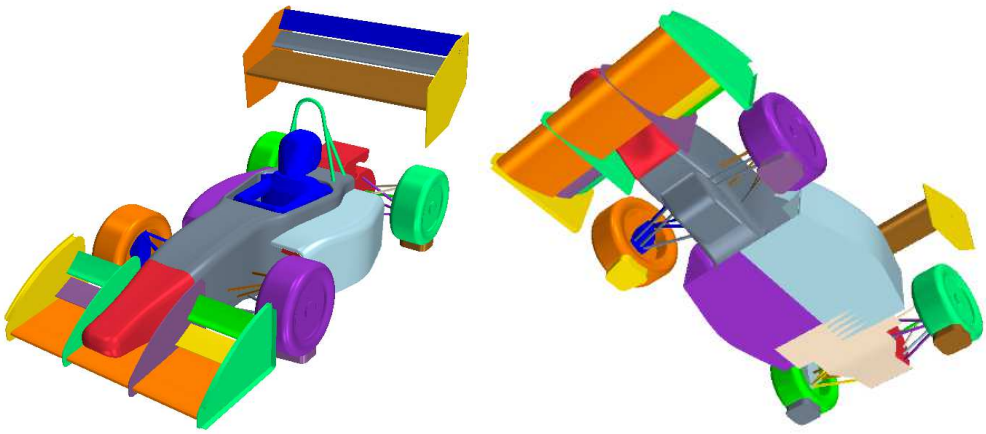

Figure 27: CAD-CFD model of JSM14c (colors represent distinguished parts)

It is important to create a good and clean CAD model in order to reduce meshing effort and achieve a high quality mesh. For interchangeable parts such as wings and endplates, the physical connection in the CAD model should be kept with a overlap for further work within the CFD software. The simplified CAD model is then imported into STAR CCM+.

4.2.1.3. Meshing

The type of mesh should be carefully chosen with respect to available computational resources, required numerical accuracy, and the complexity of the model geometry. The following grid types are used [31]:

1. **Structured grid** based on hexahedral cells, two different types:

   The rectangular sub domain is divided into smaller rectangular elements with faces parallel to the sub domain boundaries (first type). The second type is used for discretization of complex geometry through the deformation of grid elements (for instance, prism layers around a body).

   The advantages are less numerical diffusion through the alignment with the flow direction and a better cell density control. Structured grids struggle to represent complex geometry and thus, can produce low quality cells close to the wall

2. **Unstructured grid** based on tetrahedral, hexahedral or polyhedral cells:

   Grid elements of unstructured grids are not aligned with the flow direction. The advantage that the mesh can cover even complex geometries and still provide a good solution accuracy. Disadvantages are the higher numerical diffusion throughout the mesh and computer memory requirements to handle the model.

For the presented CFD model, both types of the structured grid are chosen. The first type of the structured grid represents the boundary layer (prism layer) and the second type is used to fill the computational grid with cells. The cells in the overlap of both grids are then trimmed with each other. The decision towards a hexagonal mesh (instead of polyhedral) is based on the turnaround time of meshing and calculating. With the available RAM memory of just 8GB, a polyhedral meshes with nearly 5 million cells could be generated whereas the hexagonal (trimmed cell) mesh provided up to 8 million cells for the half car model simulation and still achieved a shorter turnaround time. The presented final volume mesh and its refinements are the result of numerous meshing and solving iterations.

Surface Meshing

In the first step, the (CAD) model is prepared for the computational grid generation. All input parts are covered by a surface mesh (most common: triangular shaped cells) which is refined around geometry changes and pre-defined areas of interest such as aerodynamic devices and tires [38]. Commercial CFD and grid generation software often includes surface repair and preparation tools such as the surface wrapper toolkit of StarCCM+ which automates the surface mesh generation process. Multiple refinements at important areas like leading and trailing edge or around the tires are implemented in this setp. The surface mesh generation process is split into several groups of parts (front

wing, rear wing, and body including wheels) for an easier handling of interchangeable parts. The meshed surface is then passed over to the volume meshing process where the surface mesh gets adapted to the chosen cell type of the volume mesh. The different steps of the workflow are shown in Figure 28.

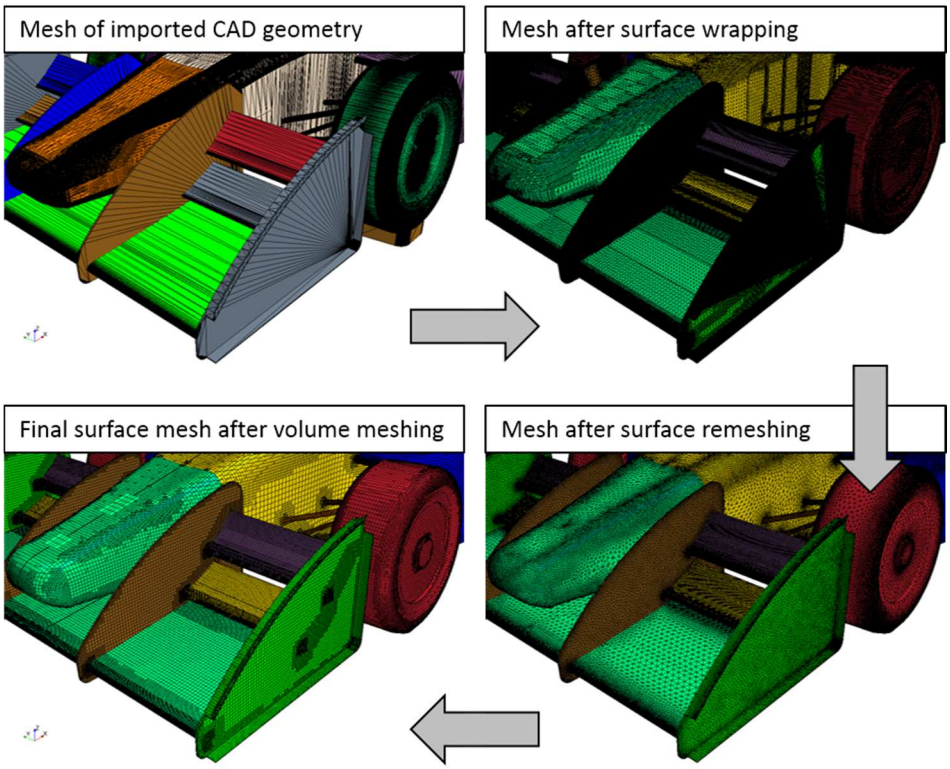

Figure 28: Development of surface meshes

Volume Meshing

The final step generates all volumetric cells in the sub domain where the calculations are carried out. The computational grid is generated within the sub domain according to the user inputs of surface controls, prism layers (boundary layer representation), curve controls, and volumetric controls. The mesh is refined in areas of possible flow separation or steep geometry changes. The present simulation features a large number of refinements which is shown in the Figure 29 to 31 (p.69). Furthermore, a list with all used parameters is attached in Appendix C.

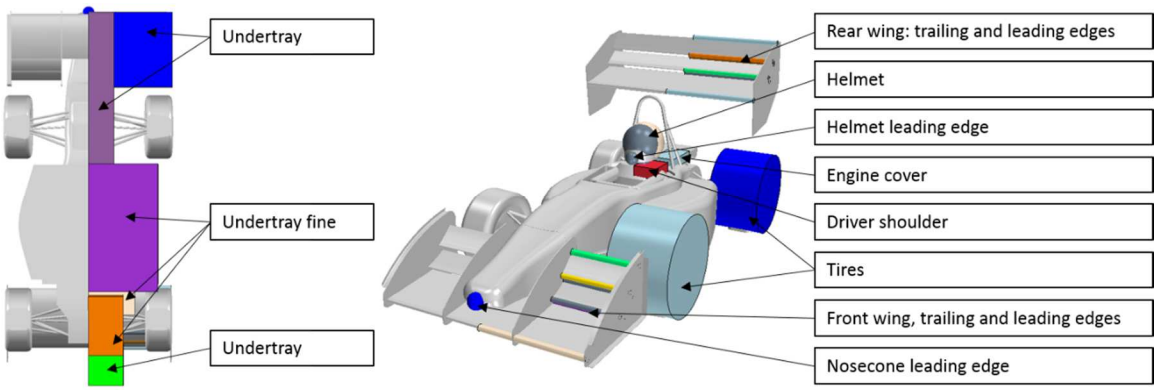

Figure 29: Near body mesh refinements around the car

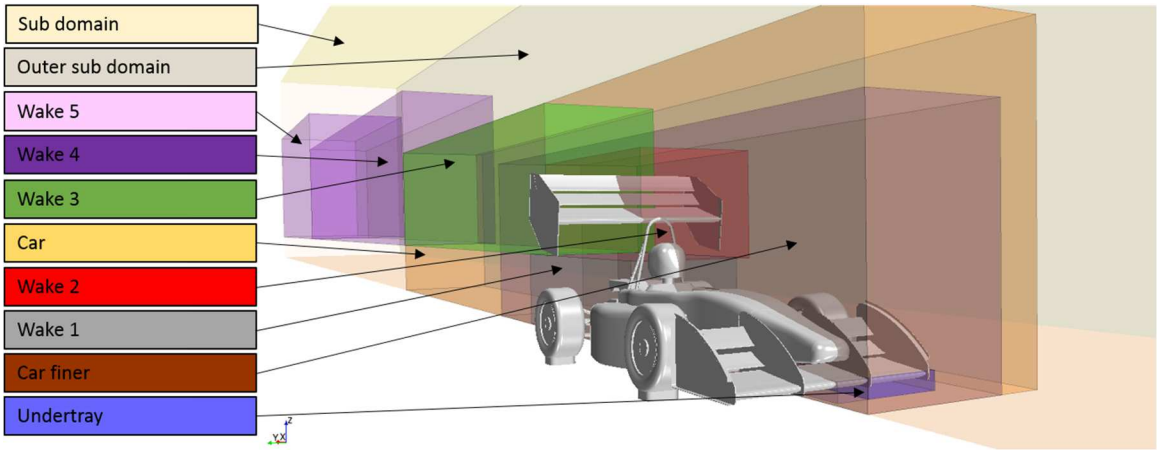

Figure 30: Sub domain mesh refinements around the car

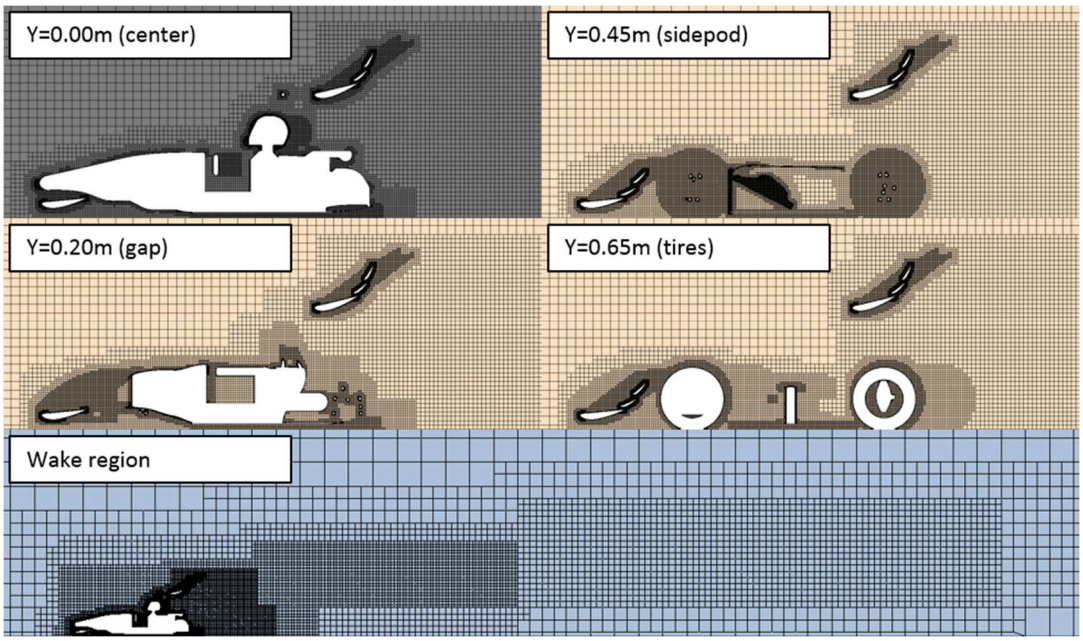

Figure 31: Volume mesh projected on plane sections of fluid sub domain

4.2.1.4. Boundary Conditions & Physical Model

The fluid subdomain box utilizes a velocity inlet boundary, a pressure outlet, a wall boundary at the ground and symmetry boundaries at the far field and in the center of the car (half car simulation). The ground boundary is set to slip condition because it is an open road simulation where no boundary layer gets generated on the ground surface [33]. Moving/ rotating reference wall boundaries are applied to the tires. The tire rotation is calculated by equation (62) and the rotational speed with respect to the vehicle speed is listed in Table 7.

$$n_{13"\,tires} = \frac{v_{translation}}{2\pi\, r_{dyn}} \tag{62}$$

Table 7: Rotational wheel speed (13”) with respect to translational vehicle speed

Vehicle speed [mph]	Vehicle speed [m/s]	Tire rotations [rpm]
20.0	32.0	325.97
25.0	40.0	407.46
30.0	48.0	488.96
35.0	56.0	570.45
40.0	64.0	651.94
45.0	72.0	733.43
50.0	80.0	814.93
55.0	88.0	896.42
60.0	96.0	977.91
65.0	104.0	1059.40
70.0	112.0	1140.90
75.0	120.0	1222.39

Moreover, the following parameters are set as constants:

- Three-dimensional, gas, steady, constant density [38]
- Ambient pressure: $101325.0\ Pa$ [38]
- Density: $1.18415\ kgm^{-3}$ [38]
- Temperature: $298K$ [38]
- Dynamic viscosity: $1.85508e^{-5}\ Pa \cdot s$ [38]
- Reference area: $0.525m^2$
- Turbulent flow utilizing RANS model
- Turbulence model: k-ω coupled with SST (Menter) [33, 38]
- Cell quality remediation: On (bad cell treatment [38])
- Wall function: All y+ wall treatment [38]
- Viscous resistance of porous media (radiator replacement): $226.0kgm^{-3}s^{-1}$ [33]

4.2.2. Solving and Post-Processing

After the entire model is pre-defined and meshed, the solver executes the calculation based on the chosen solver and parameters. An iterative approach tries to balance mass flow and momentum through the sub domain (from inlet to outlet) until a (converged) solution is found [29]. As a representation of the converging process, the solver monitors residuals starting with highly oscillating values that will converge later on. The Residuals represent the degree of satisfaction of essential equilibrium equations of mass, momentum and specific parameters of the turbulence model [38]. As a measurement of convergence, constant residuals indicate that a solution is found. To judge the convergence, monitors of forces and moments are created. When the forces remain

constant (or oscillate around a constant mean value) over a certain period of time, the simulation can be considered as converged. Often, oscillating solutions are a result of poor mesh quality, a large turbulent regions and/ or separation. The present simulation is considered as steady. This simplification is necessary for a time effective simulation process [33].

It is common practice to run an example simulation over a long period of time to evaluate residuals and forces change with an increasing iteration number. The presented baseline model has been run over 5000 iterations. Momentums and continuity reach convergence criteria of around 10e-4. The turbulent kinetic energy, however, remains at a convergence criterion of 10e-2 which is caused by the large turbulent zones in the model. The change of forces is plotted in Figure 32. The residuals start oscillating and forces remain stable after 1250 iterations. Therefore, the iteration limit is set to 1500 and all forces are calculated with the last 250 iterations. The turnaround time of an entire simulation process including meshing and solving is 11.5 hours which fulfills the initial goal of the JMS team.

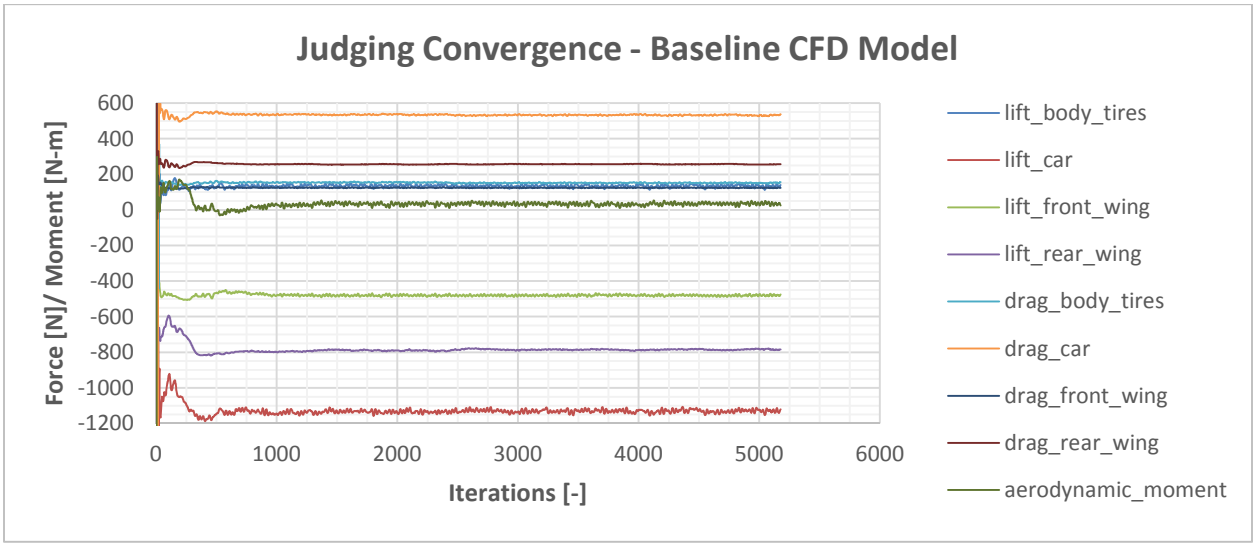

Figure 32: Judging convergence of the JMS14c baseline model CFD simulation

4.3. Results

After setting up the computational grid and the flow physics, the baseline model is evaluated by a comprehensive post-processing analysis. Throughout the analysis, the following figures are used to show and discuss the results:

- Downforce, drag, front-to-rear bias, and lift-to-drag ratio charts
- Surface pressure charts and scalars
- Volumetric scalar plots of a negative total pressure coefficient

The first part covers the CFD model analysis including sensitivity studies of varying inlet velocities, ride heights, and pitch angles. The second part of this section compares the previously analyzed data of on-track tests with the simulation results to draw conclusions about the accordance of both data sets. Throughout the analysis, dimensionless coefficients are used for the evaluation of data. For demonstration purposes, the half car model is mirrored and presented as a full car.

4.3.1. Mesh Verification

This section presents the baseline model and a complete analysis of the flow scheme. The model features the default parameters of ride height (48mm), zero roll or pitch angle, and the rear wings in an aggressive setup of 16deg AoA. It is expected that the flow scheme changes over the velocity which is why three different velocities are analyzed for the mesh verification. The inlet velocity is: (a) 15.6m/s (35mph) as the average track speed, (b) 22.4m/s (50mph) as a representation of high-speed sections, and (c) 33.5m/s (75mph) as the top speed. The flow scheme is analyzed with respect to:

- Near wall treatment (wall y+)

- General flow scheme around wings, the model and within the wake region
- Highly turbulent areas (around tires, wing endplates, driver)
- Surface pressure coefficient
- Negative total pressure coefficient
- Flow velocity

Near wall treatment

An accurate near wall representation is important for the prediction of forces and to meet the requirements of the chosen turbulence model. Figure 33 (p.75) shows that the wall y+ requirement is fulfilled and 99.9% of all surface cells are within the range of wall y+ values lower than 5. Incorrect near wall treatments are only found in irrelevant areas such as the connection of all a-arms at the upright or at the jacking tube located at the backside of the engine. The reason is that the sublayer mesher could not fit enough cells of the prism layer representation in this area so that the overall prism layer cell count is reduced. This causes a steep velocity gradient within the prism layer mesh and therefore, too high wall y+ values. The main planes, the driver's helmet, and the tires show the highest wall y+ numbers due to the high flow velocity and significant pressure changes within a small area. Generally, the wall y+ numbers increase with higher inlet velocities.

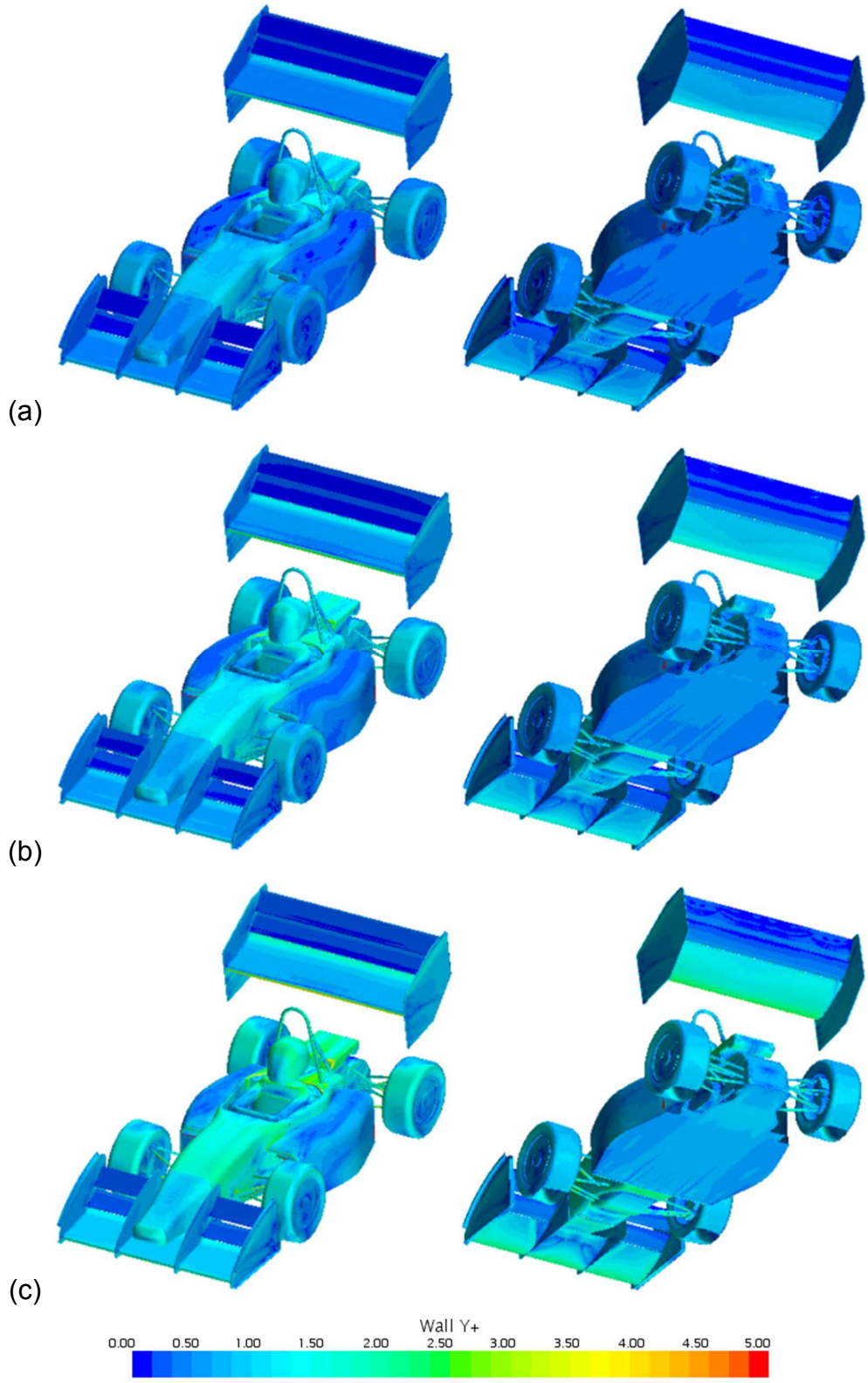

Figure 33: Wall y+ at (a) 15.6m/s, (b) 22.4m/s, and (c) 33.5m/s

General flow scheme, wake and turbulent areas

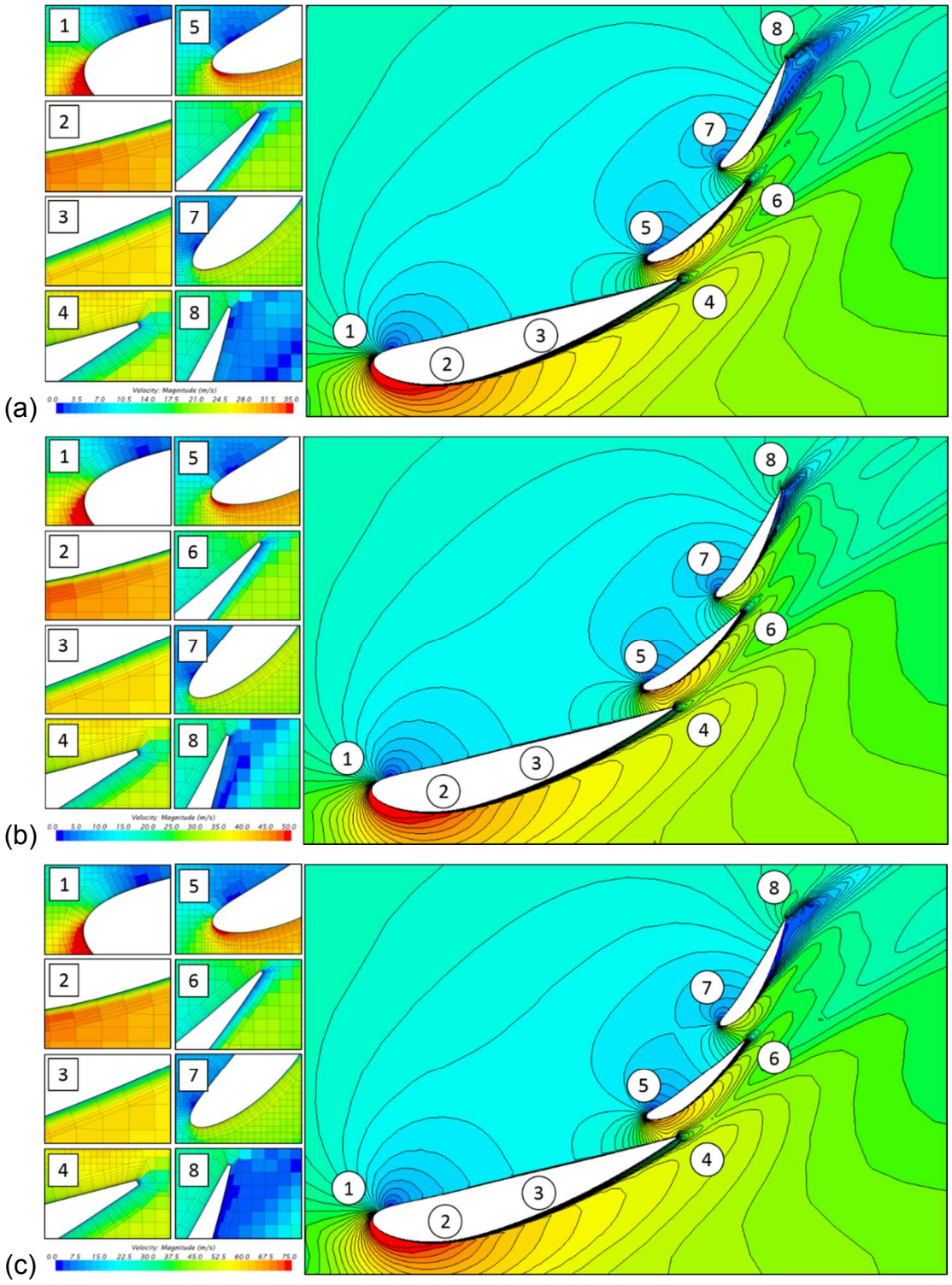

Figure 34: Velocity plot and boundary layer comparison of rear wing at the center location (Y=0.0m) at (a) 15.6m/s, (b) 22.4m/s, and (c) 33.5m/s

In Figure 34 (p.76), the velocity profile around the wings is represented by a color scheme. The growth of the boundary layer and the point of separation at the second flap are clearly identifiable. In this particular example, the separation at the second flap shows that the wing is operated close to its maximum downforce generation [9]. The flow scheme around the wings shows just a small difference between the three velocities. However, the flow separation at the second flap starts much earlier in case (a) and (c). This results in a smaller downforce coefficient as it is apparent in Figure 40 (p.84).

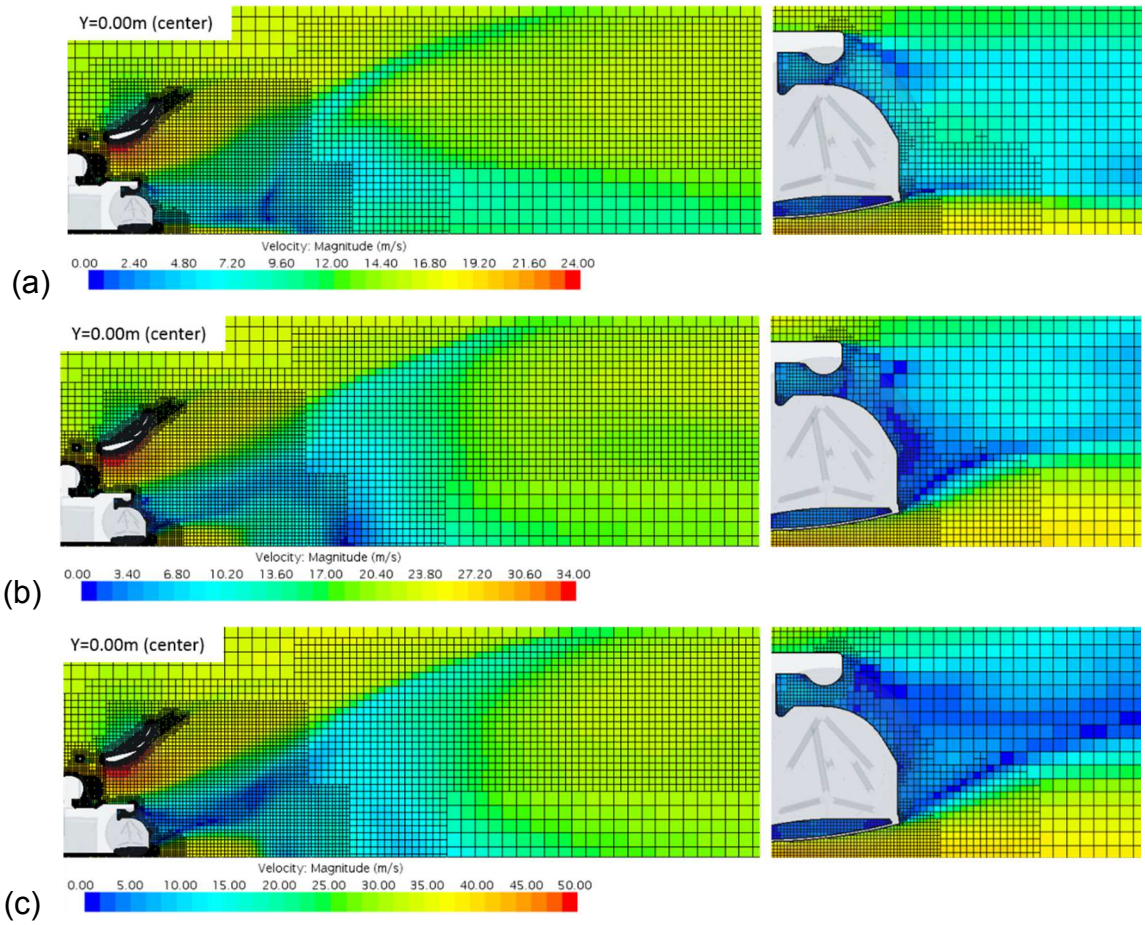

Figure 35: Wake zone refinements at (a) 15.6m/s, (b) 22.4m/s, and (c) 33.5m/s

The wake zone refinements are shown in Figure 35. The wake representation is a compromise due of the limited overall number of cells. With respect to the available computational power, it is decided to rather focus on a fine mesh close to the body than a

fine mesh in the wake zone. The overall cell number is reduced by refining wake zones only where significant pressure and velocity changes happen.

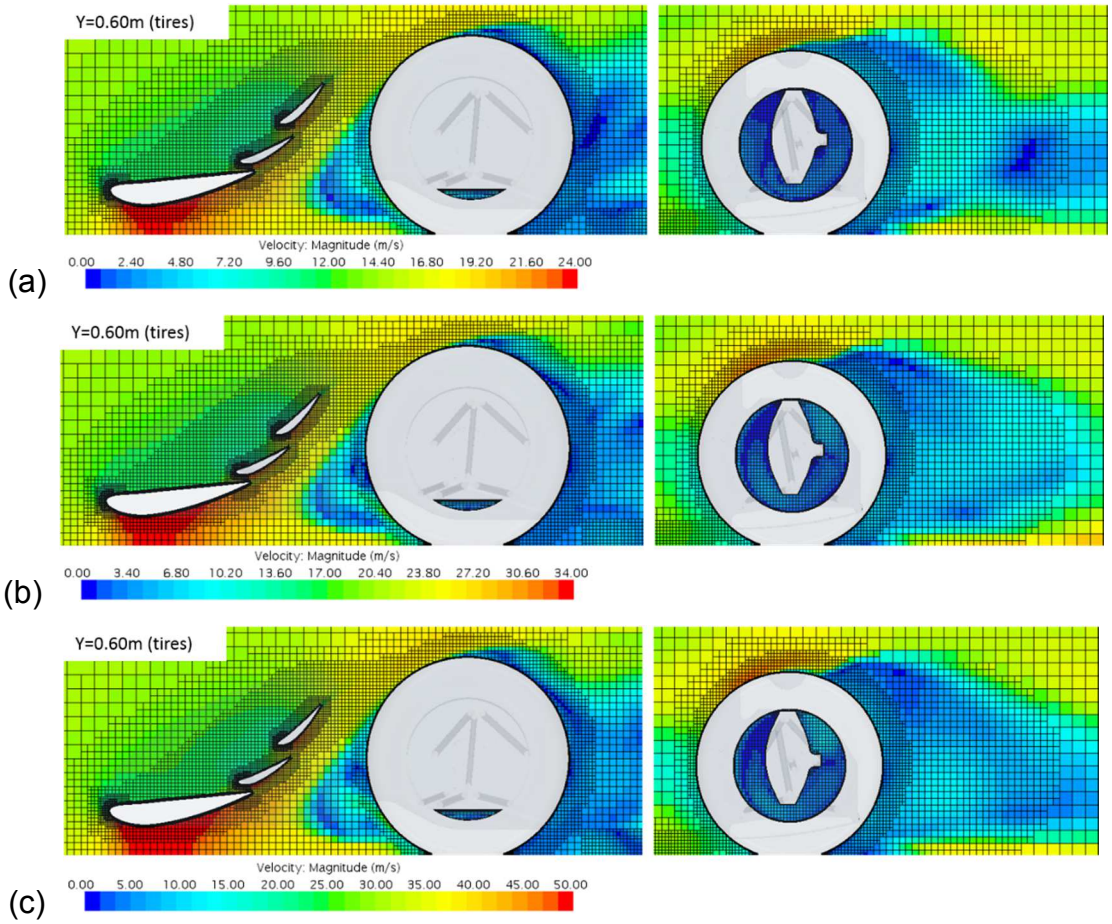

Figure 36: Turbulent zone refinements at (a) 15.6m/s, (b) 22.4m/s, and (c) 33.5m/s

Other selected areas of highly turbulent flow are presented in Figure 36. Special attention is given to the rotating tires since a highly disturbed flow field is expected. Although the refinements cover the important areas close to the tire and in the tire wake, the mesh is still too coarse. Ideally, the fine mesh should be much larger to capture the entire wake flow and the area between the front wing and the front tire. But, this would increase the cell number drastically. The particular examples show that the flow field is similar over the given velocity range. But, the wake zone increases its length downstream with higher flow velocity.

Surface pressure coefficients and iso-surfaces of total pressure coefficients

Figure 37 (p.80) gives an overview of the pressure distribution on the surfaces of the car. It is used to identify areas of separation (abrupt pressure change, for instance at the second flap of the rear wing), high-pressure zones (orange-red) and the distribution at specific parts such as the undertray. In the particular examples, only small differences between (a), (b), and (c) are noticed. For instance, the distribution of the average speed of case (a) shows a lower respective pressure coefficient towards the rear end of the undertray. This indicates a lower lift generation of the undertray/ diffuser than in the high-speed (b) and top-speed (c) cases. This behavior is evident in the body lift coefficient chart of Figure 40 (p.84). Furthermore, a slightly lower pressure on the front wing underside is noticeable. However, the influence through the mid plate increases with higher velocity as there is a larger area of higher pressure around the mid plate at the underside. The rear wing pressure coefficient only changes at the backside of the second flap. The chaotic pressure transition at the backside is an indicator of flow separation which was already shown in Figure 34 (p.76).

In Figure 38 (p.81), an iso-surface of negative total pressure coefficient is shown. Generally, this representation highlights areas that are responsible for “energy losses” and the main portion of drag (wake region). The lower the total pressure coefficient, the higher the energy loss is. Furthermore, vortices can be clearly identified. The presented figure only colors the iso-surface in the strength of the turbulent kinetic energy. At the inside of this generated volume, the total pressure coefficient is negative. The total pressure coefficient is minimized in the wake zones behind the tires and engine as well as within the vortices generated by the wings.

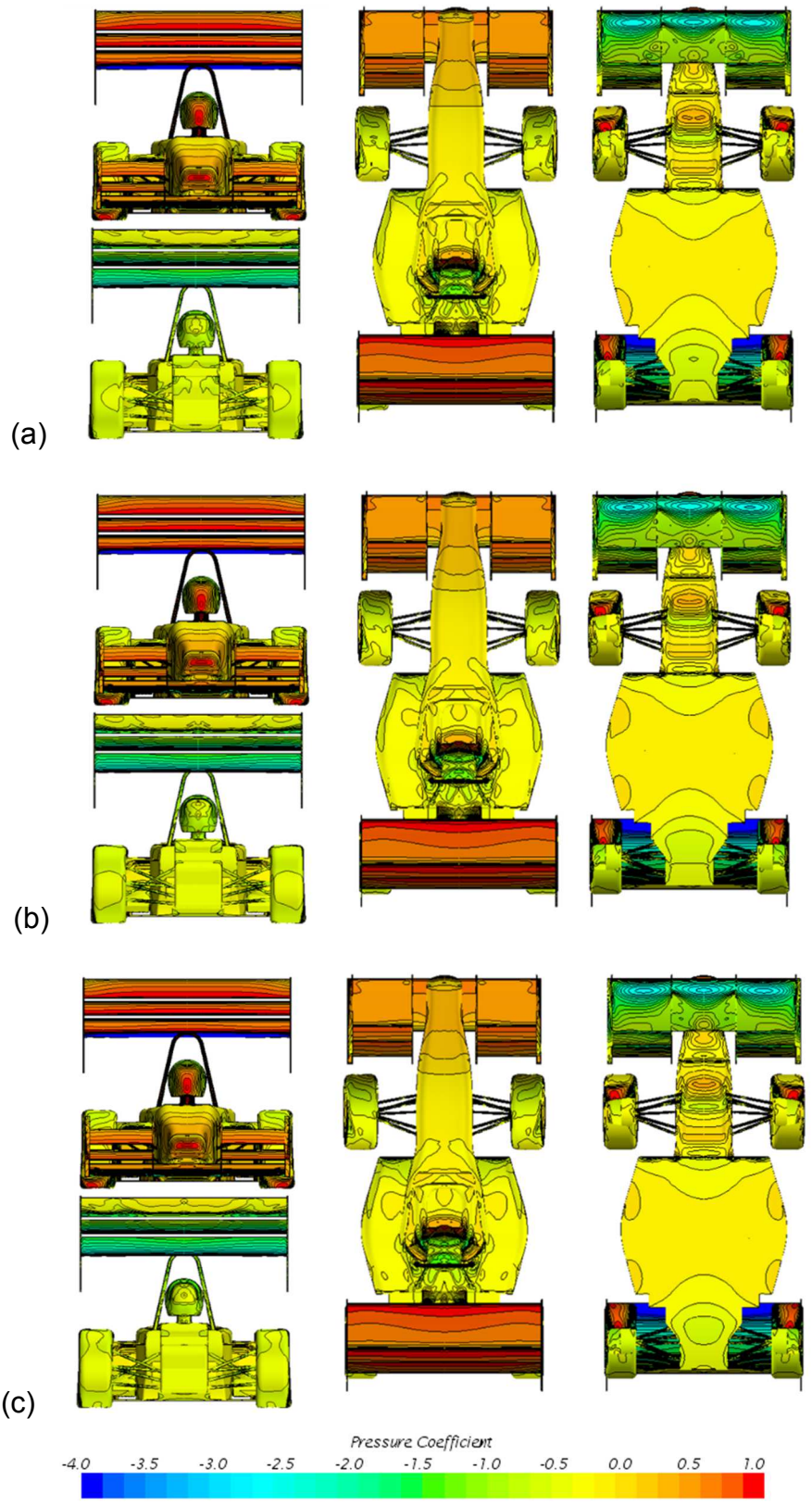

Figure 37: Surface pressure coefficient plots at (a) 15.6m/s, (b) 22.4m/s, and (c) 33.5m/s

In the particular examples, the shape of the wake zone is different at all three inlet velocities. The size and path of the generated vortices at front and rear wing seems to be identical at all covered flow inlet velocities. Furthermore, the size of the front tire wake seems to get smaller and more stretched toward the outside of the sidepod with higher velocity.

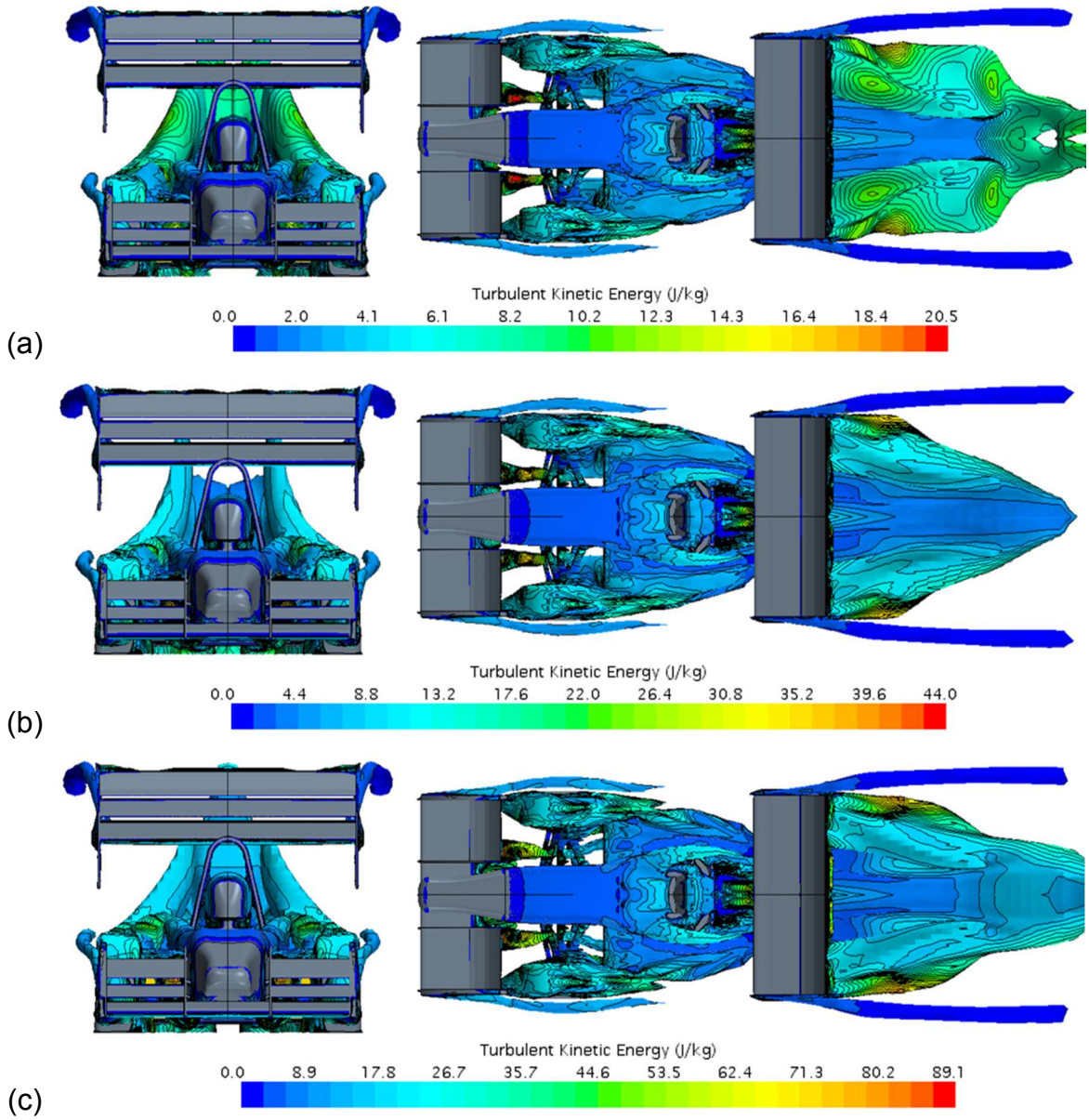

Figure 38: Generated volume with negative total pressure coefficient at (a) 15.6m/s, (b) 22.4m/s, and (c) 33.5m/s

Flow velocity

For a better understanding of the flow properties, several plane sections highlight the flow scheme within the model. Figure 39 displays the flow velocity distribution. The wake generation through the car in the center section as well as behind the tires is distinctive. To ensure comparability, all velocity charts are scaled to a 50% higher velocity than the respective inlet velocity. The large red zones represent high-speed flow. The larger the red zone below the wing, the higher the suction pressure is. Therefore, the pressure gradient between upper and lower side of the wing increases with a larger suction zone.

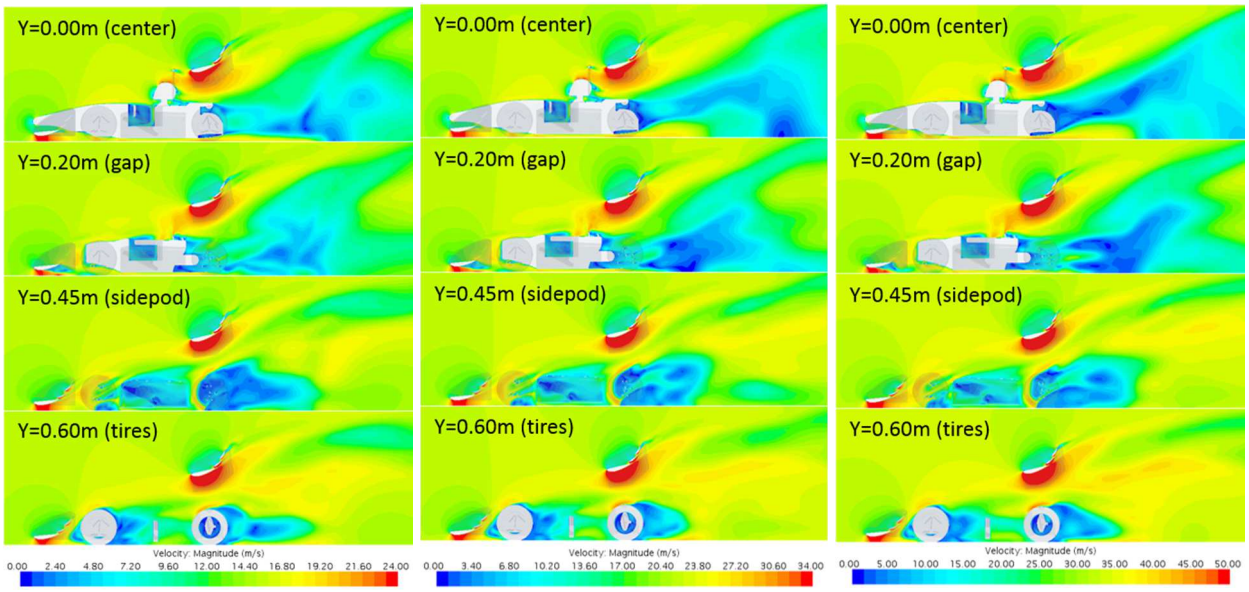

Figure 39: Baseline model - velocity distribution plots along the Y-axis of the car at (a - left) 15.6m/s, (b - middle) 22.4m/s, and (c - right) 33.5m/s

To sum up, the individual prism layers setups of each part are chosen according to the needed accuracy and the available computational power (see Appendix C). It is found that the model represents the boundary layer accurately enough. Furthermore, the wake and highly turbulent zone representations are reasonable enough to stay within the cell number limitation of roughly 8 million cells. The presented model is used as the baseline

for all further sensitivity studies. The model can be easily adjusted with respect to pitch angles, ride heights, velocities, and wing setups due to the implementation of CAD parameters and automated macros. More macros have also been created for the automatic plot generation. Plot and numbers of the aerodynamic coefficients of the baseline model can be seen in the following section.

4.3.2. Velocity Sensitivity

Inlet velocity speeds listed in Table 7 (p.70) are simulated in CFD to analyze the aerodynamic behavior over a wide range of velocities (based on the FSAE track analysis in chapter 2.3). The charts in Figure 40 (p.84) indicate that the downforce and drag generation stays stable above the inlet velocity of 13.4m/s (30mph). At lower speed, the coefficient of downforce drops because the flow is not attached to the rear wing (compare velocity profiles in Appendix D). The rear wing reattaches the flow around 11.1m/s (25mph). Although the overall downforce generation stays almost constant over the speed range, the aerodynamic balance migrates from a rearward to a neutral position in the center of the car (ahead of CoG at 0.46 font bias). The surface pressure coefficients plotted in Figure 41 (p.85) indicate that negative pressure of the front wing increases by 40% over the speed range. This results in a 25% higher front wing downforce coefficient over the speed range. The negative pressure coefficient of the rear wing remains constant after the flow got attached. There is no change in the downforce coefficient at higher speeds. The overall downforce, however, does not increase because there is an increase in lift of the body/ tires at higher speeds.

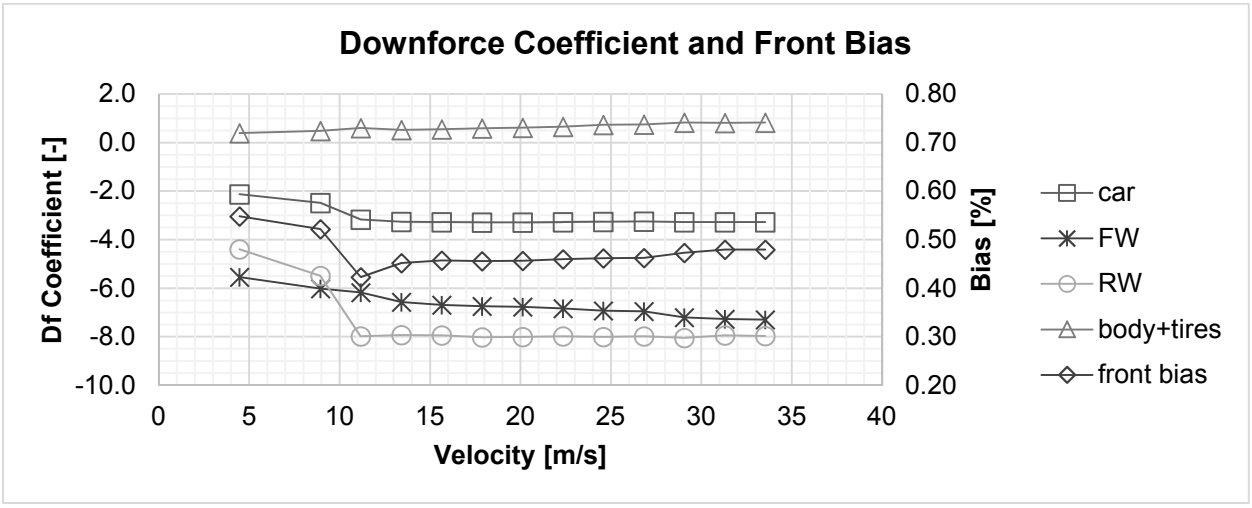

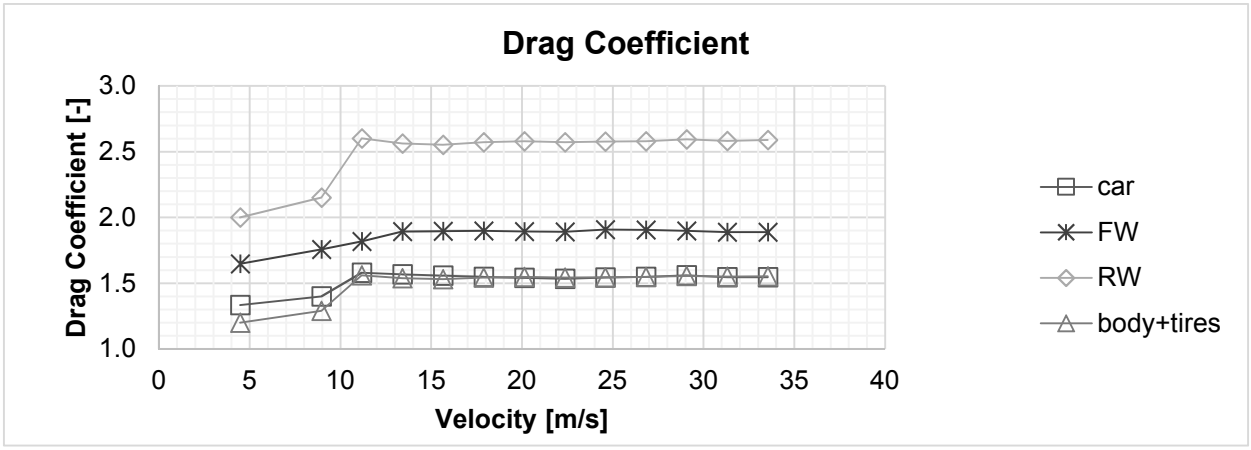

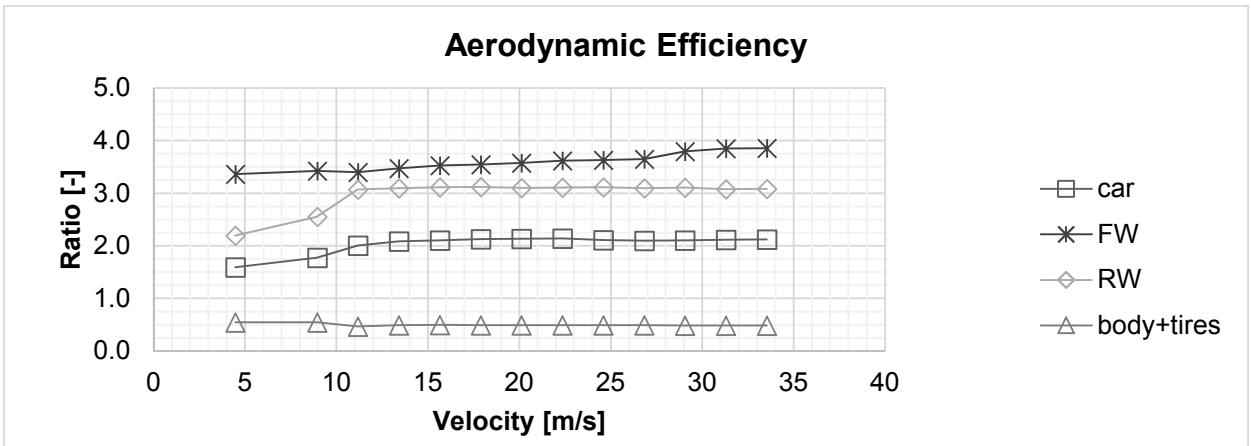

Figure 40: Aerodynamic coefficients of baseline model over the velocity range

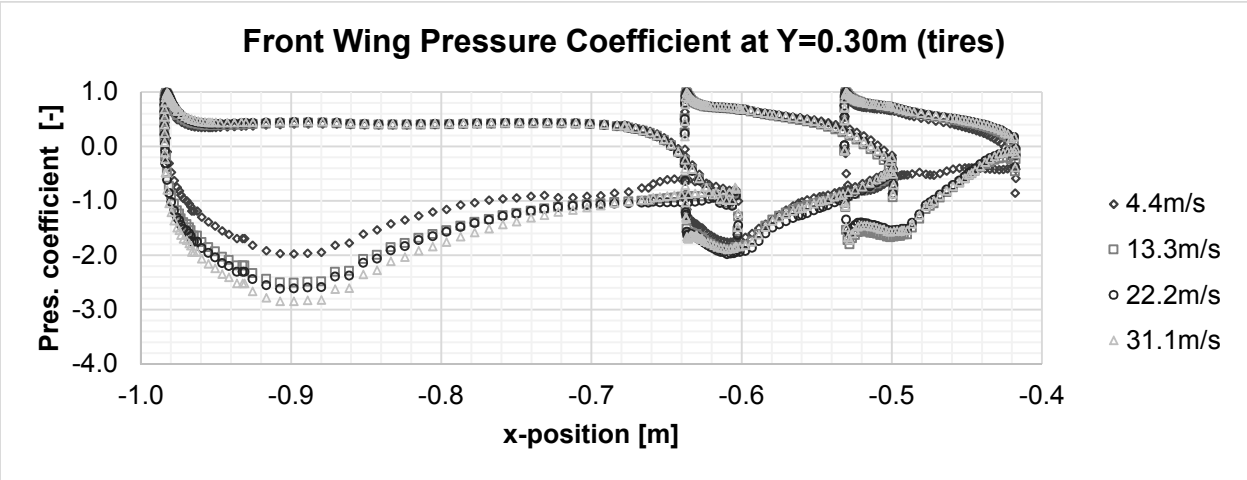

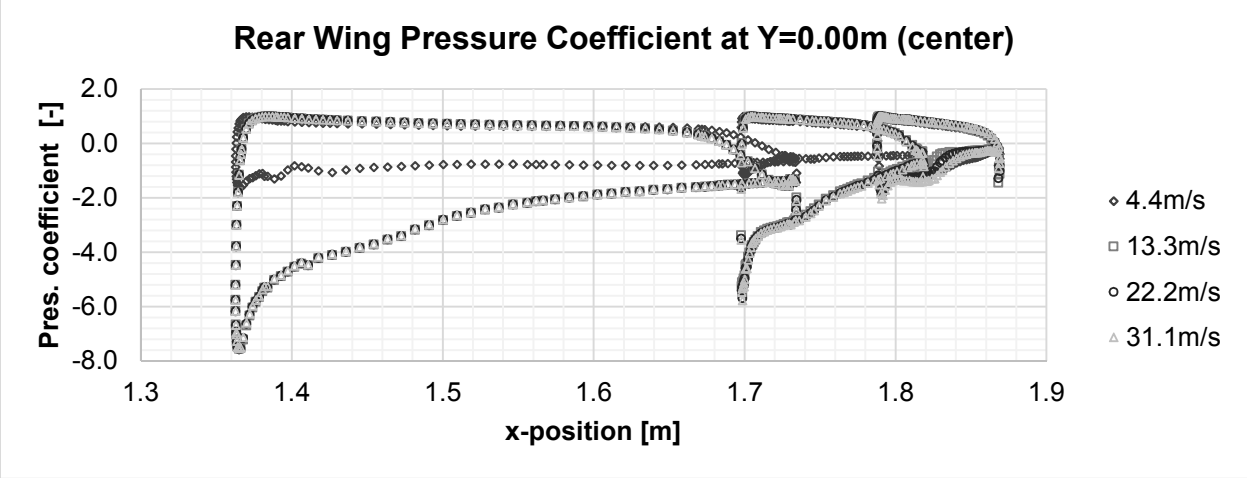

Figure 41: Pressure coefficients of front and rear wing – velocity sensitivity

4.3.3. Ride Height Sensitivity

The ride height sensitivity is initially analyzed at the fastest inlet velocity of 33.5m/s (75mph). Varied in 5mm steps, the lowest ride height is set to 28mm, the highest is set to 53mm respectively. The baseline setup of 48mm is the considerably high for FSAE race cars. However, the ride height is chosen to protect the car from bumps and scraping the front wing under braking/ pitching on the test tack.

Changes in in the downforce level are expected due to an increase in ground effect at the front wing. Figure 42 (p.86) shows a decrease in front wing downforce at lower ride heights. It seems that lower ride heights prevent the flow of passing through the gap

between wing and ground. All other coefficients experience just small changes over the speed range.

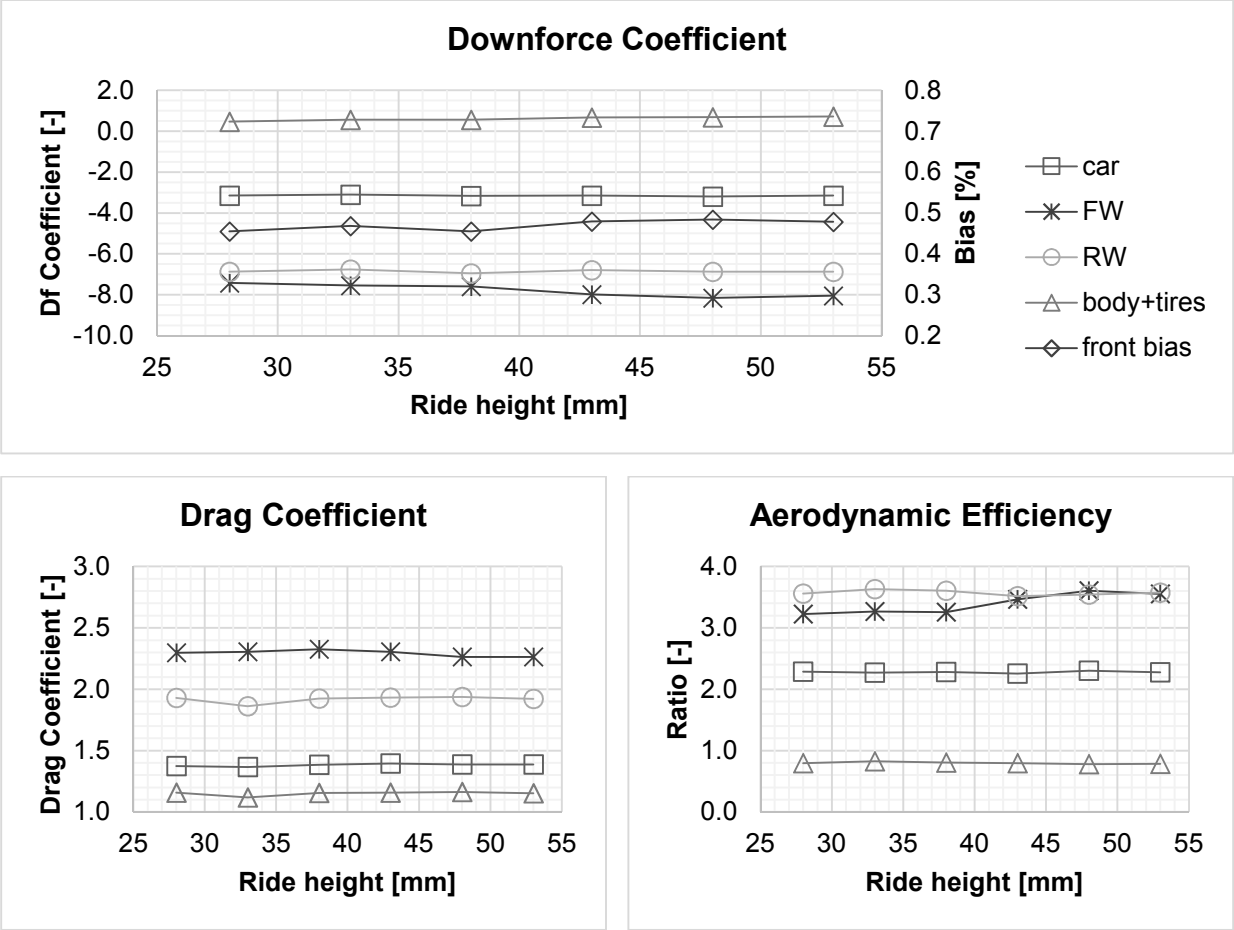

Figure 42: Aerodynamic coefficients of baseline model at various ride heights at 33.5m/s

In Figure 43 (p.87), surface pressure coefficient plots are shown to verify the reduced downforce of the front wing. There is a change in negative pressure at the main plane by 12% in the center section and 9% in front of the tires (from 28mm to 48mm). The reduced pressure field is apparent from the leading edge to the center of the wing. Furthermore, a small drop in pressure occurs at the trailing edge in the lateral center of the car. The flaps, however, experience slight differences at the leading edge. All of the reduced pressure results in a smaller downforce of 9% (28mm to 48mm).

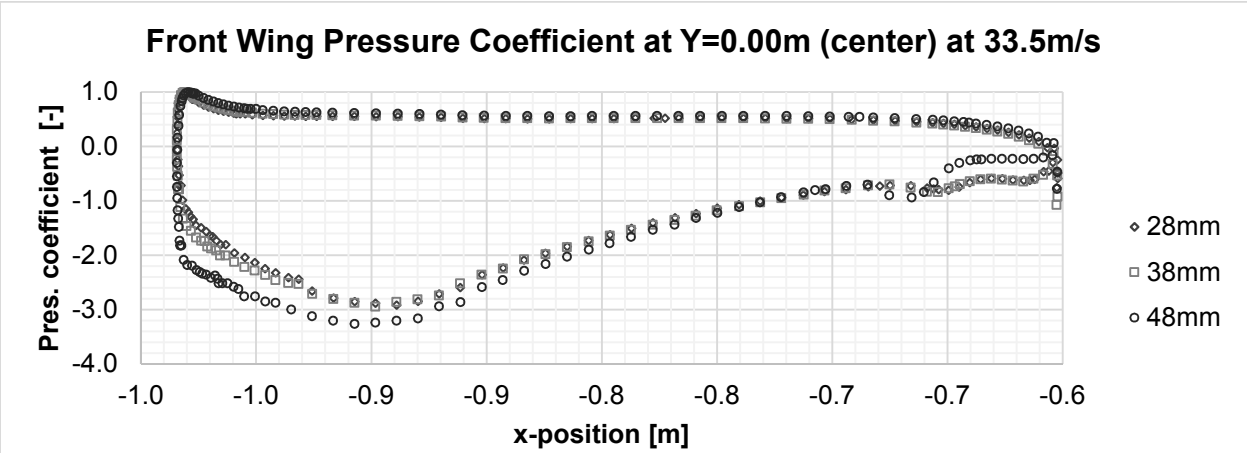

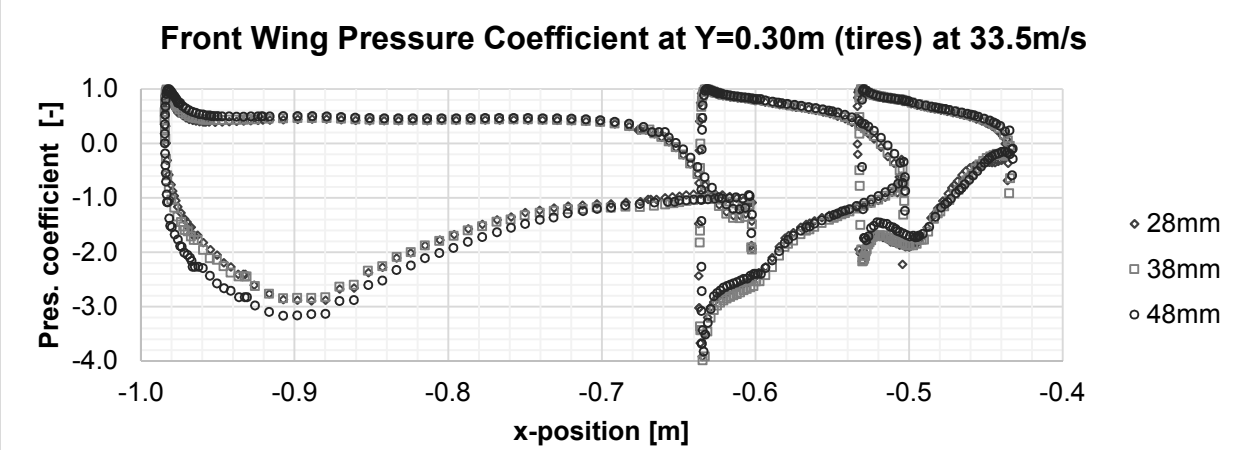

Figure 43: Pressure plot of front wing main plane at various ride heights

To study the influences of different ride heights over the entire speed range, multiple iterations have been run. Normalized plots are created for all setups to endure comparability. Sensitivities of the front and rear wing are given in Figure 44 (p.88). All contour plots are normalized with respect to the baseline model of 48mm ride height. Green coloring indicates an improvement, yellow to red represents a deterioration of the respective coefficients.

The front wing downforce output of lower ride height setups is up to 7% lower than the one of the baseline model. The higher the inlet velocity, the greater the difference between

the ride heights of the front wing downforce is. The rear wing, however, does not vary significantly and shows a maximum change of ±3% with respect to the baseline model.

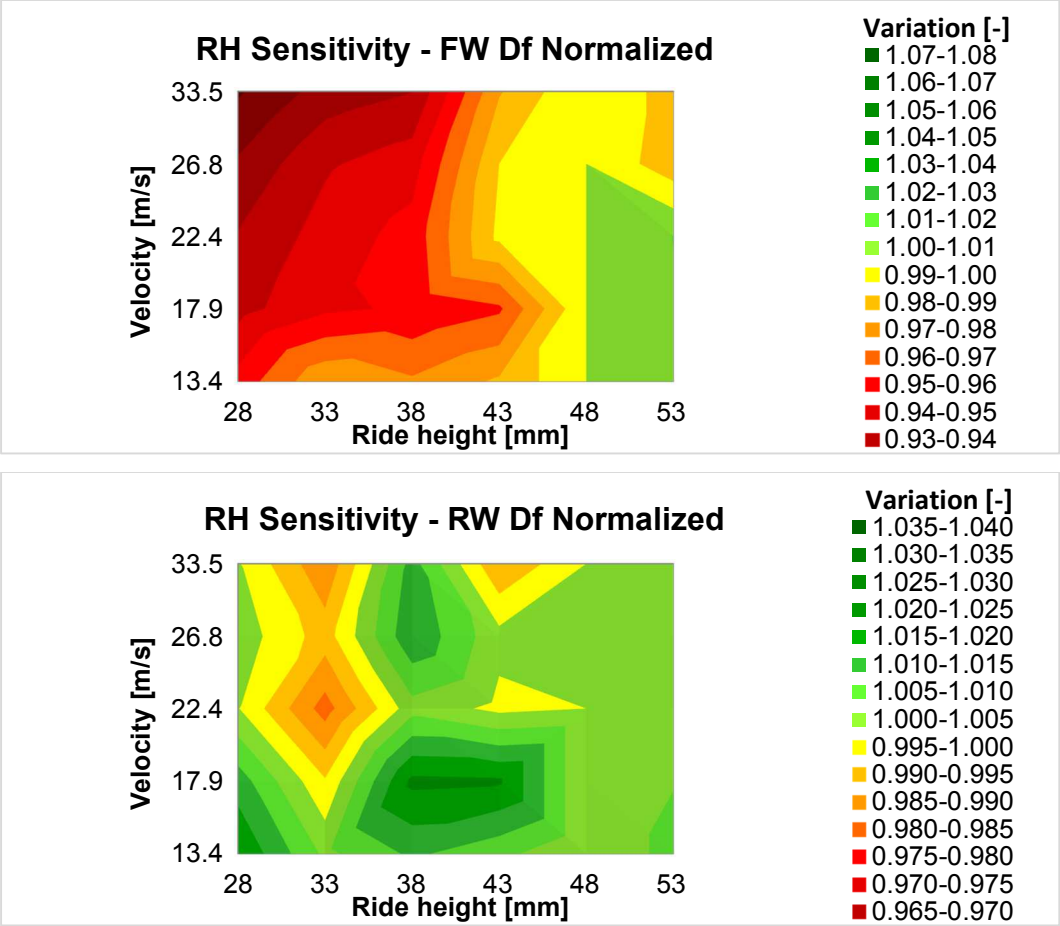

Figure 44: Ride height sensitivity – downforce of front wing, rear wing, body

Figure 45 (p.89) displays downforce, drag, and lift-to-drag data for the entire model. All coefficients do not change drastically but reveal that lower ride heights are not beneficial for the downforce generation. It is concluded from the data that the 48mm ride height setup is a reasonable choice for the initial setup. Considering a 5 to 10mm ride height reduction under high aerodynamic load, then the chosen 48mm baseline setup is the best compromise for downforce generation.

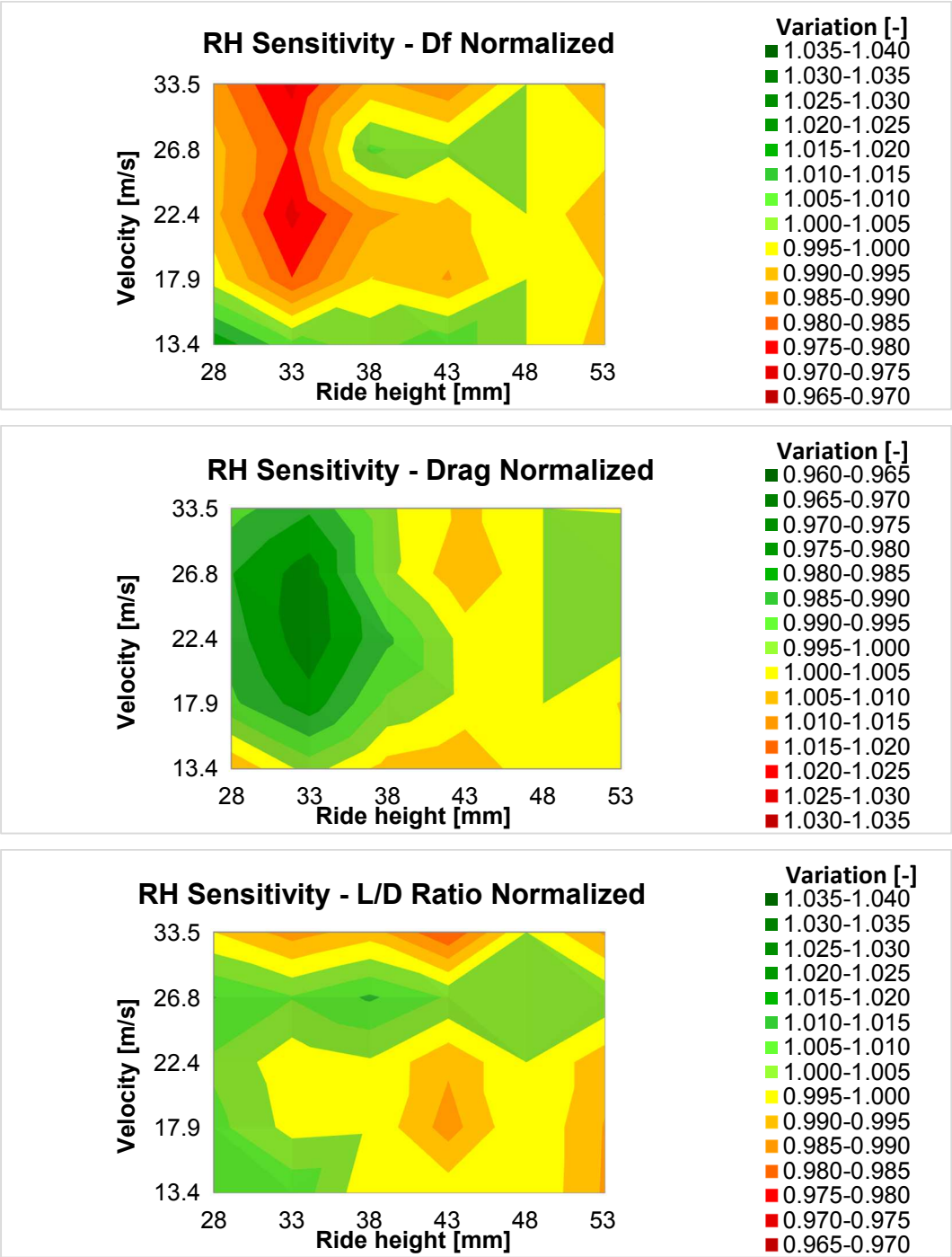

Figure 45: Ride height sensitivity – downforce, drag, aerodynamic efficiency

Finally, the aerodynamic bias of the ride height sensitivity study is plotted in Figure 49 (p.93). The chart shows the actual balance where the number represents the load on the front axle. Hence, 0.5 is the middle position between both axles. To achieve a stable setup

for high-speed, the CoP should be located slightly behind the CoG. From it is known that the CoG is located at 0.47 front and 0.53 rear. Hence, the desired CoP location should be at 0.47 front or below in high-speed. From the chart it can be concluded that the CoP location changes within 3% but remains behind the CoG position at all time.

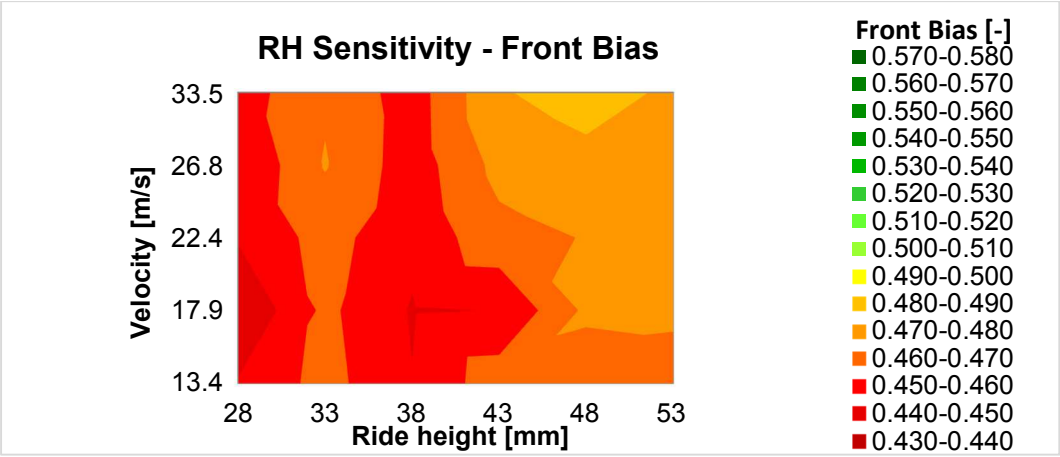

Figure 46: Pitch angle sensitivity of the aerodynamic balance

4.3.4. Pitch Angle Sensitivity

The pitching motion changes the position of the car relative to the ground. The pitch angle between the angled and the default position (0deg) of the vehicle directly influences the angle of attack of the wings (when mounted sprung to the chassis). Furthermore, the ground clearance of the aerodynamic devices changes which might imply ground effects.

A detailed study on the CFD baseline model of the JMS14c is performed at different inlet velocities and pitch angles. The simulated pitch angles are concluded from the recorded real track data. Angles range from -0.80deg to +0.40deg and are realized in 0.2deg steps in the simulation. All following charts are normalized to the appropriate velocity at zero pitch angle and 48mm ride height.

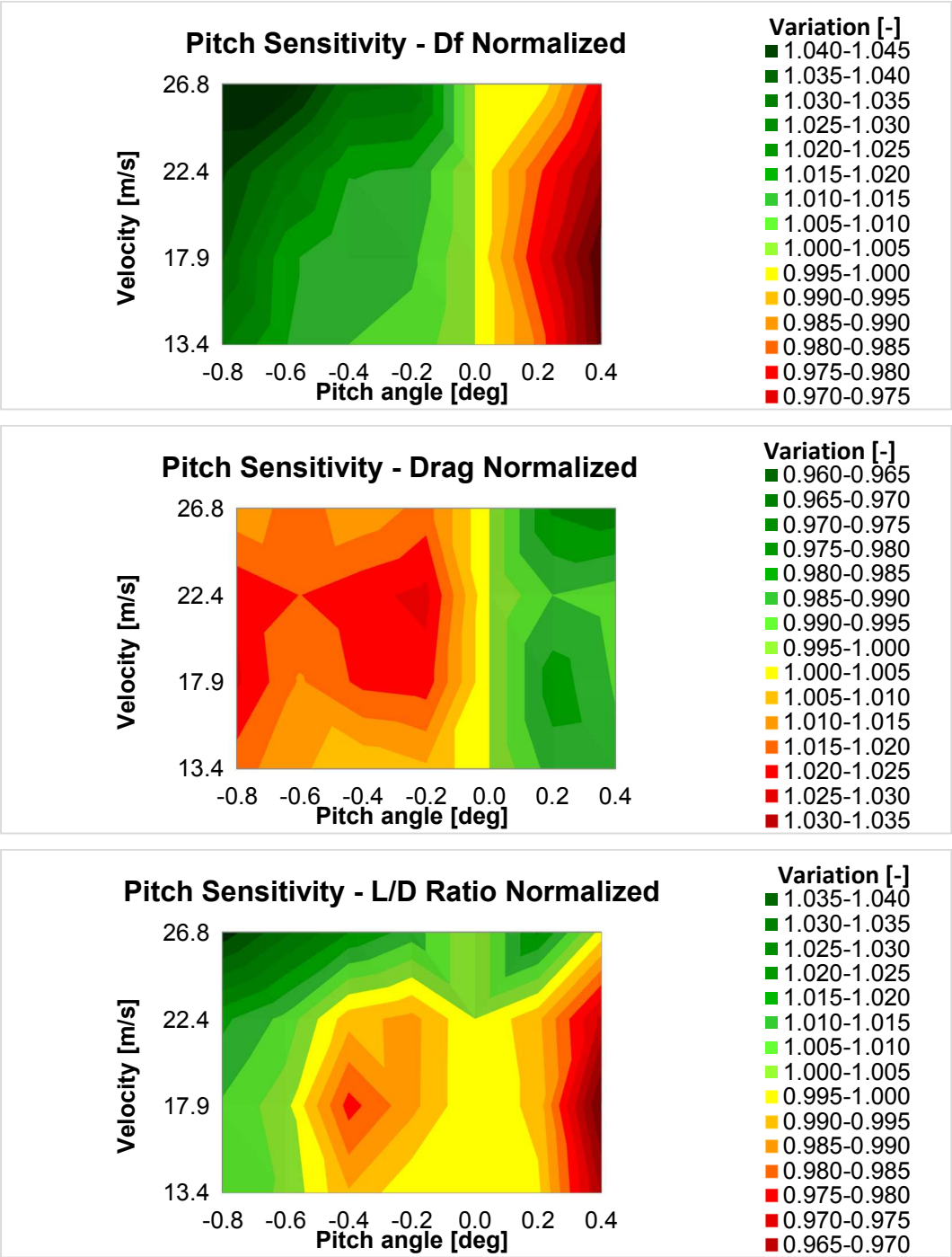

Figure 47: Pitch angle sensitivity - downforce, drag and aerodynamic efficiency

The plots of Figure 47 show the expected behavior of downforce and drag data. At negative pitch angle (braking), the car generates more downforce which causes a higher

drag generation. The higher the speed, the greater the change in downforce is. With positive pitch angles (acceleration), the downforce and drag decrease.

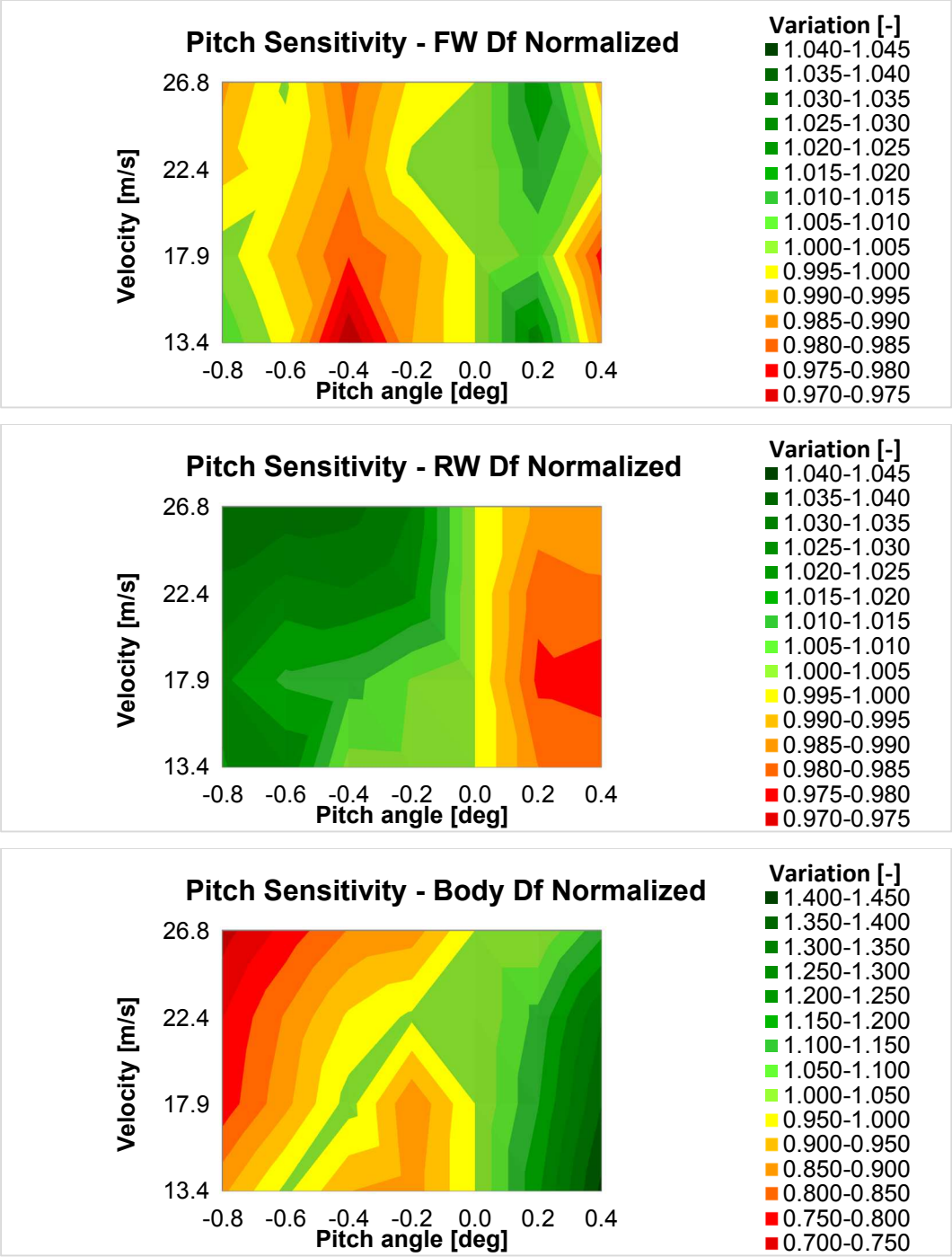

Figure 48: Pitch angle sensitivity - downforce generation of front wing, rear wing, body

A closer look to the distribution and change of downforce in Figure 48 (p.92) shows that the front wing downforce slightly decreases with higher pitch angles. Contrary to the initial expectations of the baseline model analysis, the front wing downforce does not benefit from a higher angle of attack (decrease of 1-3%). The gap between the front wing and the ground is decreased through the pitch angle which implies the same behavior seen in the previous section of the ride height iterations. However, the rear wing clearly benefits from a higher angle of attack and generates more downforce (up to 4%). The high downforce output of the rear wing and the decreased lift of the body/ tires benefit the overall downforce of the car. At top speed and under braking (-0.80deg pitch angle), the downforce is about 5% higher than at the baseline model at zero pitch angle. The aerodynamic balance experiences a slight shift forward in higher speed by 1-2% (see Figure 49).

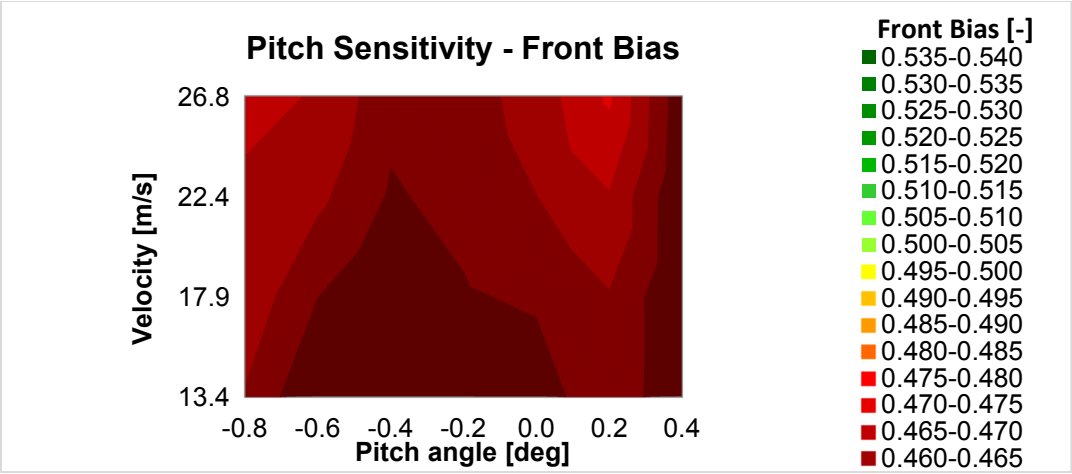

Figure 49: Pitch angle sensitivity of the aerodynamic balance

It can be concluded that the front wing is very sensitive to changes in the pitch angle whereas the rear wing downforce increases with lower pitch angles. The overall downforce and drag shows the expected behavior.

4.3.5. Future Work

The development of the CFD simulation used in this thesis showed that special attention is required in the meshing process. For future work, a more comprehensive mesh comparison of structured, unstructured, and hybrid meshes should be carried out to clearly evaluate the differences in performance, accuracy, and turnaround time of each mesh type.

Furthermore, focus should be put on yaw simulations. Due to the FSAE track layout, the car spends much more time in corners than on straights. Also, downforce is more beneficial in cornering than on straights. Laterally, the force production can significantly be improved by aerodynamic devices whereas the benefit on straights (longitudinally) is reduced to corner exits and in braking zones. Yaw-CFD simulations require much higher computational power. Using the developed mesh of this thesis and applying it to a full car model required at least 16GB of RAM in test runs. The overall cell number was twice as high due to the doubled size of the fluid sub domain. The turnaround time was more than doubled (26hrs for meshing and 1500 iterations) which does not fulfill the requirement of the team anymore. However, understanding the air flow's behavior in yaw would greatly improve the design of aerodynamic devices. The yawing simulation work could be combined with a set of skid pad tests as it was already performed by the author [39].

4.4. Comparison of Simulation and On-Track Results

This section is about the comparison of the simulated and measured data. The baseline CFD model and the real track data sets have been discussed in the previous chapters. Because of the limitation due to the half car model (straight line simulations), only driving situations without any lateral movement can be used for the comparison.

4.4.1. Coast-Down Test

In this section, the coast-down CFD simulation is presented. Recorded real track ride heights, pitch angles and front wing ground clearances from Figure 21 (p.48) are averaged over all runs of each setup. Afterwards, the numbers are imported to adjust the parameter-based CFD model. The individual setup cases are shown in Table 8. For the sake of simplicity, constant pitch angles are assumed for all different setups but the low-drag setup. A different set of pitch angles is imported to accurately represent the low-drag case.

Table 8: Simulation cases of coast-down CFD simulation

Test	#	Velocity [mph]	RH [mm]	Pitch [deg]	RW AoA [deg]	Pitch [deg]	RW AoA [deg]
June 2014 Coast-down	1	30	48	0.62	8.0, 9.0, 10.5, 12.0	0.58	Low drag
	2	40	48	0.57	8.0, 9.0, 10.5, 12.0	0.51	Low drag
	3	50	48	0.54	8.0, 9.0, 10.5, 12.0	0.43	Low drag
	4	60	48	0.48	8.0, 9.0, 10.5, 12.0	0.31	Low drag
	5	70	48	0.4	8.0, 9.0, 10.5, 12.0	0.20	Low drag

All coast-down CFD results are plotted in Figure 50 (p.97). The downforce rises with higher speeds in all setups which is similar to the previous studies. Over the velocity range, the main increase in downforce is caused by the front wing (9%). The rear wing

downforce increases by 5%. Also, the front wing downforce is not influenced by the rear wing setups since there is no significant variation between the setups. Hence, the downforce increase between the setups is only caused by the rear wing. The increase in rear wing downforce over velocity remains similar.

The front-to-rear bias migrates forward with higher speed in all setups. However, the higher the rear wing AoA, the less the CoP forward migration is. The difference in rear wing downforce of different setups also affects the CoP. The difference of the balance between 8deg and 12deg AoA is 3% in low-speed and 4% in high-speed respectively.

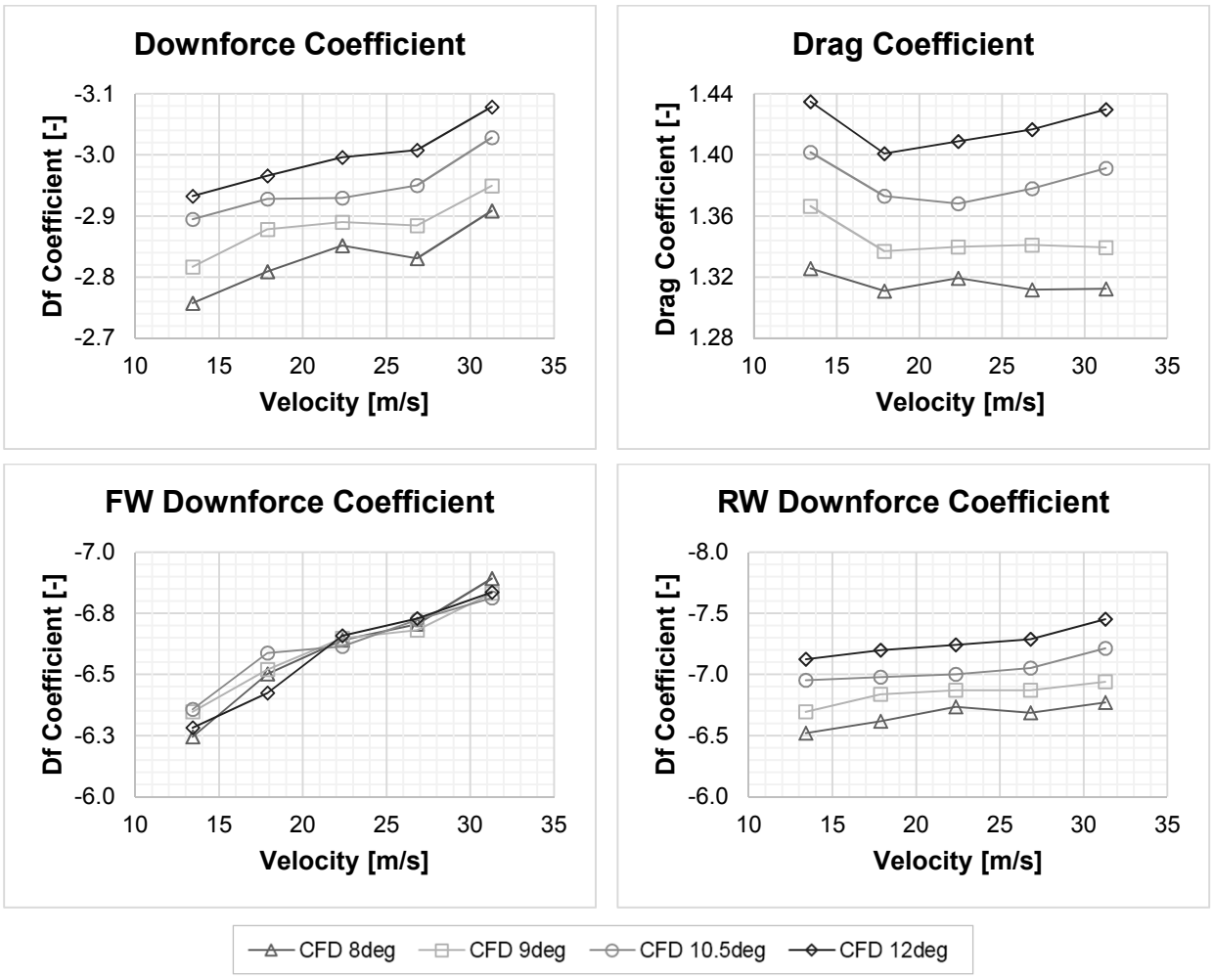

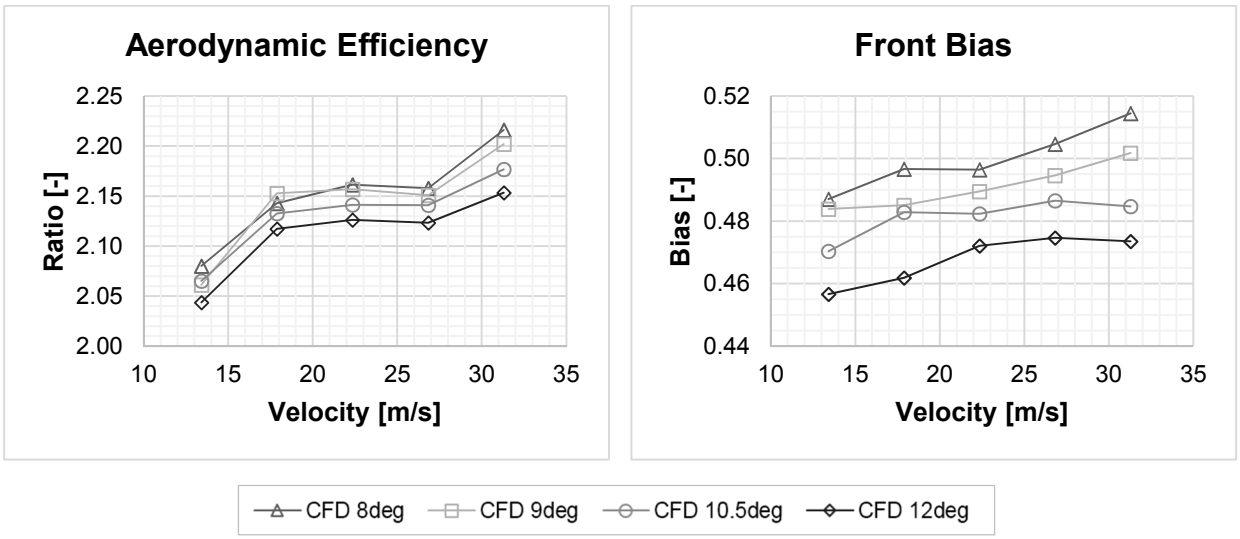

Figure 50: Results of coast-down CFD analysis

Simulation vs. On-Track Results

Table 9 (p.98) shows a comparison of downforce and drag coefficients. The overall accordance of the drag is surprisingly good. The simulated drag numbers of the AoA setups of 8, 9, 10.5, 12deg deviate by 4% from the coast-down results. The low drag setup (up to 19%), however, shows a much higher deviation. Due to the presented 2nd order method of drag calculation, only a constant drag value per setup is extracted from the data. The measured drag is higher than the simulated one in some cases (12deg, low-drag). For comparability, the deviation is always calculated with respect to the higher value. There is no clear trend of data deviation apparent (for instance less deviation towards higher speed, see downforce data).

In general, the downforce deviates much more than the drag. Throughout all setups (except low-drag), there is a high deviation in low-speed of up to 19%. In high speed, data only deviates up to 5%. Over the speed range, there is a reduction of test track downforce and an increase of CFD downforce respectively. Contrarily, the data at low-drag setup matches better in low-speed and deviates more in high-speed.

Table 9: Coast-down, comparison of coefficients

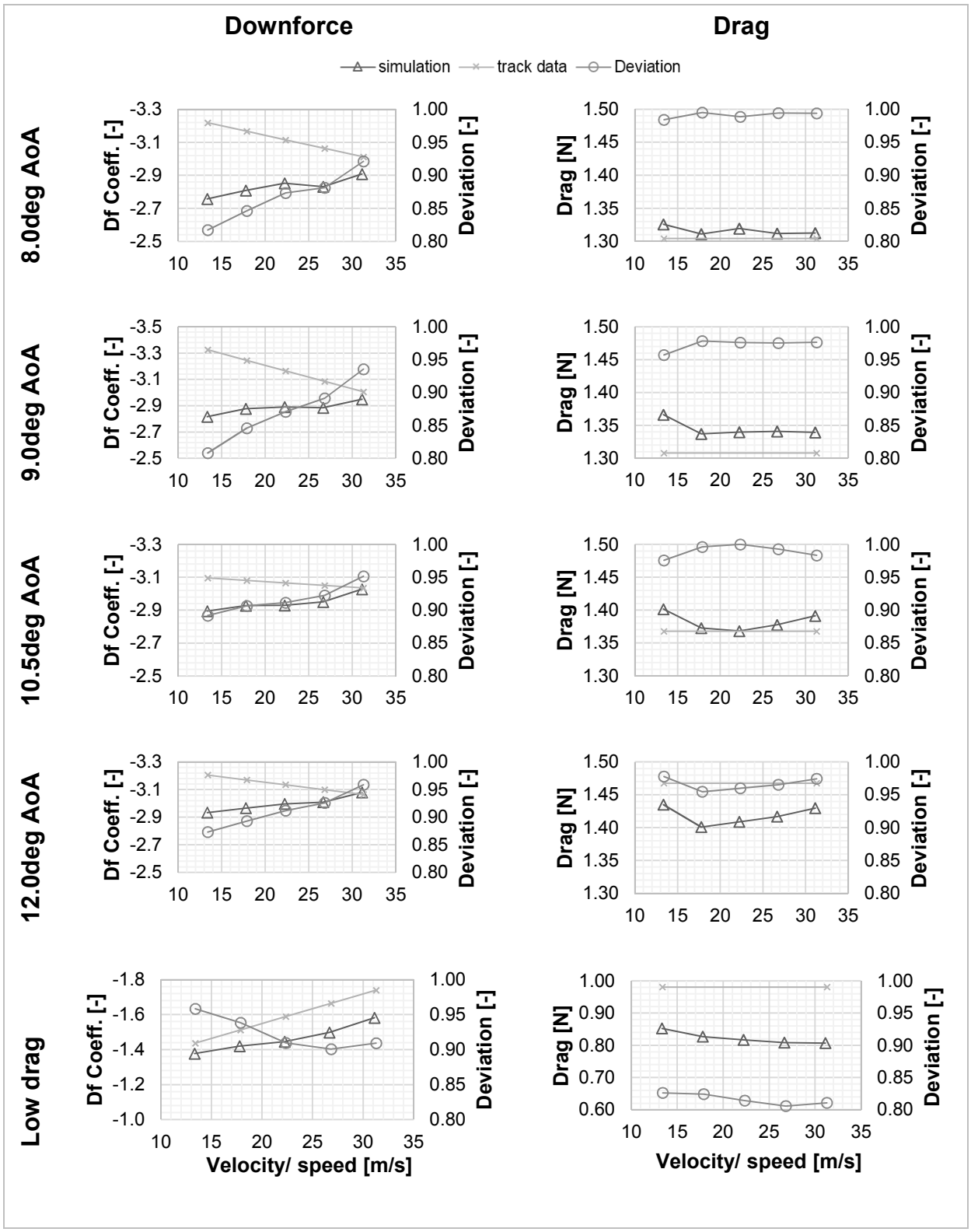

Regarding the aerodynamic balance, it can be concluded that the coast-down data show a much higher difference over the speed range (up to 10%) than the CFD data (up to 3%). Moreover, Figure 51 indicates a high deviation of coast-down and CFD data. Both data sets are only close to each other at high-speed of 27m/s to 32m/s.

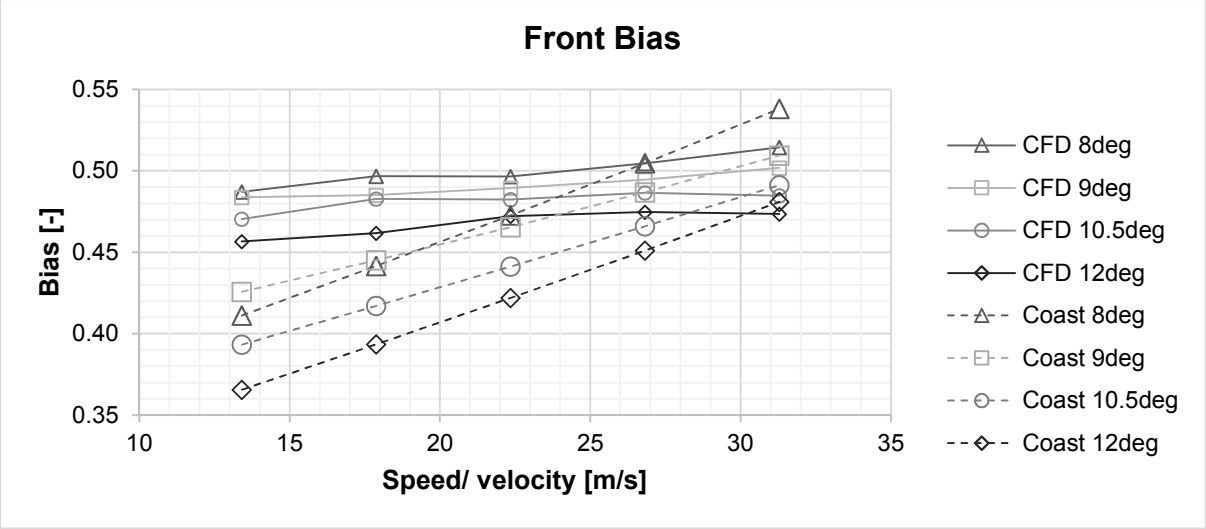

Figure 51: Comparison of the front bias of coast-down and test track data

4.5. Discussion

The presented data of on-track test and CFD simulation do not accurately match each other. The CFD simulation cannot be considered as being verified through the coast-down test. However, this result was expected because of varying testing conditions and inaccurate methods of wheel load measurement. Nevertheless, the presented comparison has proven that the coast-down test is a good tool for the evaluation and comparison of the on-track aerodynamic performance when there is no access to professional testing facilities such as wind tunnels. The comparison shows that the drag prediction is more accurate than the downforce respectively. Even small changes in the setup could be detected within the presented coast-down test and in other on-track tests (skid pad, FSAE-style test track) that the author performed throughout this thesis work [39, 40].

5. Conclusion

The study carried out in this thesis has shown that a coast-down test is a reasonable cost-effective tool for the evaluation of the aerodynamic performance.

Even small setup changes of 1deg overall angle of attack at the rear wing could be detected in the downforce and aerodynamic balance. Due to the calculation method of the drag coefficient which only relies on a velocity and time data input, it is expected that these results are much more accurate than the downforce data obtained by the shock potentiometers. The deviations of the compared coast-down simulation and test run verify that assumption. Results of the performed CFD simulations of high-downforce setups (8.0, 9.0, 10.5, and 12.0deg angle of attack) show averaged differences (over all setups) in downforce and drag according to the chosen speed ranges of:

- Drag: 4% (low-speed), 3% (mid-speed), 2% (high-speed)
- Downforce: 14% (low-speed), 11% (mid-speed), 7% (high-speed)
- Bias: 16% (low-speed), 8% (mid-speed), 3% (high-speed)

The developed CFD model is a good basis to start further developments of aerodynamic devices for future FSAE cars. It is adapted to the team's available computational power and can be used for comparisons of different setup and design iterations. Moreover, a comprehensive database of the JMS14c and its sensitivities has been created. From the CFD sensitivity studies it can be concluded that there are only small changes in coefficients across the motion and speed range of the vehicle. The overall car coefficients vary just slightly.

REFERENCES

[1] J. Katz, Race car aerodynamics: designing for speed: Robert Bentley, 1995.

[2] Society of Automotive Engineers SAE, "Rules Formula SAE 2014," 2014.

[3] L. Eckstein, Längsdynamik von Kraftfahrzeugen: Verkehrssystem Kraftfahrzeug, Kräfte am Fahrzeug, Antriebstrang, Bremsen, Fahrleistungen und Verbrauch; Vorlesungsumdruck Fahrzeugtechnik I: Forschungsges. Kraftfahrwesen, 2014.

[4] W. F. Milliken and D. L. Milliken, Race car vehicle dynamics vol. 400: Society of Automotive Engineers Warrendale, 1995.

[5] M. Mitschke, "Dynamik der Kraftfahrzeuge - Band A: Antrieb und Bremsung," 1995.

[6] M. Mitschke, "Dynamik der Kraftfahrzeuge - Band C: Fahrverhalten," 1990.

[7] W.-H. Hucho, Aerodynamik der stumpfen Körper: Vieweg Braunschweig,, Germany, 2002.

[8] P. K. Kundu and I. M. Cohen, Fluid Mechanics: Elsevier Science, 2010.

[9] S. McBeath, Competition car aerodynamics: Haynes North America Incorporated, 2006.

[10] Y. Cengel and J. Cimbala, Fluid Mechanics Fundamentals and Applications: Third Edition: McGraw-Hill Higher Education, 2013.

[11] SAE, "SAE Vehicle Fixed Coordinate System."

[12] I. Preda, D. Covaciu, and G. Ciolan, "Coast Down Test–Theoretical And Experimental Approach," 2010.

[13] M. Trzesniowski, Rennwagentechnik: Grundlagen, Konstruktion, Komponenten, Systeme ; mit 106 Tabellen: Vieweg Verlag, Friedr, & Sohn Verlagsgesellschaft mbH, 2010.

[14] E. M. Kasprzak and D. Gentz, "The Formula SAE Tire Test Consortium-Tire Testing and Data Handling," 2006.

[15] C. Smith, Tune to Win: The art and science of race car development and tuning: Aero Publishers, Incorporated, 1978.

[16] A. R. Hammond and R. G. Flay, "Aerodynamic Design of a Formula SAE Race Car," BBAA VI International Colloquiun on: Bluff Bodies Aerodynamics & Applications, Milano, Italy, 2008.

[17] R. Weingart, "Antriebsauslegung eines Formula Student Electric Fahrzeuges," Study Research Project, Kraftfahrzeugtechnik, Westsächsische Hochschule Zwickau, 2012.

[18] S. S. Pakkam, High Downforce Aerodynamics for Motorsports: North Carolina State University, 2011.

[19] OptimumG, "Vehicle Dynamics Seminar," ed, 2012.

[20] I. American Honda Motor Co., "Honda Vehicle Stability Assist," ed: American Honda Motor Co., Inc., 2008.

[21] M. Krumm and P. De La Rosa, Driving on the Edge: The Art and Science of Race Driving: Icon Publishing Limited, 2011.

[22] A. Gnech, "Development of a Robust Workflow for a CFD Analysis of External Aerodynamics in a Virtual Wind Tunnel," Mechanical Engineering, RTWH Aachen, Altair Engineering Inc. Commercial Software Devision, 2012.

[23] O. Cleynen, "Wing profile nomenclature," in http://en.wikipedia.org/wiki/File:Wing_profile_nomenclature.svg, W. p. nomenclature, Ed., ed: Wikimedia Foundation Inc.,, 2011.

[24] P. K. Yeung, "Lift-induced drag and aspect ratio," in http://soliton.ae.gatech.edu/labs/windtunl/classes/dci/intro/aerodesn/dci03b.html, vortsys, Ed., ed: Georgia Tech Institute, N/A.

[25] P. Haney, "Airfoil in ground effect," ed.

[26] J. Segers, Analysis techniques for racecar data acquisition vol. 367: SAE International Warrendale, PA, 2008.

[27] R. Weingart, "Evaluation of the Pitch Center Location Through Ride Height Data For Further Use in CFD Simulations (unpublished)," 2015.

[28] T. D. Gillespie, Fundamentals of vehicle dynamics vol. 400: Society of Automotive Engineers Warrendale, PA, 1992.

[29] H. K. Versteeg and W. Malalasekera, An introduction to computational fluid dynamics: the finite volume method: Pearson Education, 2007.

[30] S. Corrsin, "Turbulent flow," American Scientist, pp. 300-325, 1961.

[31] A. Bakker. (2012, 1/15/15). Applied Computational Fluid Dynamics. Available: http://www.bakker.org

[32] L. a. C. Team, "Wall functions," ed, 2012.

[33] cd-Adapco. (2013, Workshop: External Aerodynamics of Race Car.

[34] S. Wordley and J. Saunders, "Aerodynamics for Formula SAE: A Numerical, Wind Tunnel and On-Track Study," 2006.

[35] Tutorhelpdesk, "Boundary layer flow," Laminar%20boundary%20layer.jpg, Ed., ed, 2008.

[36] T. J. Craft, "Wall Functions," A. a. C. E. The University of Manchester - School of Mechanical, Ed., ed: The University of Manchester, 2011.

[37] D. Anderson John, "Fundamentals of aerodynamics," ed: McGraw Hill International.[35] Study course in three dimensional turbomachinery flows and transonic flows in turbomachinery, Ecole Centrale de Lyon, 2005.

[38] cd-Adapco, "Star-CCM+ User Guide," ed, 2014.

[39] R. Weingart, "Evaluating FSAE Aerodynamic Performance Through Skid Pad Testing (unpublished)," 2015.

[40] R. Weingart, "Evaluating FSAE Aerodynamic Performance Through Real Track Testing (unpublished)," 2015.

APPENDIX

(This page is left intentionally blank)

Appendix A: Center of Gravity Measurement

Table 10: CoG measurement, JMS14c with driver [27]

Leveled - JMS14c with driver					
corner	[lbs]	[kg]	corner	[lbs]	[kg]
FL	147.8	67.04	FR	151.3	68.62
RL	179.6	81.46	RR	167.1	75.79
total	645.8	292.93			
comment	adjusted tire pressure to 10psi, not fueled up, with coolant				
l_rear	30.10	["]	764.65	[mm]	**46.3%**
l_front	34.85	["]	886.34	[mm]	**53.7%**

Tilted - JMS14c with driver					
H_FA	29.61	["]	752.10	[mm]	
α	27.1	[°]	0.474	[rad]	
corner	[lbs]	[kg]	corner	[lbs]	[kg]
FL'	146.6	66.49	FR'	137.9	62.55
RL'	184.7	83.77	RR'	175.0	79.37
total	644.2	292.20	**OK**		
H_COG_1	12.97	["]	329.63	[mm]	
H_COG_2	12.81	["]	325.50	[mm]	

Appendix B: Pitch Center Location

Calculation of pitch angle:

[27]
$$\gamma_{pitch} = atan\left(\frac{RH_{RA,dyn} - RH_{FA,dyn}}{WB}\right) \tag{63}$$

γ_{Pitch} – pitch angle
$RH_{RA,dyn}$ – dynamic rear ride height
$RH_{FA,dyn}$ – dynamic front ride height
WB – wheelbase

Calculation of gap size between front wing and ground:

[27]
$$H_{FW,gap} = H_{FW,static} + \left\{ sin\left(atan\left(\frac{RH_{FA,dyn} - RH_{RA,dyn}}{WB}\right)\right) \cdot \left(WB + \frac{RH_{RA,dyn} - RH_{Static}}{\frac{\left(RH_{FA,dyn} - RH_{RA,dyn}\right)}{WB}} + \left|L_{FW,x-pos}\right| \right) \right\} \tag{64}$$

RH_{Static} – static ride height
$H_{FW,gap}$ – gap size between front wing and ground
$H_{FW,static}$ – static height of front wing with respect to the ground
$L_{FW,x-pos}$ – distance from front axle to lowest point of front wing

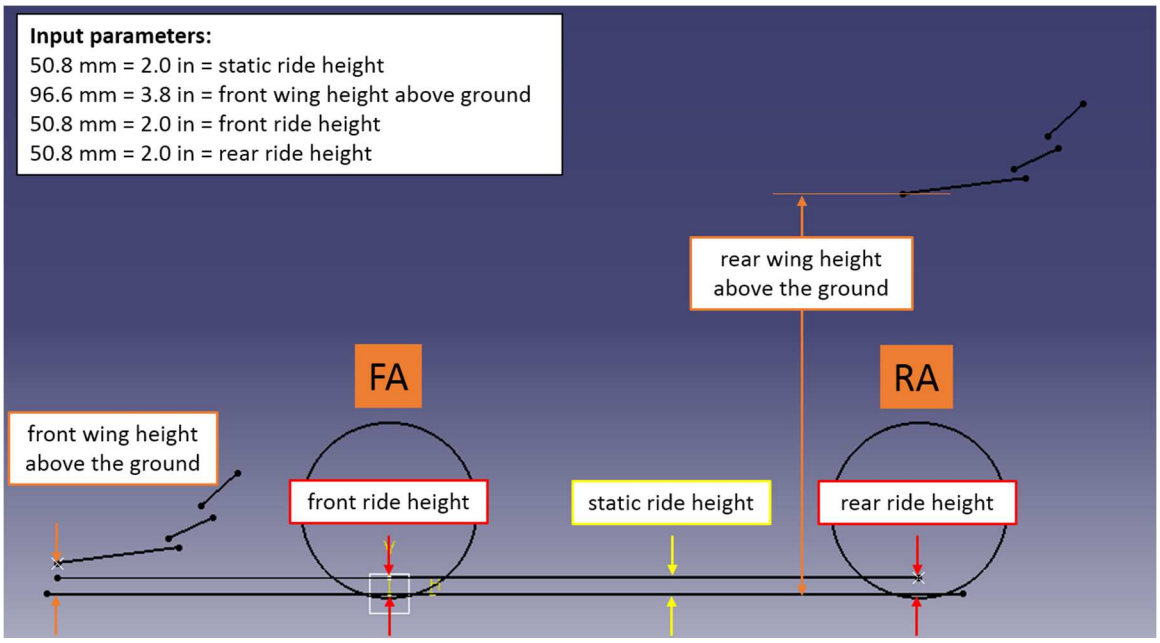

Figure 52: Pitch center location remodeled in CAD, static [27]

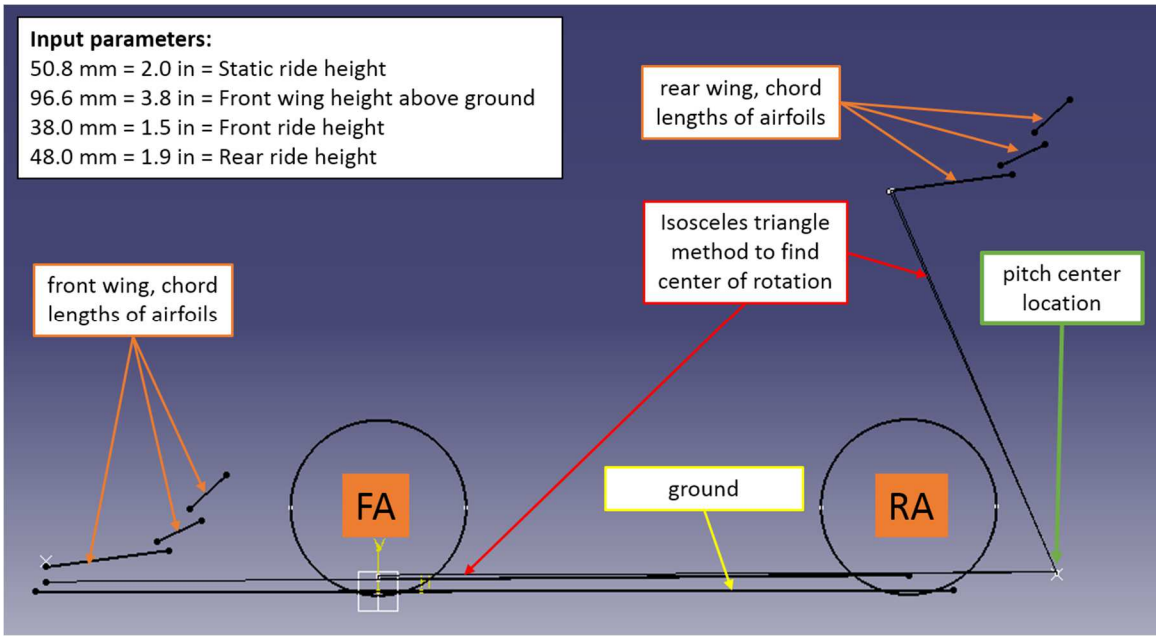

Figure 53: Pitch center location remodeled in CAD, dynamic [27]

Table 11: Change in Front wing height (left), change in pitch angle (right) [27]

FRONT [mm]	REAR ride height in [mm]																									
	15	17.5	20	22.5	25	27.5	30	32.5	35	37.5	40	42.5	45	47.5	50	52.5	55	57.5	60	62.5	65	67.5	70
15	#DIV/0!	59.29	57.73	56.16	54.59	53.02	51.46	49.89	48.32	46.76	45.19	43.63	42.06	40.49	38.93	37.36	35.80	34.24	32.67	31.11	29.54	27.98	26.42
17.5	64.93	#DIV/0!	61.79	60.23	58.66	57.09	55.52	53.96	52.39	50.82	49.26	47.69	46.13	44.56	42.99	41.43	39.86	38.30	36.73	35.17	33.61	32.04	30.48
20	68.99	67.43	#DIV/0!	64.29	62.73	61.16	59.59	58.02	56.46	54.89	53.32	51.76	50.19	48.63	47.06	45.49	43.93	42.36	40.80	39.23	37.67	36.10	34.54
22.5	73.06	71.49	69.93	#DIV/0!	66.79	65.23	63.66	62.09	60.52	58.96	57.39	55.82	54.26	52.69	51.13	49.56	47.99	46.43	44.86	43.30	41.73	40.17	38.60
25	77.13	75.56	73.99	72.43	#DIV/0!	69.29	67.73	66.16	64.59	63.02	61.46	59.89	58.32	56.76	55.19	53.62	52.06	50.49	48.93	47.36	45.80	44.23	42.67
27.5	81.20	79.63	78.06	76.49	74.93	#DIV/0!	71.79	70.23	68.66	67.09	65.52	63.96	62.39	60.82	59.26	57.69	56.12	54.56	52.99	51.43	49.86	48.30	46.73
30	85.26	83.70	82.13	80.56	78.99	77.43	#DIV/0!	74.29	72.73	71.16	69.59	68.02	66.46	64.89	63.32	61.76	60.19	58.62	57.06	55.49	53.93	52.36	50.80
32.5	89.33	87.76	86.20	84.63	83.06	81.49	79.93	#DIV/0!	76.79	75.23	73.66	72.09	70.52	68.96	67.39	65.82	64.26	62.69	61.12	59.56	57.99	56.43	54.86
35	93.40	91.83	90.26	88.70	87.13	85.56	83.99	82.43	#DIV/0!	79.29	77.73	76.16	74.59	73.02	71.46	69.89	68.32	66.76	65.19	63.62	62.06	60.49	58.93
37.5	97.47	95.90	94.33	92.76	91.20	89.63	88.06	86.49	84.93	#DIV/0!	81.79	80.23	78.66	77.09	75.52	73.96	72.39	70.82	69.26	67.69	66.12	64.56	62.99
40	101.53	99.97	98.40	96.83	95.26	93.70	92.13	90.56	88.99	87.43	#DIV/0!	84.29	82.73	81.16	79.59	78.02	76.46	74.89	73.32	71.76	70.19	68.62	67.06
42.5	105.60	104.03	102.47	100.90	99.33	97.76	96.20	94.63	93.06	91.49	89.93	#DIV/0!	86.79	85.23	83.66	82.09	80.52	78.96	77.39	75.82	74.26	72.69	71.12
45	109.67	108.10	106.53	104.97	103.40	101.83	100.26	98.70	97.13	95.56	93.99	92.43	#DIV/0!	89.29	87.73	86.16	84.59	83.02	81.46	79.89	78.32	76.76	75.19
47.5	113.73	112.17	110.60	109.03	107.47	105.90	104.33	102.76	101.20	99.63	98.06	96.49	94.93	#DIV/0!	91.79	90.23	88.66	87.09	85.52	83.96	82.39	80.82	79.26
50	117.80	116.23	114.67	113.10	111.53	109.97	108.40	106.83	105.26	103.70	102.13	100.56	98.99	97.43	#DIV/0!	94.29	92.73	91.16	89.59	88.02	86.46	84.89	83.32
52.5	121.86	120.30	118.73	117.17	115.60	114.03	112.46	110.90	109.33	107.76	106.20	104.63	103.06	101.49	99.93	#DIV/0!	96.79	95.23	93.66	92.09	90.52	88.96	87.39
55	125.93	124.36	122.80	121.23	119.66	118.10	116.53	114.96	113.40	111.83	110.26	108.70	107.13	105.56	103.99	102.43	#DIV/0!	99.29	97.73	96.16	94.59	93.02	91.46
57.5	129.99	128.43	126.86	125.30	123.73	122.16	120.60	119.03	117.46	115.90	114.33	112.76	111.20	109.63	108.06	106.49	104.93	#DIV/0!	101.79	100.23	98.66	97.09	95.52
60	134.06	132.49	130.93	129.36	127.80	126.23	124.66	123.10	121.53	119.96	118.40	116.83	115.26	113.70	112.13	110.56	108.99	107.43	#DIV/0!	104.29	102.73	101.16	99.59
62.5	138.12	136.56	134.99	133.43	131.86	130.30	128.73	127.16	125.60	124.03	122.46	120.90	119.33	117.76	116.20	114.63	113.06	111.49	109.93	#DIV/0!	106.79	105.23	103.66
65	142.19	140.62	139.06	137.49	135.93	134.36	132.80	131.23	129.66	128.10	126.53	124.96	123.40	121.83	120.26	118.70	117.13	115.56	113.99	112.43	#DIV/0!	109.29	107.73
67.5	146.25	144.69	143.12	141.56	139.99	138.43	136.86	135.29	133.73	132.16	130.60	129.03	127.46	125.90	124.33	122.76	121.20	119.63	118.06	116.49	114.93	#DIV/0!	111.79
70	150.31	148.75	147.18	145.62	144.06	142.49	140.93	139.36	137.79	136.23	134.66	133.10	131.53	129.96	128.40	126.83	125.26	123.70	122.13	120.56	118.99	117.43	#DIV/0!
72.5	154.37	152.81	151.25	149.68	148.12	146.55	144.99	143.42	141.86	140.29	138.73	137.16	135.60	134.03	132.46	130.90	129.33	127.76	126.20	124.63	123.06	121.49	119.93
75	158.44	156.87	155.31	153.75	152.18	150.62	149.05	147.49	145.92	144.36	142.79	141.23	139.66	138.10	136.53	134.96	133.40	131.83	130.26	128.70	127.13	125.56	123.99

FRONT [mm]	REAR ride height in [mm]																									
	15	17.5	20	22.5	25	27.5	30	32.5	35	37.5	40	42.5	45	47.5	50	52.5	55	57.5	60	62.5	65	67.5	70
15	0.00	-0.09	-0.17	-0.26	-0.35	-0.43	-0.52	-0.61	-0.69	-0.78	-0.87	-0.95	-1.04	-1.13	-1.21	-1.30	-1.39	-1.47	-1.56	-1.65	-1.73	-1.82	-1.91
17.5	0.09	0.00	-0.09	-0.17	-0.26	-0.35	-0.43	-0.52	-0.61	-0.69	-0.78	-0.87	-0.95	-1.04	-1.13	-1.21	-1.30	-1.39	-1.47	-1.56	-1.65	-1.73	-1.82
20	0.17	0.09	0.00	-0.09	-0.17	-0.26	-0.35	-0.43	-0.52	-0.61	-0.69	-0.78	-0.87	-0.95	-1.04	-1.13	-1.21	-1.30	-1.39	-1.47	-1.56	-1.65	-1.73
22.5	0.26	0.17	0.09	0.00	-0.09	-0.17	-0.26	-0.35	-0.43	-0.52	-0.61	-0.69	-0.78	-0.87	-0.95	-1.04	-1.13	-1.21	-1.30	-1.39	-1.47	-1.56	-1.65
25	0.35	0.26	0.17	0.09	0.00	-0.09	-0.17	-0.26	-0.35	-0.43	-0.52	-0.61	-0.69	-0.78	-0.87	-0.95	-1.04	-1.13	-1.21	-1.30	-1.39	-1.47	-1.56
27.5	0.43	0.35	0.26	0.17	0.09	0.00	-0.09	-0.17	-0.26	-0.35	-0.43	-0.52	-0.61	-0.69	-0.78	-0.87	-0.95	-1.04	-1.13	-1.21	-1.30	-1.39	-1.47
30	0.52	0.43	0.35	0.26	0.17	0.09	0.00	-0.09	-0.17	-0.26	-0.35	-0.43	-0.52	-0.61	-0.69	-0.78	-0.87	-0.95	-1.04	-1.13	-1.21	-1.30	-1.39
32.5	0.61	0.52	0.43	0.35	0.26	0.17	0.09	0.00	-0.09	-0.17	-0.26	-0.35	-0.43	-0.52	-0.61	-0.69	-0.78	-0.87	-0.95	-1.04	-1.13	-1.21	-1.30
35	0.69	0.61	0.52	0.43	0.35	0.26	0.17	0.09	0.00	-0.09	-0.17	-0.26	-0.35	-0.43	-0.52	-0.61	-0.69	-0.78	-0.87	-0.95	-1.04	-1.13	-1.21
37.5	0.78	0.69	0.61	0.52	0.43	0.35	0.26	0.17	0.09	0.00	-0.09	-0.17	-0.26	-0.35	-0.43	-0.52	-0.61	-0.69	-0.78	-0.87	-0.95	-1.04	-1.13
40	0.87	0.78	0.69	0.61	0.52	0.43	0.35	0.26	0.17	0.09	0.00	-0.09	-0.17	-0.26	-0.35	-0.43	-0.52	-0.61	-0.69	-0.78	-0.87	-0.95	-1.04
42.5	0.95	0.87	0.78	0.69	0.61	0.52	0.43	0.35	0.26	0.17	0.09	0.00	-0.09	-0.17	-0.26	-0.35	-0.43	-0.52	-0.61	-0.69	-0.78	-0.87	-0.95
45	1.04	0.95	0.87	0.78	0.69	0.61	0.52	0.43	0.35	0.26	0.17	0.09	0.00	-0.09	-0.17	-0.26	-0.35	-0.43	-0.52	-0.61	-0.69	-0.78	-0.87
47.5	1.13	1.04	0.95	0.87	0.78	0.69	0.61	0.52	0.43	0.35	0.26	0.17	0.09	0.00	-0.09	-0.17	-0.26	-0.35	-0.43	-0.52	-0.61	-0.69	-0.78
50	1.21	1.13	1.04	0.95	0.87	0.78	0.69	0.61	0.52	0.43	0.35	0.26	0.17	0.09	0.00	-0.09	-0.17	-0.26	-0.35	-0.43	-0.52	-0.61	-0.69
52.5	1.30	1.21	1.13	1.04	0.95	0.87	0.78	0.69	0.61	0.52	0.43	0.35	0.26	0.17	0.09	0.00	-0.09	-0.17	-0.26	-0.35	-0.43	-0.52	-0.61
55	1.39	1.30	1.21	1.13	1.04	0.95	0.87	0.78	0.69	0.61	0.52	0.43	0.35	0.26	0.17	0.09	0.00	-0.09	-0.17	-0.26	-0.35	-0.43	-0.52
57.5	1.47	1.39	1.30	1.21	1.13	1.04	0.95	0.87	0.78	0.69	0.61	0.52	0.43	0.35	0.26	0.17	0.09	0.00	-0.09	-0.17	-0.26	-0.35	-0.43
60	1.56	1.47	1.39	1.30	1.21	1.13	1.04	0.95	0.87	0.78	0.69	0.61	0.52	0.43	0.35	0.26	0.17	0.09	0.00	-0.09	-0.17	-0.26	-0.35
62.5	1.65	1.56	1.47	1.39	1.30	1.21	1.13	1.04	0.95	0.87	0.78	0.69	0.61	0.52	0.43	0.35	0.26	0.17	0.09	0.00	-0.09	-0.17	-0.26
65	1.73	1.65	1.56	1.47	1.39	1.30	1.21	1.13	1.04	0.95	0.87	0.78	0.69	0.61	0.52	0.43	0.35	0.26	0.17	0.09	0.00	-0.09	-0.17
67.5	1.82	1.73	1.65	1.56	1.47	1.39	1.30	1.21	1.13	1.04	0.95	0.87	0.78	0.69	0.61	0.52	0.43	0.35	0.26	0.17	0.09	0.00	-0.09
70	1.91	1.82	1.73	1.65	1.56	1.47	1.39	1.30	1.21	1.13	1.04	0.95	0.87	0.78	0.69	0.61	0.52	0.43	0.35	0.26	0.17	0.09	0.00
72.5	1.99	1.91	1.82	1.73	1.65	1.56	1.47	1.39	1.30	1.21	1.13	1.04	0.95	0.87	0.78	0.69	0.61	0.52	0.43	0.35	0.26	0.17	0.09
75	2.08	1.99	1.91	1.82	1.73	1.65	1.56	1.47	1.39	1.30	1.21	1.13	1.04	0.95	0.87	0.78	0.69	0.61	0.52	0.43	0.35	0.26	0.17

Appendix C: CFD Model Refinements

Table 12: Volume mesh refinements

#	name	type	custom size [m]		number of prism layers	prism layer thickness [m]	prism layer stretching	wake refine
			min.	target				
1	AIR (sub domain)	Surface	1	1	default			no
2	aero_endplates	Surface	0.01	0.002	10	0.002	default	no
3	aero_flaps	Surface	0.005	0.001	15	0.005	default	yes
4	aero_mps	Surface	0.02	0.001	15	0.005	default	yes
5	car_aarms _uprights	Surface	0.01	0.004	9	0.002	default	no
6	car_driver	Surface	0.02	0.01	9	0.002	default	yes
7	car_engine	Surface	0.02	0.01	8	0.002	default	no
8	car_mainhoop	Surface	0.01	0.04	8	0.001	default	no
9	car_ monocoque	Surface	0.02	0.005	8	0.002	default	no
10	car_nosecone	Surface	0.02	0.005	9	0.002	default	no
11	car_radiator _inlet_outlet	Surface	0.01	0.002	disabled			no
12	car_radiator _wall	Surface	0.01	0.002	9	0.002	default	no
13	car	Volumetric	0.2		default			-
14	car_fine	Volumetric	0.1		default			-
15	car_sidepod _skidplate	Surface	0.02	0.002	10	0.002	default	no
16	car_tires	Surface	0.02	0.002	12	0.004	default	yes

#	name	type	custom size [m]		number of prism layers	prism layer thickness [m]	prism layer stretching	wake refine
			min.	target				
17	driver_neck	volumetric	0.005		default			-
18	ground	Surface	default	default	disabled			no
19	driver_helmet	Volumetric	0.005		default			-
20	outer refinement	Volumetric	1		default			-
21	radiator	Volumetric	0.005		default			-
22	refinement _LE_TE	Volumetric	0.005		default			-
23	refinement _nosecone _helmet	Volumetric	0.005		default			-
24	tire_contact _patch	Volumetric	0.002		default			-
25	tires	Volumetric	0.01		default			-
26	undertray	Volumetric	0.02		default			-
27	undertray_fine	Volumetric	0.01		default			-
28	wake_1	Volumetric	0.04		default			-
29	wake_2	Volumetric	0.1		default			-
30	wake_3	Volumetric	0.2		default			-
31	wake_4	volumetric	0.5		default			-
32	wings_sidepod _skidplate	Curve	0.005	0.002	-	-	-	-

Appendix D: Half Car Model Analysis

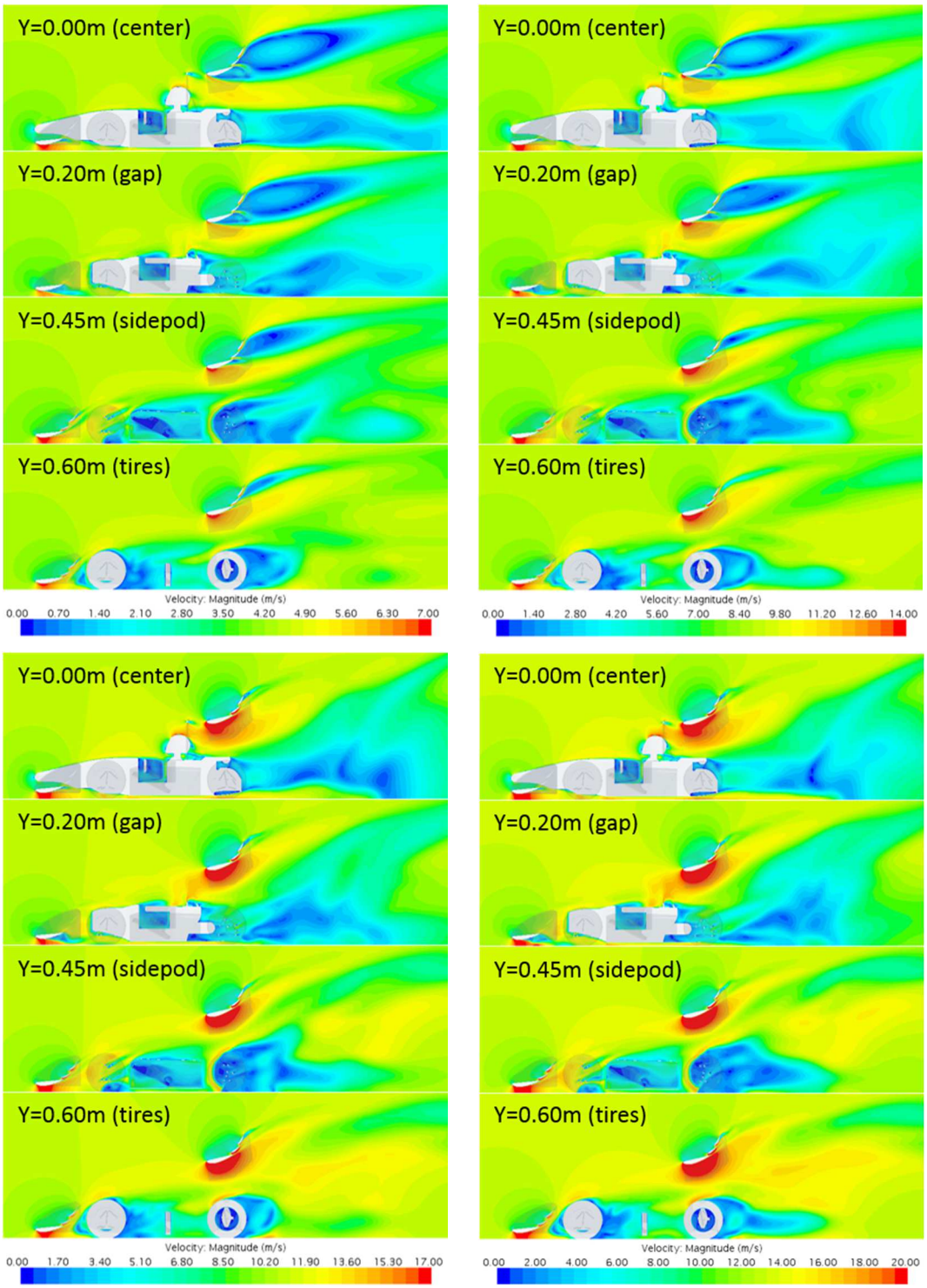

Figure 54: Baseline model at various vehicle velocities – velocity distribution plots (top left – 10mph, top right – 20mph, bottom left – 25mph, bottom right – 30mph)

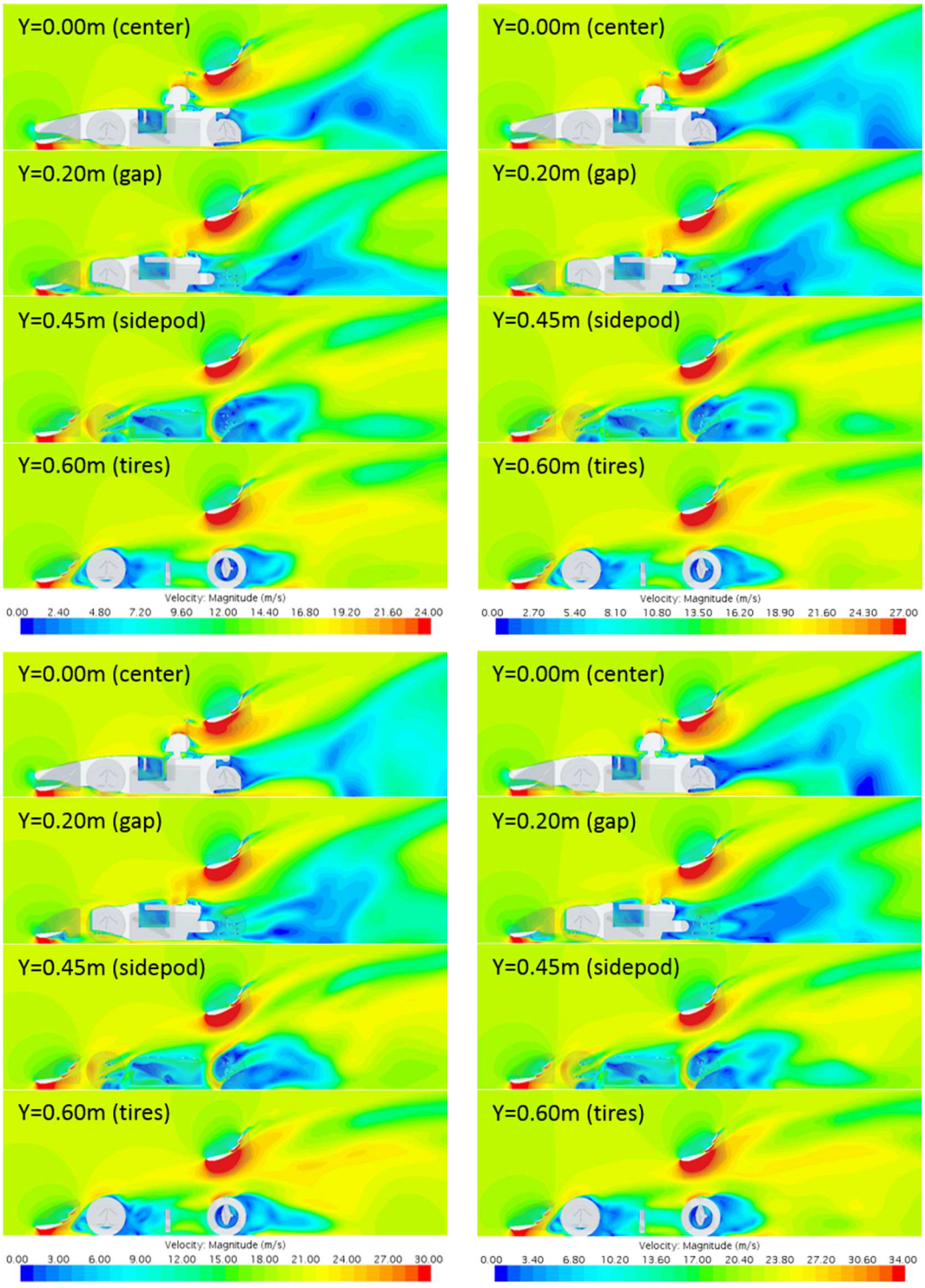

Figure 55: Baseline model at various vehicle velocities – velocity distribution plots (top left –35mph, top right – 40mph, bottom left – 45mph, bottom right – 50mph)

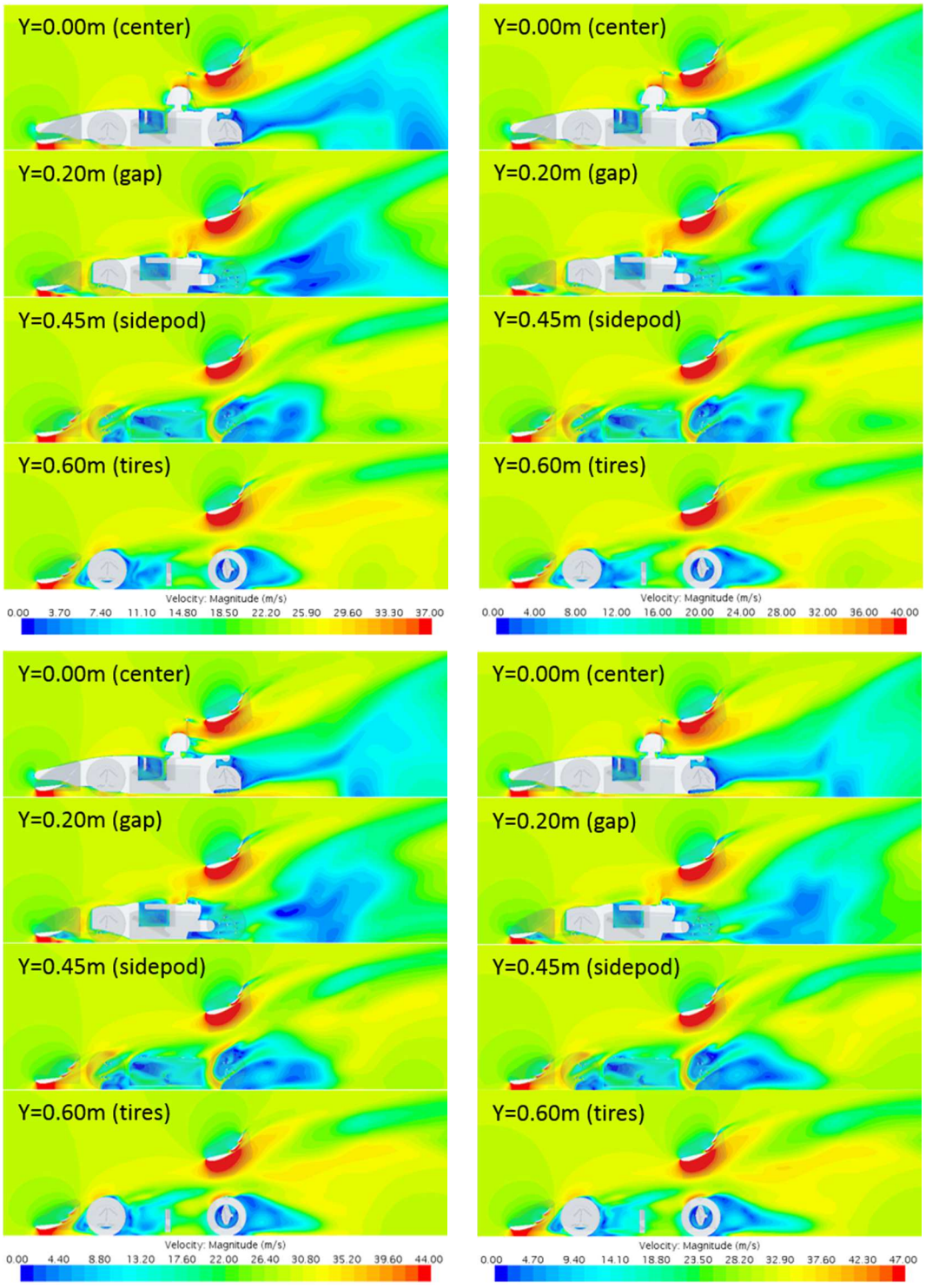

Figure 56: Baseline model at various vehicle velocities – velocity distribution plots (top left –55mph, top right – 60mph, bottom left – 65mph, bottom right – 70mph)